OBSERVATIONS OF MICROSCALE GRAVITY WAVES IN THE

NOCTURNAL BOUNDARY LAYER ABOVE AN ORCHARD

CANOPY BY A HORIZONTALLY SCANNING LIDAR

―――――――――

A Thesis

Presented

to the Faculty of

California State University, Chico

―――――――――

In Partial Fulfillment

of the Requirements for the Degree

Master of Science

in

Environmental Science

―――――――――

by

© Tyson Randall 2015

Spring 2015

OBSERVATIONS OF MICROSCALE GRAVITY WAVES IN THE

NOCTURNAL BOUNDARY LAYER ABOVE AN ORCHARD

CANOPY BY A HORIZONTALLY SCANNING LIDAR

A Thesis

by

Tyson Randall

Spring 2015

APPROVED BY THE DEAN OF GRADUATE STUDIES
AND VICE PROVOST FOR RESEARCH:

_____

Eun K. Park, Ph.D.

APPROVED BY THE GRADUATE ADVISORY COMMITTEE:

_____

Shane D. Mayor, Ph.D., Chair

_____

Chris Gaffney, Ph.D.

_____

Masaki Hamada, M.S.

PUBLICATION RIGHTS

No portion of this thesis may be reprinted or reproduced in any manner unacceptable to the usual copyright restrictions without the written permission of the author.

ACKNOWLEDGMENTS

TABLE OF CONTENTS

LIST OF FIGURES

ABSTRACT

OBSERVATIONS OF MICROSCALE GRAVITY WAVES

IN THE NOCTURNAL BOUNDARY LAYER ABOVE

AN ORCHARD CANOPY BY A HORIZONTALLY

SCANNING LIDAR

by

© Tyson Randall 2015

Master of Science in Environmental Science

California State University, Chico

Spring 2015

Fifty-two episodes of microscale gravity waves were analyzed. The waves were discovered in a data set resulting from the continuous operation of a ground-based scanning aerosol lidar over a 3-month period. The lidar operated in concert with a set of meteorological in-situ sensors on a 30-m-tall tower located within the lidar's field of view and within a large walnut orchard. The waves are also present in meteorological variables measured by the in-situ sensors such as wind and temperature. All of the episodes occurred at night when strong temperature inversions existed. The wavelengths ranged from 40 to 110 m. The waves propagated in the direction of and at speeds less than the mean wind at altitudes just above the canopy. The waves decrease in amplitude with height and with no phase shift suggesting that they are evanescent rather than vertically propagating. The observations support the hypothesis that the waves are generated

by inflection point instabilities caused by the drag that the canopy imparts on the mean flow and that they do not transport energy or momentum vertically.

CHAPTER I

INTRODUCTION

Waves

Waves are a universal construct in science and mathematics. The study
of waves spans many scientific disciplines such as physics, meteorology, geology, and
chemistry. In nature, a wave is an oscillation that transfers energy. Some examples
of natural waves include sound waves, tsunamis, seismic waves, and electromagnetic
waves. All of these except electromagnetic waves require a medium in which to
propagate and are referred to as mechanical waves. Frequently, the medium is a
fluid which may be a gas or a liquid.

Mathematical Treatment

Waves are described by their wavelength, frequency, and amplitude. A
one-dimensional wave in some quantity, ψ, traveling in the positive x-direction can
be described by the equation

$$\psi(x,t) = A\cos(2\pi(\frac{x}{\lambda} - ft)) \tag{1}$$

or more generally

$$\psi(x,t) = Ae^{i(2\pi(\frac{x}{\lambda} - ft))} \tag{2}$$

where λ is the wavelength, f is the frequency, and A is the amplitude. The
wavelength is the distance between peaks, the frequency is the number of cycles per
unit time, and the amplitude is the difference between the maximum and zero. It is

sometimes more convenient to use more mathematically natural quantities such as wavenumber, k, and angular frequency, ω. They can be found from the relations

$$k = \frac{2\pi}{\lambda} \tag{3}$$

and

$$\omega = 2\pi f. \tag{4}$$

This simplifies Equations 1 and 2 to

$$\psi(x,t) = A\cos(kx - \omega t) \tag{5}$$

and

$$\psi(x,t) = Ae^{i(kx - \omega t)}. \tag{6}$$

The wave crests propagate at the phase speed, v_p, which is found by the relation

$$v_p = \lambda f \tag{7}$$

or

$$v_p = \frac{\omega}{k}. \tag{8}$$

This treatment is for linear, monochromatic (single wavelength), monotonic (single frequency) waves in one spatial dimension. However, waves can exist in two or three spatial dimensions. In these cases, a wave can be described as

$$\boldsymbol{\psi}(\mathbf{x},t) = \mathbf{A}e^{i(\mathbf{k}\cdot\mathbf{x} - \omega t)} \tag{9}$$

where $\mathbf{k}$ is the wavevector such that

$$||\mathbf{k}||^2 = k_x^2 + k_y^2 + k_z^2. \tag{10}$$

The right side of Equation 10 shows the x-, y-, and z-components of the wavenumber. The wavenumber is the magnitude of the wave vector. Equation 9 is a solution to the second-order, linear, partial-differential equation

$$\frac{\partial^2 \boldsymbol{\psi}}{\partial t^2} = v_p^2 \, \nabla^2 \, \boldsymbol{\psi} \tag{11}$$

known as the wave equation (*Durran*, 1999). Solutions to this equation are waves. Since it is a linear equation, the solutions obey superposition meaning that a linear combination of solutions is a solution itself. Superpositions of multiple frequencies can give more complex wave patterns (Figure 1). The sum of wave solutions can form wave envelopes or packets whose shape depends on the constituent frequencies. In these cases the wave packet moves at a speed

$$v_g = \frac{\partial \omega}{\partial k} \tag{12}$$

called the group velocity. For some waves, including gravity waves, the phase speed depends on frequency. In these waves, called dispersive waves, the group velocity is different than the phase speed. The group velocity is the rate at which the energy contained in the wave signal moves through space, not at the phase speed. Dispersive waves do not satisfy Equation 11, because the relation implies a constant phase speed for all frequencies.

Depending on whether the vertical component of the wave vector is real or imaginary, waves may be said to be vertically-propagating or evanescent (Figure
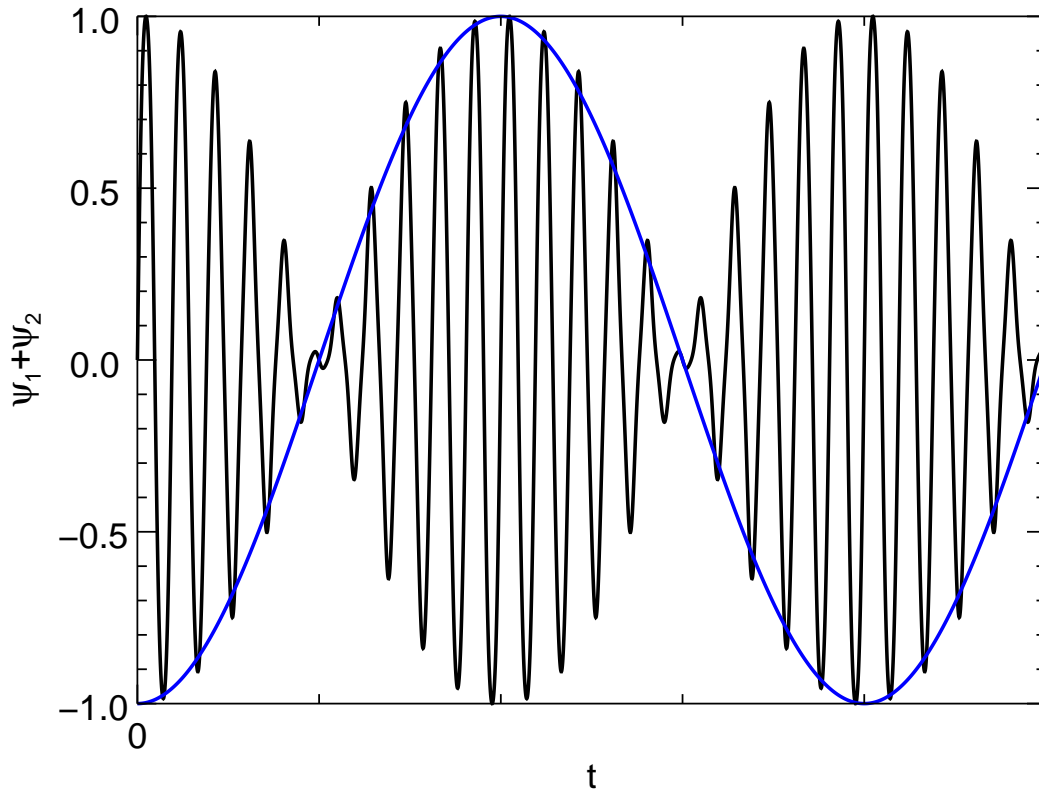
Figure 1. (Color required.) The superposition of two sine waves with frequencies differing by about 10% are shown by the black line, and propagate at the phase speed, v_p. The blue line indicates the wave packet that propagates at the group velocity, v_g.

2). Vertically-propagating waves have a real vertical component, k_z. A wave propagating in the xz-plane can be expressed as

$$\psi(\mathbf{x}, t) = A e^{i(\mathbf{k} \cdot x - \omega t)} \tag{13}$$

$$= A e^{(k_x x + k_z z - \omega t)}. \tag{14}$$

If the vertical wavenumber is real,

$$\boldsymbol{\psi} = A e^{i(k_x x - \omega t + \phi(z))} \tag{15}$$

where

$$\phi(z) = k_z z \tag{16}$$

showing a phase shift of the horizontal wave as a linear function of height.

Evanescent waves are waves that do not propagate in the vertical. The vertical component of the wave vector is purely imaginary,

$$k_z = i||k_z||. \tag{17}$$

An evanescent wave propagating in the x-direction, can be found from the equation

$$\boldsymbol{\psi}(\mathbf{x}, t) = A e^{i(\mathbf{k} \cdot \mathbf{x} - \omega t)} \tag{18}$$

$$= A e^{i(k_x x + i||k_z||z - \omega t)} \tag{19}$$

$$= A e^{i(k_x x - \omega t)} e^{-||k_z||z} \tag{20}$$

$$= \psi_x(x, t) e^{-||k_z||z}. \tag{21}$$

Therefore, their amplitude decays exponentially with height. From this equation, it is also evident that the phase is constant in altitude since there is no z-dependence left in the oscillatory factor.

Many phenomena in fluids can be described by the famous Navier–Stokes equation. It is a second-order partial-differential equation that
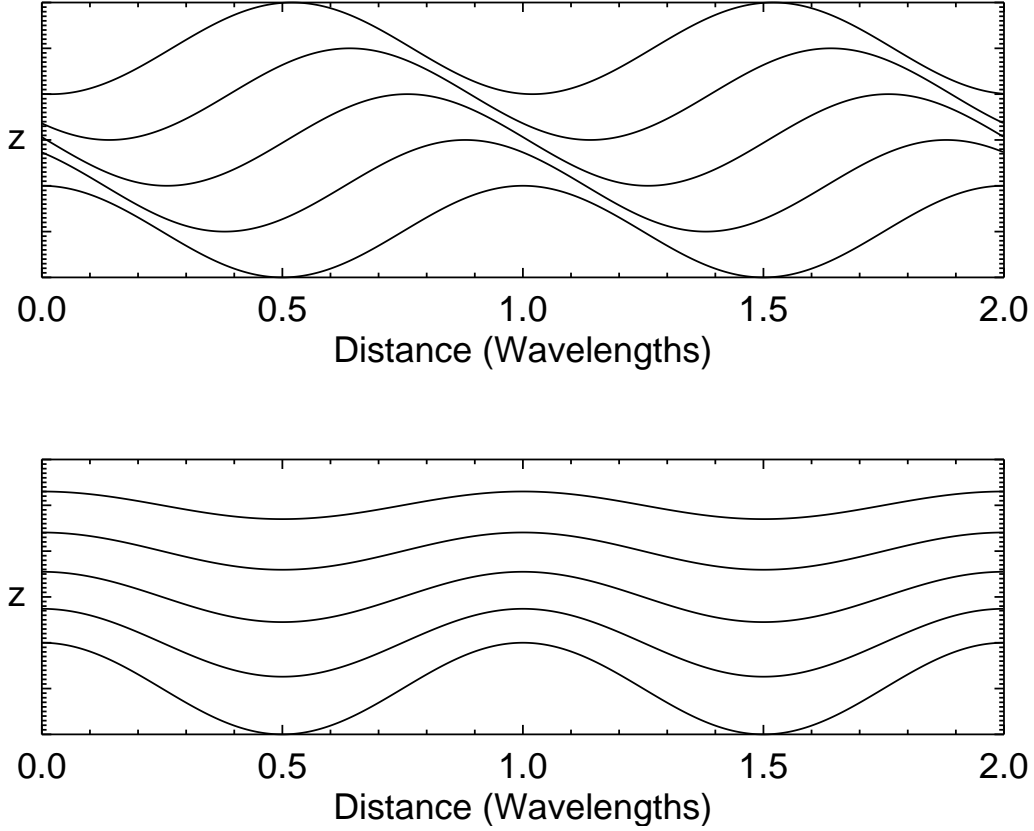
Figure 2. Top panel: Waves in a quantity, ψ, propagating in the positive x- and z-directions (k_z is real). Bottom panel: Evanescent waves, ψ, propagating in the x-direction (k_z is imaginary).

describes Newtonian fluids. One form of the Navier–Stokes equation is

$$\rho \frac{D\mathbf{u}}{Dt} = -\nabla P + \mu \nabla^2 \mathbf{u} + \frac{1}{3}\mu \nabla(\nabla \cdot \mathbf{u}) + \rho \mathbf{g} + \mathbf{B} \tag{22}$$

where $\mathbf{u}$ is the velocity of a fluid parcel, P is the pressure, μ is the dynamic viscosity, ρ is the density, $\mathbf{g}$ is the acceleration due to gravity and has a magnitude of 9.81 m s^{-2}, and $\mathbf{B}$ is other body forces per unit volume on the parcel. Where

$$\frac{D\boldsymbol{\xi}}{Dt} = \frac{\partial \boldsymbol{\xi}}{\partial t} + \mathbf{u} \cdot \nabla \boldsymbol{\xi} \tag{23}$$

for some vector field, $\boldsymbol{\xi}$. This is known as the material derivative. It describes the motion of the field from a Lagrangian framework. In a Lagrangian frame, the motion is from the perspective of a parcel that is moving with the flow. In contrast, an Eulerian framework is one from a stationary perspective and is described by the first term in the material derivative, $\partial \boldsymbol{\xi}/\partial t$, known as the local derivative. The remaining terms are known as the advective terms (*Kundu et al.*, 2011). There is no known general solution to this Equation 22, but when certain approximations are made, it is possible to eliminate terms and find solutions. The solutions describe important physical relations such as hydrostatic equilibrium or geostrophic balance. Other equations, such as continuity, ideal gas law, or conservation of energy, may be used in conjunction with Equation 22 to find other relationships such as the barometric law or the speed of sound.

Atmospheric Waves

Fluids give rise to various types of waves that occur at many scales. Sound waves, gravity waves, and inertial waves are all waves that can occur in fluids that can have wavelengths on orders ranging from centimeters to planetary scales (*Holton*, 2004). Waves result from perturbations of parcels in stable equilibria. For instance, a sound wave is the result of a parcel out of pressure equilibrium (*Hooke*, 1986). Compression or rarefraction leads to a greater or lower pressure in some volume of air with respect to the surrounding air. The air with higher pressure will exert a force on the air with lower pressure. The pressure gradient force will be directed toward lower pressure. Therefore, the low pressure region is compressed toward the equilibrium pressure and beyond, creating a region of high pressure. This process continues in three dimensions resulting in an acoustic wave. However, areas of high and low pressure do not always result in sound waves. Pressure gradients exist in the atmosphere when they are in

equilibrium or near equilibrium with other forces. For example, the pressure at the bottom of the atmosphere is greater than that of the air above it because gravity is constantly pulling the air down. Sound waves are a solution to Equation 22 when all of the forces are neglected except the pressure gradient.

Gravity provides a stable equilibrium in which the density of the fluid decreases with height. In this environment, the fluid is said to be stably stratified. Gravity waves, also known as buoyancy waves, occur due to a perturbation in this stable density profile which leads to unbalanced buoyant and gravitational forces. Under stable conditions, if a parcel is displaced downward adiabatically, it will be less dense than its environment, and therefore buoyant, so it will rise back to its original position. Upon returning to the original position, the parcel will still have vertical momentum so it will rise adiabatically past the height at which it is at equilibrium. A parcel forced upwards will be denser than its environment and sink back towards its equilibrium and overshoot the original height in a similar manner. A familiar example of gravity waves is large[1] waves in a pond after a stone or other object is thrown (Figure 3). The stone forces air below the surface of the mean water level disturbing the density equilibrium. In terms of Equation 22, gravity waves are a solution when the viscosity terms and other body forces are eliminated.

Gravity waves, Kelvin–Helmholtz (KH) instabilities, inertial waves, and mountain waves are all forms of atmospheric waves. KH waves are formed in the presence of velocity shear in a continuous fluid, or between the interface of two different fluids. KH waves can be recognized by their signature "rolling-up" shape (Figure 4). This shape forms when the KH instability grows and eventually breaks into turbulence (*Sun et al.*, 2015). Inertial waves occur in rotating fluids and are

---

[1]Large meaning having wavelengths greater than approximately 2 cm. At smaller scales, surface tension is a larger force than gravity and buoyancy.

the result of the Coriolis force. Mountain waves are a special case of gravity waves that occur on the lee sides of mountains that force air up in a stable atmosphere, resulting in an oscillation. Since the mountain does not move, the waves that form are stationary with crests and troughs that do not move but the air moving through the waves does.

Figure 3. Gravity waves in a pond propagating from a central disturbance. Image is courtesy of Dr. Larry Braile, Purdue University.

Gravity waves are ubiquitous in the atmosphere (*Nappo*, 2012). They occur internally when natural density gradients are perturbed (*Sutherland*, 2010). Perturbations may be the result of shear (*Lilly*, 1986), flow over barriers (*Durran*,

Figure 4. Kelvin-Helmholtz waves shown by billow clouds. Photograph was taken by Bejamin Foster of UCAR, 9 February, 2004.

2015), or some form of impulse such as nearby convection (*Lane*, 2015). Gravity waves are both longitudinal and transverse (*Blaes*, 2011). Waves are referred to as transverse when the motion of the particles is perpendicular to the direction of propagation such as the waves on a string and longitudinal when the oscillations are along the direction of propagation as in sound waves. Gravity waves propagating horizontally will oscillate both vertically and in the horizontal direction of travel. Atmospheric gravity waves range from hundreds of kilometers down to tens of meters (*Valkonen et al.*, 2010) and have time-scales ranging from a day down to tens of seconds. Gravity waves transport significant amounts of energy and momentum that can lead to convective storms and clear-air turbulence (*Hooke*,

1986). They are a major factor in the overall energetics of the atmosphere (*Beer*, 1974).

Despite their ubiquity and influence, atmospheric gravity waves are rarely seen directly. An exception is when waves are revealed through the formation of clouds at the crests of waves (Figure 5). They can, however, be measured as oscillations in one or more physical parameters such as velocity, pressure, or temperature. In the past, observations of atmospheric waves have been made primarily by in-situ instruments. In-situ measurements are collected as the atmosphere advects by a sensor or on a platform such as on an aircraft that moves a sensor through the atmosphere. The result is time-series data that represent one or a few locations. If temporally coherent waves are present and non-stationary, they can present themselves as distinct oscillations in these temporal data. Waves, however, exist over areas or volumes rather than at single points. This can be seen on large scales in satellite imagery (Figure 6) (*Dewan et al.*, 1998). Temporal measurements of waves are much more common than spatial measurements. There are only a few studies that involve images of clean atmospheric waves on micrometeorological scales due to limits in remote-sensing technology. Here clean waves are defined as those that are readily apparent in data or imagery, that have a number of clearly identifiable crests and troughs, and that are relatively monochromatic. These are in contrast to "dirty" waves which have a small number of oscillations or may not be coherent oscillations. Because the atmosphere supports the production and superposition of waves at a variety of wavelengths, dirty waves are suspected to be the norm and clean waves more rare. Recent advances in active, laser-based, remote sensing have allowed a description of statically stable areas or volumes of the atmosphere that support clean waves with the spatial resolution necessary to resolve waves at those scales.

Figure 5. Photograph of gravity waves made visible by the presence of altocumulus clouds. This occurs when the wave troughs are below the dew point, and the wave crests are above the dew point. Image is courtesy of NOAA.
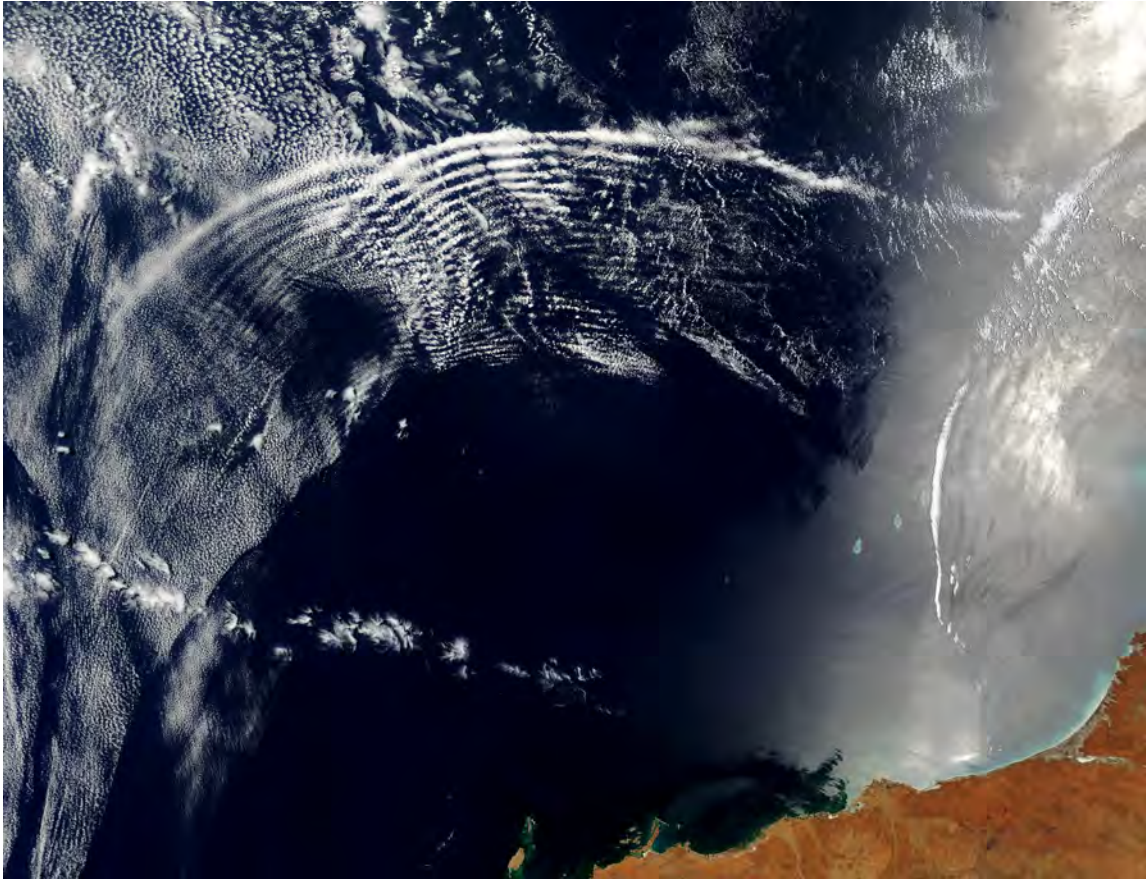
Figure 6. Satellite imagery of gravity waves off the coast of Australia. This image was taken by NASA's Moderate Resolution Imaging Spectroradiometer (MODIS) on 11 November, 2003.

Atmosphere

<u>Structure</u>

The general vertical structure of the Earth's atmosphere can be described in terms of layers. From the largest perspective, a two-layer model can be used to describe the homosphere and heterosphere. The homosphere is the region between the surface and about 85 km altitude where the constituents of dry air (nitrogen, oxygen, argon, etc.) are in constant proportion. Within the homosphere, the general vertical atmospheric structure can be divided into three layers indicated by the sign of the average lapse rate. The lapse rate, Γ, is the rate of decrease in temperature with respect to altitude.

$$\Gamma = -\frac{dT}{dz} \tag{24}$$

If the environmental lapse rate is less than the dry adiabatic lapse rate (DALR), 9.8 K km^{-1}, the atmosphere is said to be statically stable. The upper-most layer of the homosphere is the mesosphere which is about 50 to 85 km above ground level (AGL). In this layer, the temperature decreases with height so the lapse rate is positive, but it is less than the DALR so it is weakly stable. The coldest temperatures in the atmosphere occur at the top of the mesosphere, known as the mesopause. Below the mesosphere, the stratosphere, the middle layer of the homosphere, is located about 10 to 50 km AGL. Here the temperature increases with height so the lapse rate is negative. Therefore, the stratosphere is very stable. The lowest of these three major layers is the troposphere. The troposphere is in contact with the surface of the earth and extends to about 10 km altitude on average. The troposphere, where the majority of atmospheric mass resides, is the layer in which weather occurs. The average environmental lapse rate of the

troposphere is approximately 6 K km^{-1} which is weakly stable. Depending on weather conditions, this lapse rate can vary from unstable to strongly stable.

Potential temperature, θ, is frequently used in meteorology in favor of temperature. It is the temperature an air parcel would have due to adiabatic expansion or compression when moved to a reference pressure, usually the 1000 hPa surface.

$$\theta \equiv T \left(\frac{P_0}{P}\right)^{R_d/c_p} \tag{25}$$

where T is the temperature, P is the pressure of the parcel, P_0 is the reference pressure, R_d is the specific gas constant for dry air, and c_p is the specific heat capacity at constant pressure (*Petty*, 2008).

In the atmosphere, the vertical pressure gradients are balanced by gravitational forces. If the pressure gradient is large compared to viscosity and other body forces, all of the terms on the right side of Equation 22 can be neglected except for the pressure gradient and gravity, and the result is

$$\rho \frac{D\mathbf{u}}{Dt} = -\nabla P + \rho\mathbf{g}. \tag{26}$$

If the parcel is static and gravity only acts in the negative z-direction then

$$\rho g = -\frac{dP}{dz}. \tag{27}$$

If the atmosphere is taken to be an ideal gas, then the state equation is

$$PV = nk_b T \tag{28}$$

where V is volume, n is the number of particles, k_b is the Boltzmann's constant, and T is temperature. For a constant temperature, the solution to Equation 27 becomes

$$P(z) = P_0 e^{-m_u g z/(k_b T)} \tag{29}$$

where P_0 is the pressure at sea level ($z = 0$), m_u is the average molecular mass of air, and k_b is Boltzmann's constant. This is known as the barometric law. Since pressure is proportional to density, Equation 28 can be rewritten as

$$\rho(z) = \rho_0 e^{-m_u g z/(k_b T)}. \tag{30}$$

As a result, density decreases exponentially with height in hydrostatic equilibrium. The reciprocal of the coefficient in the exponential, $k_b T/m_u g$, is known as the scale height. The scale height has a value of about 8.4 km at $T = 288$ K, the average temperature of the atmosphere. So for every 8.4 km in altitude, the density of air decreases by a factor of Euler's number. If the density profile does not match this equilibrium, gravity and buoyancy will work to restore it.

When a parcel is displaced vertically in the atmosphere, its pressure will equilibrate with the pressure of its new environment according to Equation 29, and the parcel will contract or expand. Assuming that this is done adiabatically, meaning there is no thermal energy transfer into or out of the parcel, then the parcel will warm or cool. This results in a lapse rate of

$$\Gamma = \frac{g}{c_p} \tag{31}$$

for the parcel where c_p is the specific heat capacity at constant pressure. For dry air, the specific heat capacity is 1.0035 J g^{-1} K^{-1} making the DALR 9.8 K km^{-1}. If

the environmental lapse rate is less than the DALR, then the atmosphere is statically stable, permitting wave activity. Considering Equation 22 for only the z-direction and neglecting all of the terms on the right side, except the pressure gradient and gravity, and allowing the parcel to accelerate the result is the equation

$$\frac{dw}{dt} = \frac{d^2z}{dt^2} = -\frac{1}{\rho}\frac{\partial P}{\partial z} - g. \tag{32}$$

Using Equation 27

$$\frac{d^2z}{dt^2} = -\frac{1}{\rho}(-\rho'g) - g \tag{33}$$

$$= \frac{\rho'}{\rho}g - g \tag{34}$$

$$= g\left(\frac{\rho'}{\rho} - 1\right) \tag{35}$$

$$= g\left(\frac{\rho' - \rho}{\rho}\right) \tag{36}$$

$$\frac{d^2z}{dt^2} = g\left(\frac{\frac{P}{R_dT'} - \frac{P}{R_dT}}{\frac{P}{R_dT}}\right) \tag{37}$$

$$= g\left(\frac{P}{R_dT'} - \frac{P}{R_dT}\right)\frac{R_dT}{P} \tag{38}$$

$$= g\left(\frac{PR_dT}{R_dT'P} - \frac{PR_dT}{R_dTP}\right) \tag{39}$$

$$= g\left(\frac{T}{T'} - 1\right). \tag{40}$$

Rearranging Equation 25 to

$$T = \theta\left(\frac{P}{P_0}\right)^{R_d/c_p} \tag{41}$$

and substituting gives

$$\frac{d^2z}{dt^2} = g \left(\frac{\theta \left(\frac{P}{P_0}\right)^{R/c_P}}{\theta' \left(\frac{P'}{P_0}\right)^{R/c_P}} - 1 \right). \tag{42}$$

The parcel will equilibrate with pressure on very short timescales so we can say

$$P = P', \tag{43}$$

so

$$\frac{d^2z}{dt^2} = g \left(\frac{\theta}{\theta'} - 1 \right). \tag{44}$$

Taylor expanding the potential temperature of the atmosphere about the temperature of the parcel to first order gives

$$\theta' = \theta + z\frac{d\theta}{dz}. \tag{45}$$

Replacing θ in Equation 44 gives

$$\frac{d^2z}{dt^2} = g \left(\frac{\theta}{\theta + z\frac{d\theta}{dz}} \right) \tag{46}$$

$$= g \left(\frac{1}{1 + \frac{z}{\theta}\frac{d\theta}{dz}} \right) \tag{47}$$

$$\text{if } |\alpha| \ll 1, \text{ then } \frac{1}{1 - \alpha} \approx 1 + \alpha. \tag{48}$$

In the atmosphere over distances on the order of 1 km or less

$$\frac{z}{\theta}\frac{d\theta}{dz} \ll 1 \tag{49}$$

so Equation 47 becomes

$$\frac{d^2z}{dt^2} \approx -\frac{g}{\theta}\frac{d\theta}{dz}z. \tag{50}$$

This is a common differential equation in the same form as

$$\frac{d^2x}{dt^2} = -\omega^2 x \tag{51}$$

commonly referred to as a simple harmonic oscillator. Its solutions are waves with an angular frequency ω. Therefore, Equation 50 has wave solutions, such as

$$z = A_z \sin(Nt) \tag{52}$$

where A_z is the amplitude of displacement, which oscillate at an angular frequency, N, which is known as the Brunt–Väisälä (BV) frequency. Specifically,

$$N = \sqrt{\frac{g}{\theta}\frac{d\theta}{dz}}. \tag{53}$$

Since the potential temperature is approximately equal to the temperature near the surface, it can be shown that

$$T \approx \theta \tag{54}$$

and

$$\frac{d\theta}{dz} = \frac{dT}{dz} + \Gamma. \tag{55}$$

This leads to the relationship

$$N \approx \sqrt{\frac{g}{T}\left(\frac{dT}{dz} + \Gamma\right)} \approx \sqrt{\frac{g}{T}\left(\frac{\Delta T}{\Delta z} + \Gamma\right)} \tag{56}$$

that include finite differences rather than infinitesimal changes so that this equation can be used with real data. The BV frequency is an angular frequency. Since the period is the time of one cycle it follows that

$$\tau = \frac{1}{f} \tag{57}$$

so a theoretical period can be calculated from Equation 4 to be

$$\tau = \frac{2\pi}{N} \tag{58}$$

as shown in Figure 7. For gravity waves, this is the lower bound on period and leads to the upper bound on frequency. This model is only an approximation because it does not account for friction or compensating motions of the environment.

When waves are observed in the real atmosphere and the wind is blowing, the trajectory of a parcel is the result of the wave motion and the wind. Considering a parcel with vertical motion determined from Equation 52 while confined to a horizontally traveling wave, the parcel's trajectory will also be a wave in space with a wavelength longer than the wavelength inferred from an image of the waves at a given time. The parcel will travel one wavelength plus the distance the wave travels in one cycle, $v_p\tau$ (Figure 8). From here forward, the parcel's Lagrangian properties will be referred to as intrinsic. Therefore, the intrinsic wavelength, λ_i, is

$$\lambda_i = \lambda + v_p\tau. \tag{59}$$

Airy wave theory, also referred to as linear wave theory, is a linearized description of gravity waves. The theory predicts most of what is known about gravity waves today (*Nappo*, 2012). According to Airy wave theory, waves can

transport kinetic energy and momentum vertically, but they do not transport other scalars such as heat and constituents. This is shown by a 90° phase shift between vertical velocity and temperature. These properties do not necessarily extend to nonlinear waves (*Stull*, 1988). A 90° phase shift between horizontal and vertical velocity results in no momentum flux (*Lee et al.*, 1996).
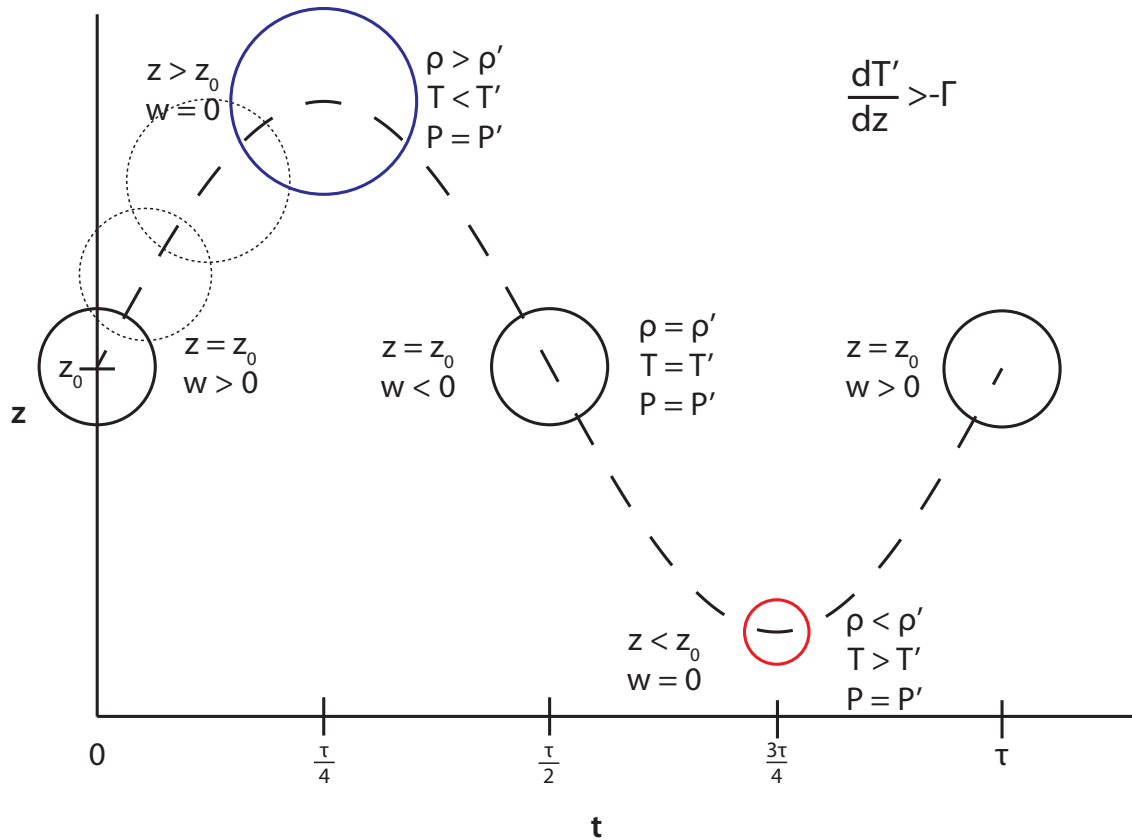
Figure 7. Idealized vertical motion of a parcel in a stably stratified fluid with no dissipation, mixing, or compensating motions through time. Here, the parcel is initially perturbed with a positive vertical velocity. As the parcel rises, it adiabatically expands and cools. Above the initial height, z_0, the parcel will be more dense than the local environment, indicated by primes ($'$), so the net force will be downward. As it sinks, its momentum will carry it past z_0 resulting in adiabatic compression, warming, and a net buoyant force upward. The period, τ, is found by Equation 58. Figure adapted from *Hooke* (1986).
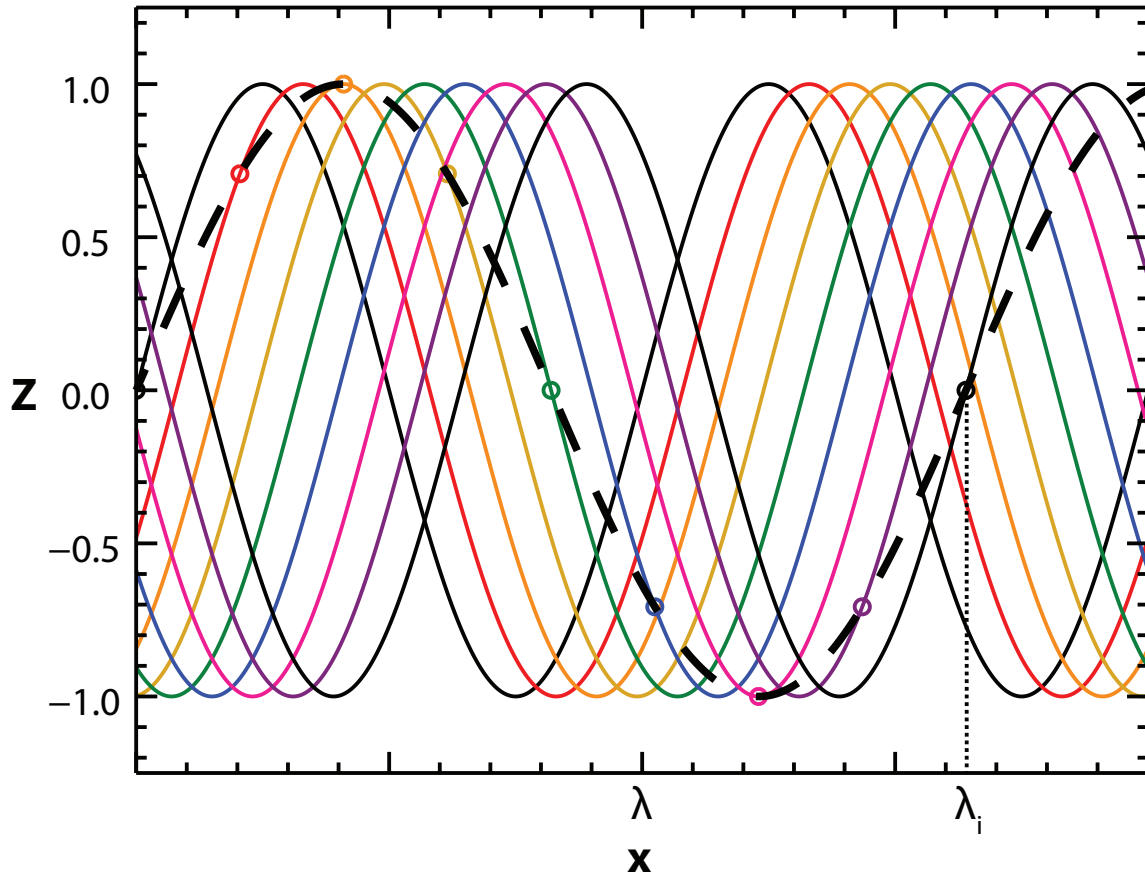
Figure 8. (Color required.) Idealized oscillating parcel in space when confined to a traveling wave. Solid colors indicate the observed wave at different times. The time interval is $1/8^{\text{th}}$ of a period as determined by Equation 58. On each solid line, there is a small circle representing the position of a parcel at each time. The dashed line shows the trajectory of the parcel. The wave moves to the right at velocity, v_p, while the parcel moves through the wave at a slightly higher velocity, leading to an intrinsic wavelength which is greater than the observed wavelength.

Atmospheric Boundary Layer

Moving fluids in contact with rigid surfaces form boundary layers. The earth's atmosphere moving against the surface of the earth is no exception. At the bottom of the troposphere is the atmospheric boundary layer. Its depth is variable in both location and time. The depth depends on the roughness and temperature of the earth's surface relative to the air above it.

Boundary layers are significant because they control the vertical flux of momentum, thermal energy, and concentrations of constituents such as trace gases and pollutants. In order to model the earth's climate correctly, it is critical to understand boundary layer vertical fluxes. For instance, the surface of the earth is a sink of momentum because it imposes drag on the atmosphere, it is a source of water vapor through evaporation, and it is a source or sink of thermal energy when the atmospheric temperature is different from the surface temperature. Without turbulence, the vertical communication through the laminar boundary layer would be limited by vertical molecular diffusion, which happens on very slow time scales.

Convective Boundary Layer

During the day, the surface of the earth is warmed due to radiation from the sun. The surface warms the adjacent air through conduction, causing the air at the surface to reach the maximum temperature in the afternoon. During the day, the temperature of the air tends to decrease with height. This drives convection in the bottom of the atmosphere on the order of 1 km. This is known as the convective boundary layer (CBL). It can be divided into two sublayers: the mixed layer and the surface layer.

The mixed layer (ML), as its name suggests, is well mixed due to turbulence from the convective forcing of the earth's surface (*Kaimal and Finnigan*,

1994) or wind shear. This layer makes up the majority of the CBL and spans altitudes ranging approximately from 100 m to 1 km AGL. On average, momentum, potential temperature, moisture and pollutants are vertically uniform in the mixed layer. Even though it is non-deterministic, the mixed layer is relatively well understood because of robust statistical descriptions of turbulence.

The surface layer is the bottom 10% of the atmospheric boundary layer. When the boundary layer is convective, the surface layer is approximately 100 m deep. Here, the mean potential temperature may decrease slightly with height. When perturbed vertically from this equilibrium state, an air parcel that moves down will be colder, and therefore denser, than its new environment which leads to further sinking. Similarly, air that is forced up is warmer and less dense than its new environment so it will continue to rise. This type of non-linear behavior leads to convection, turbulence, and efficient vertical heat flux. This type of atmosphere is described as unstable where the change in potential temperature with respect to altitude is negative ($d\theta/dz < 0$). The surface layer's momentum is also not well mixed. Since the ground is not moving but the winds aloft are, the atmosphere is constrained on one side by a no-slip boundary condition, leading to a log wind profile where the speed increases logarithmically with altitude (*Boyce and DiPrima*, 2004).

Nocturnal Boundary Layer

In contrast to the mixed layer, the stable boundary layer (SBL) is not very well understood (*Nieuwstadt*, 1984). This relatively shallow layer is characterized by a stable temperature profile ($d\theta/dz > 0$), suppressing turbulence (*Mahrt*, 2014). Typically, the nocturnal boundary layer (NBL) is statically stable, so from here forward, NBL will refer to a stable boundary layer. In a statically stable environment, potential temperature increases with height. If a parcel of air is

perturbed downward, warm air will find itself in a colder, denser environment than it was previously, so it will become buoyant and rise back towards its original position. Air that rises will be colder and denser than its new environment and therefore tend to sink back to its original position. If underdamped with enough static stability, these parcels will overshoot their original position and move to a location where they are again, out of equilibrium, setting up an oscillation. These are gravity waves.

In the NBL, the winds aloft at approximately 100 m to 300 m AGL can accelerate to supergeostrophic speeds in the nocturnal low-level jet while the winds near the surface slow (*Stull*, 1988). The result is a strong shear profile. The nocturnal boundary layer over flat barren terrain typically follows a log wind profile. However, stratification can lead to decoupling of different layers of air and may generate short sporadic bursts of turbulence. The shear-induced turbulence rapidly reconnects the layers. A stable environment in the presence of perturbations may cause oscillations. Very stable environments can trap high-frequency waves in the NBL surface layer (*Stull*, 1988). One type of high-frequency wave is canopy waves which occur in the stable, nocturnal, atmospheric, boundary layer at the microscale.

Atmospheric Scales

Atmospheric motions, such as circulations and waves, span many orders of magnitude in distance and time. When referring to meteorological scales, length scales and time scales increase almost linearly such that if a length scale is increased by a factor of ten, the time scale is also increased by a factor of ten. As a result, atmospheric phenomena tend to fall along a line with a slope of 1 m s^{-1} when plotted on a space versus time graph. This ratio is not valid at and below the Kolmogorov scale (*Kolmogorov*, 1941) and deviates at longer timescales for

processes like seasons and climate change (*Stull*, 1988). At the largest scales where the atmosphere can be regarded as a two-dimensional fluid, characteristic length scales can be as large as the circumference of Earth (on the order of 10^7 m) and time scales on the order of weeks (one week is 6.048×10^5 s). This is referred to as the planetary scale where the Coriolis force due to the rotation of the earth is dominant. At smaller scales, the rotation of the earth becomes less important and the three-dimensional nature of the atmosphere must be taken into consideration. Rossby waves, a subset of inertial waves, occur at this scale. Cyclones and anticyclones are phenomena at the synoptic scale of approximately 10^6 m to 10^7 m and on the order of days. This is the scale that is most critical for weather forecasting. The mesoscale spans 10^3 m to 10^6 m, occurs on timescales from hours to days, and includes phenomena such as land and sea breezes, lee waves, and thunderstorms. The microscale covers all length and time scales ranging from the Kolmogorov scale at about 10^{-3} m to about 10^3 m. Phenomena within this scale include turbulent coherent structures within the planetary boundary layer and the internal gravity waves reported herein.

Canopy waves

Canopy waves are a type of microscale gravity wave. They exist on scales on the order of 10 m to 100 m with periods on the order of minutes. They occur in the stable layers directly above forest canopies, whether that is a natural forest or an orchard. Canopy waves are thought to be the result of a shear instability in a statically stable environment (*Lee et al.*, 1996). The Richardson number is a measure of the ratio of the temperature gradient to the shear expressed as

$$Ri = \frac{N^2}{\left(\frac{du}{dz}\right)^2}. \tag{60}$$

A Richardson number dropping below a critical value, generally accepted as 0.25, creates a shear instability (*Kaimal and Finnigan*, 1994). The instability creates oscillations in the air immediately above the canopy top. The instability will first occur at the height where the horizontal wind shear in the vertical oriented streamwise, du/dz, is at a maximum. The maximum of the shear occurs where its derivative with respect to height, d^2u/dz^2, is equal to zero. This is an inflection point in speed by definition. In a uniform idealized fluid with one no-slip boundary at the bottom and a moving atmosphere at some height, there is a log wind profile with no inflection point in the wind. However, the drag induced by the canopy reduces the wind speed in the canopy, causing an inflection point just above the trees (Figure 9). At the height of the inflection, the canopy waves are generated and should have the maximum amplitude (*Einaudi and Finnigan*, 1981). The wind speed at this height is thought to be the speed at which the waves propagate (*Lee et al.*, 1997).
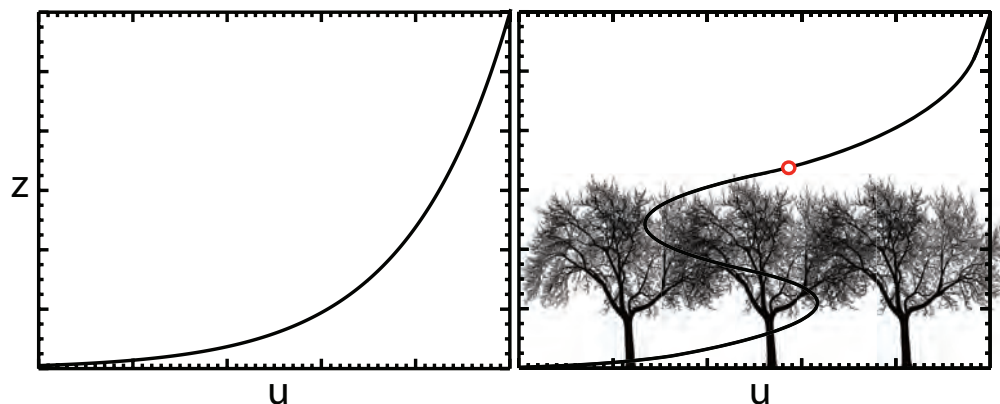

Figure 9. Left panel: Height versus mean wind speed for a barren surface resulting in a log wind profile with no change in concavity. Right panel: Foliage of canopy produces an elevated layer of drag and an inflection point instability just above the canopy.

There are two types of perturbations that induce gravity waves, internal and external. Shear is the only internal perturbations for gravity-wave induction. External forces could be but are not limited to convective or topographical (*Lane*, 2015). To illustrate conceptually how shear generates waves, consider two parcels of equal mass moving horizontally at different speeds and different altitudes, where the higher parcel is moving faster than the lower parcel (Figure 10). In a viscous fluid, there is a shear force between these two parcels that will decelerate the top parcel and accelerate the bottom parcel. The shear force will be the only force considered here, neglecting pressure gradients and gravity. Considering only linear forces on the parcels, the two parcels will approach the same speed which would be the average of the two initial speeds conserving linear momentum, eliminating the shear and allowing the parcels to continue traveling horizontally at constant speed. Angular momentum, $\mathbf{L}$, is defined as

$$\mathbf{L} = \mathbf{r} \times \mathbf{p} \tag{61}$$

where $\mathbf{p}$ is the linear momentum and $\mathbf{r}$ is the radius or distance from the origin, defined classically as

$$\mathbf{p} = m\mathbf{v} \tag{62}$$

where m is mass, so

$$\mathbf{L} = \mathbf{r} \times m\mathbf{v} \tag{63}$$

$$\mathbf{L} = m\mathbf{r} \times \mathbf{v}. \tag{64}$$

The system of two parcels initially has some nonzero angular momentum in all reference frames. The situation with two parcels moving horizontally at equal

speed will have zero angular momentum in a frame whose x-axis is aligned with the motion of center of mass of the system, violating the conservation of angular momentum. There is not a unique solution that satisfies conservation of both linear and angular momentum, but restricting the parcels to match one another's horizontal speed and keeping the parcels the same distance apart, requires that each parcel reaches some nonzero vertical velocity that is equal to and opposite that of the other parcel to conserve the vertical component of linear momentum. Furthermore, each parcel must be displaced such that the center of mass is still traveling at the average initial velocity to conserve linear momentum, since there are no external forces (*Taylor*, 2005). One solution is an orbital motion of the parcels about their common center of mass translating at the average horizontal velocity of the parcels. If the distance of the parcels to the center of mass stays the same, energy is also conserved.

In reality, there are a very large number of parcels, essential infinitely many, interacting. In a wind profile like those in Figure 9, where there is only a horizontal non-uniform velocity, there is a nonzero angular momentum. If the shear force does any work that causes the horizontal velocity of a parcel to change with respect to other parcels, there will be some vertical velocity induced. This is the simplified mechanism from which shear waves are generated. In the atmosphere there are other forces such as gravity, pressure gradients, and other body forces, that complicate the motion of the parcels.

Canopy waves can be observed in a number of meteorological variables. Fundamentally, gravity waves are due to a density disequilibrium. However, density is not measured directly. Considering the atmosphere to be an ideal gas, the density of a parcel of air depends on both pressure and temperature. Pressure disequilbria are communicated from sound waves on short timescales. Therefore,

the waves can be observed in adequate measurements of temperature. With a density disequilibrium, the air is subjected to unbalanced forces. During equilibrium, buoyant forces are balanced by gravity, so the forces are balanced. When they are out of equilibrium, the forces are unbalanced. Therefore, the parcels are accelerated, so a wave can be observed in wind velocity as well. Since the acceleration is the derivative of velocity and the second derivative of position, and since the position is a superposition of sine and cosine waves, the acceleration is comprised of sine and cosine waves with a 90° phase difference with velocity and 180° phase difference with position. Measurements of these quantities to date have mostly been done in situ providing only temporal data. However, recent advances in remote-sensing technologies provide the possibility for spatial data and analysis that can lead to improved insight into wave structure and dynamics.
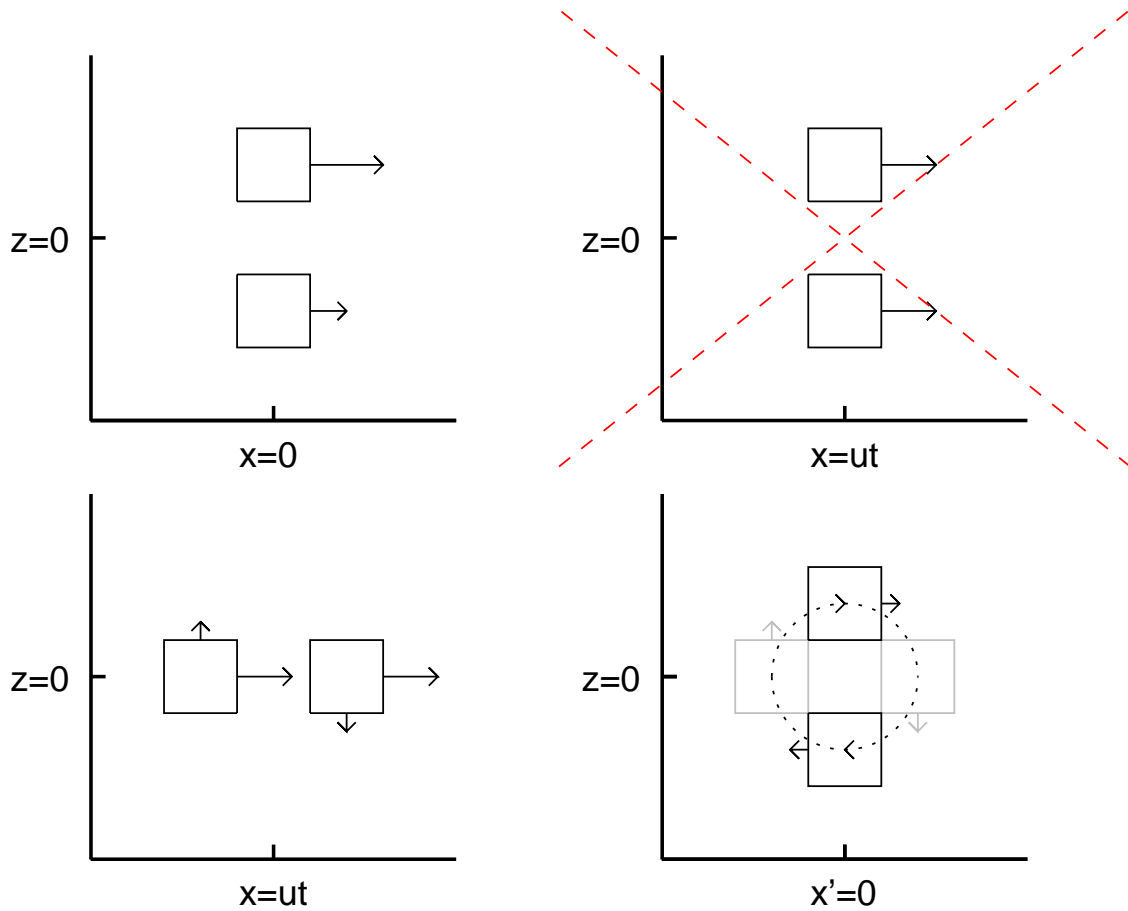
Figure 10. Top left panel: Two parcels traveling horizontally at different speeds exerting a shear force on one another. Top right panel: After some time, t, two parcels whose shear force caused them to reach the same horizontal velocity. However, this violates the conservation of angular momentum. Bottom left panel: In order for a shear force to cause the parcels to match one another's horizontal speed, each parcels takes some nonzero vertical velocity in each parcel to conserve angular momentum. Bottom right panel: A possible orbital trajectory for two parcels with a shear force between them in frame moving at the average speed of the parcels.

Raman-shifted Eye-safe Aerosol Lidar

The Raman-shifted Eye-safe Aerosol Lidar (REAL) (*Mayor et al.*, 2007) is one of these technologies. Lidar (or LIDAR) is an acronym for LIght Detection And Ranging (akin to the Acronym RADAR, RAdio Detection And Ranging). The principle is to transmit pulses of laser radiation into the atmosphere and measure the intensity that is scattered back toward the receiver. The intensity is measured fast enough so that the time delay and speed of light can be used to determine the radial distribution of backscatter with high resolution. By changing the direction of the propagation of the laser beam in azimuth or elevation, a two-dimensional map of the backscatter distribution in the atmosphere can be created. A scan can be repeated every 10 s to 30 s which allows observations of the temporal evolution and propagation of the waves on these timescales.

Canopy waves were discovered in the REAL data collected during the Canopy Horizontal Array Turbulence Study (CHATS) (*Patton et al.*, 2011). From the images created by the REAL, over 50 episodes of microscale gravity waves were cataloged (*Jachens et al.*, 2012, *Randall et al.*, 2012) (Figure 11). Episodes appear as parallel linear bands of high and low backscatter intensity. Previous studies have shown observations in the form of time series, and limited amounts of spatial sampling from previous studies have revealed wave-like oscillations at night in this shallow region above forest canopies (*Bergström and Högström*, 1989, *Cava et al.*, 2004, *Fitzjarrald and Moore*, 1990, *Kaimal and Finnigan*, 1994, *Lee*, 1997, *Lee and Barr*, 1998, *Lee et al.*, 1997, *Van Gorsel et al.*, 2011). Few studies of waves have been done using lidar. *Newsom and Banta* (2003) used a Doppler lidar to measure a 60 min wave episode during the 1999 Cooperative Atmosphere–Surface Exchange Study (CASES-99) (*Poulos et al.*, 2002). No study could be found using lidar to

measure canopy waves. This may be due to the difficulty associated with making images of atmospheric structures on a nearly horizontal plane just above the treetops. Capturing microscale waves requires high resolution and high signal-to-noise ratio. Eye-safety is also very advantageous as it permits unattended operation for long periods of time.

Previous studies using images produced by direct-detection lidars have described the aerosol distribution in the lower turbulent atmosphere, both spatially and temporally. Statistical methods such as autocorrelation (*Ferrare et al.*, 1991) and cross-correlation (*Mayor et al.*, 2003) have been applied to the backscatter fields in order to quantify the aerosol features in terms of their size and velocities. These techniques were typically used for unstable, turbulent, convective conditions and have not been applied to lidar observations of gravity waves since there have been no previous two-dimensional direct detection images of microscale waves to date.
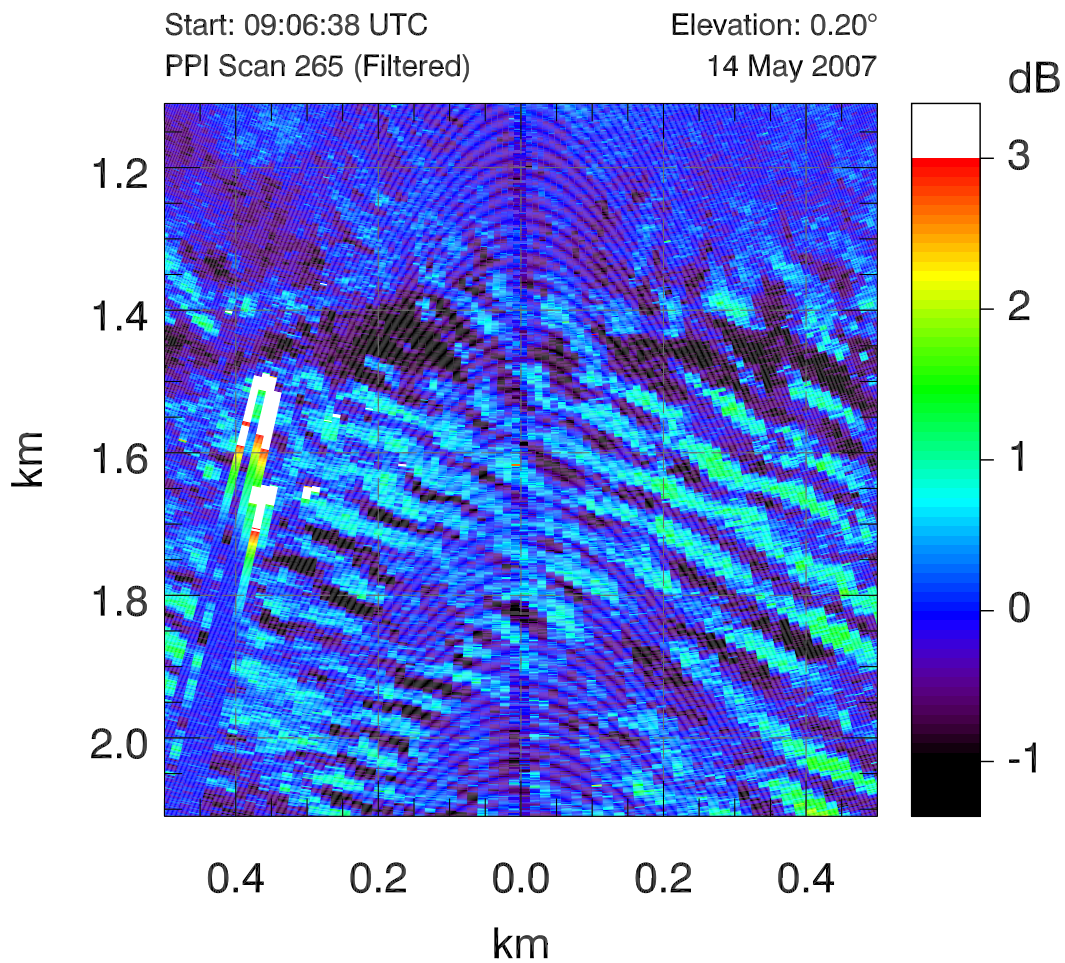
Figure 11. (Color required.) A square kilometer of a horizontal scan from the REAL on 14 May 2007, revealing canopy waves in the high-pass median filtered backscatter signal. Such images can be used to determine wavelength. In this case, the wavelength is approximately 60 m.

Motivation

To accurately simulate the atmosphere, the physical processes that transport thermal energy, momentum, and trace gases must be quantified. For example, thermal energy can be transported by conduction, radiation, turbulent mixing, or the mean flow. Momentum can be transported through viscous dissipation and turbulence. Models require proper boundary conditions and parameterizations of subgrid-scale processes. Boundary conditions are the variables and numerical procedures that exist on the edges of the modeling area or volume. They may specify a value of some quantity on the edge, referred to as Dirichlet boundary conditions, or a quantities derivative with respect to time on the edge, referred to as Neumann boundary conditions. The quantities can be temperature, pressure, velocity, or other relevant observables. Subgrid-scale parameterization is required for phenomena that occur at length scales smaller than the grid spacing of simulation. If a process is a source or sink of energy that is not explicitly resolved by the grid, the gain or loss of energy must be parameterized (*Stensrud*, 2007). Since the observed canopy waves are small with respect to many model grid spacings, such as weather and climate models, their contributions to fluxes of heat, momentum and trace gases must be parameterized. Developing a parameterization for the waves is beyond the scope of this study, but one motivation is to determine the possible impact of the waves on fluxes.

Studies of the NBL are far fewer than studies of the CBL. Specifically, the exchange between forest canopies and the atmosphere has been rigorously studied for daytime turbulence, but the exchange during night has not been the focus of nearly as many studies (*Hu*, 2001). The combination of in-situ and remote-sensing data allowed comparison of what theory predicts spatial structure

should be based on in-situ temporal oscillations to remote-sensing spatial observations. Since these are unique spatial observations, validating them is non-trivial because there are no direct comparisons that can be made. Also, objective techniques are generally favorable to subjective ones, so the development of algorithms to determine these quantities was desired.

Hypothesis

The first possibility addressed in this research is that the observed waves may not be a real physical phenomenon, but rather some artifact of the lidar system. This question can be resolved by examining the complementary in-situ data. If oscillations exist in this temporal data during wave episodes that are not present at other times, the evidence will strongly point toward the existence of natural fluid waves.

The next issue to investigate is why the REAL is capable of detecting canopy waves. During the evening and night, the earth's surface and atmosphere cool due to the emission of long-wave radiation. The earth's surface cools faster than the air, resulting in a temperature inversion starting from the ground up. The atmospheric surface layer tends toward static stability where the lower atmosphere becomes stratified and horizontally homogeneous in terms of temperature, relative humidity (*Kaimal and Finnigan*, 1994), and aerosol concentration. Stable stratification and weak flow are likely to result in the formation of vertical gradients of aerosol backscatter that are approximately horizontally invariant. However, the variation in these properties may change significantly with height (Figure 12). As the night progresses, the stable stratification strengthens resulting in frictional decoupling (*Blackadar*, 1957), leading to even more vertical wind shear. The shear can induce wave motion as described previously. The aerosol field

will be displaced vertically by the shear-induced internal gravity waves. The aerosol that was horizontally invariant now becomes corrugated and volumes of high aerosol concentration are pushed up with rising air and low aerosol concentration are pulled down by sinking air. Therefore, aerosols can serve as tracers of wave activity. The horizontally scanning lidar beam will propagate through peaks and troughs of aerosol concentration resulting in a non-uniform backscatter field and reveal the waves as shown in Figure 11. If this is the case, the backscatter intensity should be in phase with the position of air parcels, and therefore 90° out of phase from the vertical velocity.
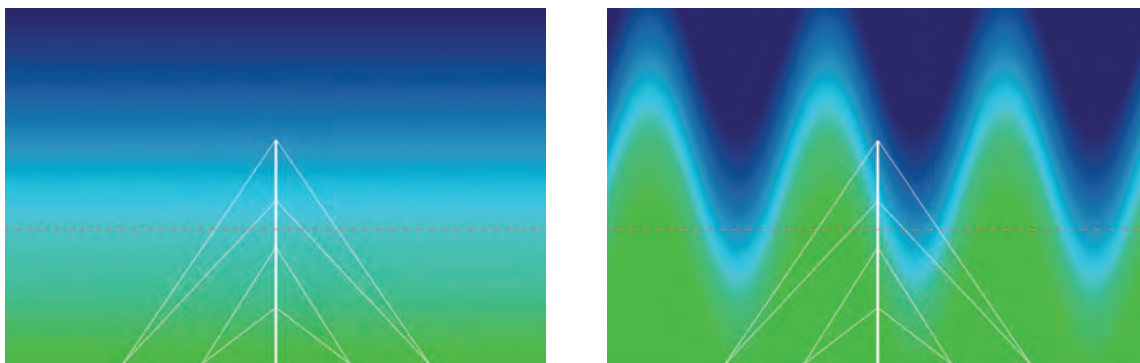

Figure 12. (Color required.) Left panel: Artist conception of a hypothetical vertical cross section of the backscatter from the lower atmosphere (from the surface to about 50 m AGL) as observed in the REAL data that may occur at night during quiescent conditions. The horizontal line is the approximate altitude of the horizontal lidar scans. Right panel: The same cross-section as the left image but with canopy waves displacing the local atmosphere and aerosol gradient vertically.

Furthermore, the research will show whether the wave characteristics can be both subjectively and objectively described. Once the waves are identified in the REAL data, the corresponding tower data collected during the same time frame

can be retrieved. First, the presence of the waves in the in situ vertical velocities, horizontal velocities, and temperature can confirm a dynamical cause which shows that the waves are not an artifact of the lidar system. With the in-situ data, temporal calculations, such as momentum and thermal flux, can be made. Also, the period of the waves can be determined either by subjective inspection, or more objectively with autocorrelations or discrete Fourier transforms.

The images created by the REAL contain quantitative information about the waves. The relevant quantities that can be uniquely described from the lidar images are the wavelength and phase speed. The wavelength of the waves is apparent in the images produced by the lidar data and the speed at which they move can be deduced from the animations that are subsequently created from these images. However, subjective inspections are prone to biases and errors, so objective algorithms are preferred.

Given a single image, the wavelengths of the canopy waves can be determined through subjective inspection by measuring the distance between wave crests, or through more objective algorithms, such as autocorrelation. Given several images, the wavecrests' translation can be tracked over time, which leads to a phase speed and direction. Again, this can be done subjectively or objectively. Subjective methods involve tracing wave fronts as they move from each image to the next, measuring their displacement with a ruler over a known interval of time. Objective methods involve cross-correlation between two sequential images. With phase speed and wavelength, the period of the waves can be calculated through the relationship

$$\tau = \frac{\lambda}{v_p}. \tag{65}$$

Hence, using only lidar data, a period can be identified that can be compared with the value determined from the in-situ tower data. For mechanical waves, the phase speed is typically measured with respect to the medium. For gravity waves with a background wind, the air in which they are propagating is also moving. This means that a stationary observer, such as in-situ sensors on a tower, would measure a higher frequency and a shorter period than an observer moving with the wind. An intrinsic period, τ_i, can be defined as

$$\tau_i = \frac{\lambda}{v_p - u_0} \tag{66}$$

where u_0 is the background wind speed.

The waves' propagation direction appears to be in the direction of the wind based on the relative motion of wavecrests and the surrounding aerosol features in the images of aerosol backscatter created by the lidar. This will be verified by subjective and objective determination of the propagation direction to be compared with the in-situ measurements of the wind velocity.

Since, by definition, canopy waves occur only over forest canopies, it is hypothesized that the canopy induces an inflection point in the mean wind speed profile. It is at this height that the waves are generated. As a result, the wave amplitude should be greatest at this height. Some amplitude should be observed in several of the quantities measured, but close attention will be given to vertical velocity since horizontal velocity and temperature may likely be subject to linear or higher order trends.

Given that waves occur in stably stratified fluids, they do not serve to transport heat or trace gases. If they are evanescent they will not transport energy or momentum vertically.

Literature Review

Quantitative gravity wave observation dates back at least as far as the 1950's when *Gossard and Munk* (1954) observed waves with a barograph and a damped anemometer. These waves had periods on the order of 10 min and occurred with wind speeds from 0.7 m s^{-1} to 2.9 m s^{-1} and occurred over the ocean. Since then, the field has advanced extensively with the use of technology, both in-situ and remote-sensing, computational power, and the evolution of Airy wave theory (*Nappo*, 2012).

Wave motion above plant canopies in the nocturnal boundary layer has been observed in time-series data for at least the last three decades. Periodicity was found in time series of velocities and scalars (*Fitzjarrald and Moore*, 1990, *Paw U et al.*, 1992). The largest body of work on canopy waves appears to have been done by X. Lee. His work dealt largely with data that were collected during BOREAS (BOReal Ecosystem-Atmospheric Study), a 1994 field campaign performed in an aspen forest in the Prince Albert National Forest in Saskatchewan, Canada where trees were approximately 21 m tall. In the experiment, in-situ sensors of 3-D wind velocity and temperature were recorded from a single 40-m-tall tower. During the experiment, there were many wave episodes, but two 60-minute canopy wave events, referred to as event A and event B were studied extensively. These events occurred on 13 July and 4 August 1994.

The period and amplitude were determined from spectral analysis. The period of events A and B were 59.2 s and 60.0 s. In previous work Lee showed that this was shorter than the period from the Brunt–Väisälä frequency, making the argument that these are not purely gravity waves (*Lee et al.*, 1996). The maximum temperature amplitude for event A was 1.49° at 39.1 m and 0.77° at 27.7 m for

event B. The maximum amplitude in vertical velocity was 0.68 m s^{-1} and 0.30 m s^{-1} for events A and B, both at the 27.7 m height. Wave phase speeds and wavelengths cannot be measured from a single point, so Lee used two spectral analysis techniques, one he developed and another from previous literature (*Gossard and Munk*, 1954, *Hooke et al.*, 1973) to estimate the wavenumber and wavelength. The one he developed started from the linear wave equation for potential temperature expressed as

$$\frac{\partial \tilde{\theta}}{\partial t} + \bar{u}\frac{\partial \tilde{\theta}}{\partial x} + (\frac{\bar{\theta}}{g}N^2)\tilde{w} = 0. \tag{67}$$

Expressing all relevant quantities in the form

$$a = \bar{a} + \tilde{a} \tag{68}$$

$$\tilde{a} = \hat{a}(z)e^{i(kx-\omega t)} \tag{69}$$

where a is some complex parameter, $\hat{a}$ indicates the maximum perturbation from the mean, $\bar{a}$ is the average and $\tilde{a}$ is the oscillation about the mean. Solving Equation 67 gives an expression for the amplitude of θ as a function of wavenumber,

$$A_\theta = \frac{A_w}{[(\bar{u}k - \omega_r)^2 + \omega_i^2]^{\frac{1}{2}}}\left(\frac{\bar{\theta}}{g}N^2\right) \tag{70}$$

where A is $|\hat{a}|$ or the amplitude of the wave in the subscripted quantity. Assuming the imaginary part of angular frequency, ω_i, to be small and solving for the wavenumber yields

$$k = \frac{1}{\bar{u}}\left(\omega_r + \frac{A_w}{A_\theta}\frac{\bar{\theta}}{g}N^2\right). \tag{71}$$

Lee followed *Hooke et al.* (1973) as an alternate approach to determine wavenumber with the equation

$$\frac{N^2}{(k\bar{u} - \omega_r)^2} - 1 = \left(\frac{A_u}{A_w}\right)^2. \tag{72}$$

Solving for k gives

$$k = \frac{1}{\bar{u}}\left(N\left[\left(\frac{A_u}{A_w}\right)^2 + 1\right]^{-\frac{1}{2}} + \omega_r\right). \tag{73}$$

Combined with period, he calculated the phase speed. Lee calculated the wavelengths to be 130 m for event A and 65 m for event B. Phase speed for event A was determined to be 2.2 m s^{-1} and event B was 1.3 m s^{-1}. The wavelengths and phase speeds were calculated from two different methods for three heights, resulting in six values. For the event A, the phase speed reported was the average of the four values from the top two heights. For the second case, the phase speed was the average of the results from the two methods from only the 27.7 m height. Lee reasoned that the equations were not valid for the data collected at the 5.5 m height since it was in the trees and that turbulence contaminated the top height in event B. In both cases, the phase speeds calculated varied by a large fraction of the reported value (2.07 m s^{-1} to 2.61 m s^{-1} for event A and 1.16 m s^{-1} to 1.45 m s^{-1} for event B) (*Lee et al.*, 1997). Considering that the two cases used a different treatment, and that the calculation was inconsistent, it appears that these methods can be used only as a rough estimate of phase speed and wavelength.

Lee subsequently developed a linear model of canopy waves. This work concluded with a few key components of canopy waves. Among these conclusions, he found the main role of the canopy was to induce drag that creates an inflection point in wind profiles that otherwise would not exist. He found that the phase speed was always higher than the wind speed at canopy top (*Lee*, 1997). This

research aims to show that the first statement is correct, but that the second is not always true. Further analysis of the BOREAS data attempted to establish the climatology of these waves (*Lee and Barr*, 1998). The study asserted that waves occurred on 40% of nights, the waves had a phase speed that typically matched the wind speed at 1.2 to 1.8 times the canopy height, and that the waves were coherent in less than one wavelength. The lidar images clearly disagree with the last claim. The data from CHATS show a coherence length that can be tens of wavelengths long. This may be due to the uniformity of the orchard canopy versus a natural aspen forest canopy. The phase speed described by Lee may also be unreliable due to the lack of spatial data.

One of the largest studies of the NBL was the Cooperative Atmosphere-Surface Exchange Study (CASES-99) conducted in 1999 in southeastern Kansas (*Poulos et al.*, 2002). The goal was to study turbulence-producing phenomena with four main scientific goals. The first, which was most relevant to this study, was to study internal gravity waves, Kelvin-Helmholtz waves, and turbulence events along with their heat, moisture, and momentum fluxes and time history. The other focuses of the study included: how the heat and momentum flux divergences departed from similarity theory under stable and very stable conditions; the importance of surface heterogeneity; and the acquisition of data during the transition to and from the stable boundary layer. Like CHATS, CASES-99 deployed a variety of instruments both in situ and remote sensing. In CASES-99, the National Oceanic and Atmospheric Association (NOAA) deployed the High-Resolution Doppler Lidar (HRDL) (*Newsom and Banta*, 2003). The HRDL detected microscale waves with wavelengths between 350 m and 400 m. Like the canopy waves discovered in CHATS, these waves are shear generated in the nocturnal boundary layer. However, the shear was generated by a low-level jet

rather than drag from the trees. A Doppler lidar only provides the radial velocity, or line-of-sight velocity. Therefore, unless the waves are propagating in the radial direction with respect to the HRDL, only a fraction of the full wind velocity vector would have been captured. Also the HRDL was performing RHI scans so the vertical structure was observed rather than the horizontal. These are the only spatial images of microscale waves that could be found in the literature review.

CHAPTER II

DESCRIPTION OF THE EXPERIMENT

CHATS

The Canopy Horizontal Array Turbulence Study (CHATS) (*Patton et al.*, 2011) in Dixon, California was a 3-month field campaign from 15 March through 11 June, 2007 to study the micrometeorology in and above forest canopies. The study deployed a multitude of sensors, mostly in situ with some remote-sensing instruments. Among these instruments was the Raman-shifted Eye-safe Aerosol Lidar (REAL). The REAL operated nearly continuously for the duration of CHATS, day and night, over a 10-m-tall walnut orchard such that the sector of each nearly horizontal scan was centered on a 30-m vertical tower at a range of 1.61 km (1 mile). The vertical tower was equipped with an array of meteorological sensors that measured three-component velocity, temperature, relative humidity, and pressure at various heights.

The CHATS site was chosen for its uniformity and flatness. The orchard block was 1.6 km by 1.6 km and less than 1 m difference in elevation over the entire orchard. The study mainly focused on the 800 m by 800 m Cilker Orchards in the NE corner of the orchard block. The trees were planted in a near-square configuration. They were spaced 6.8 m apart in the north-south direction and 7.3 m in east-west. The canopy had an average height of about 10 m. Vegetation was nearly homogeneous except for a few trees that were lost or replanted. Winds from the site were typically 50% out of the north and 50% out of the south with a small

westerly component according to data collected over 24 years by the California Irrigation Management Information System (CIMIS) for Davis, California, the nearest urban area to Dixon. The experiment focused on periods when the winds were from the south because they tended to be weaker and with less variation in the direction. The tower was placed closer to the north side of the orchard for maximum fetch from these southerly winds.

The Raman-shifted Eye-safe Aerosol Lidar (REAL) (*Mayor et al.*, 2007) was used for this study. The advantage of using a laser over microwaves is that a laser beam is very narrow and provides high spatial resolution. The principle is to transmit laser radiation into the atmosphere and measure the intensity that is scattered back toward the receiver. The intensity is measured fast enough so that the time delay and speed of light can be used to determine the radial distribution of backscatter. By changing the direction in azimuth (angle about the z-axis) or elevation (the angle from the xy-plane), a two-dimensional map can be created of the backscatter distribution in the atmosphere. This can be repeated on periods of every 10 to 30 s which permits the observation of the temporal evolution and propagation of the waves. Placing the REAL at the CHATS experiment site had several goals. The first goal was to create time-lapse visualizations of turbulent coherent structures (*Patton et al.*, 2011).

The REAL, the lidar system that detected the microscale gravity waves, is a ground-based, scanning lidar. This provides a stationary origin with a circular sector of data with a range of up to approximately 5 km depending on atmospheric conditions. The REAL operates at an eye-safe wavelength of 1.54 μm. This wavelength is within a narrrow range of wavelengths that enables transmission of high pulse-energy beams according to the American National Standard for Safe Use of Lasers (ANSI 2000) (*Mayor et al.*, 2007). This wavelength is achieved in the

lidar transmitter by directing a 1.064 μm-beam produced by commercially-available Nd:YAG into a Raman-cell, where the beam is Raman scattered. The first Stokes line is 1.543 μm. The residual 1.064 μm beam is removed which ensures an eye-safe beam. Eye-safety is required because it permits continuous and unattended operation at the energy levels required for this work. The REAL has a pulse energy of approximately 170 mJ, and a pulse repetition frequency (PRF) of 10 Hz. The PRF is one of the limiting factors for the angular velocity of the laser beam. At the lidar, the laser beam diameter ($1/e^2$ distance) is 6.6 cm with a half-angle divergence of 0.12 mrad. This results in a beam diameter of 45 cm at 1.61-km range and 1 m at 4-km range. The laser pulse lasts 6 ns which corresponds to a 1.8-m length. Most scans were made at a rate of $4°$ s^{-1}. The receiver records data at 10^8 samples per second which leads to a radial resolution of 1.5 m. The data is distributed across a 14-bit channel and has no calibration. Therefore, the values given by the REAL have no physical units. High backscatter generally trends with higher concentrations of aerosol particles (*Held et al.*, 2012). The REAL was approximately 1.5 km from the northern edge and center in the east-west direction of a 800 m by 800 m walnut orchard of Cilker Orchards outside of Dixon California.

The REAL was used in conjunction with a the National Center for Atmospheric Research (NCAR) Integrated Surface Flux Facility (ISFF) 30-m vertical tower. The vertical tower was 1.61 km (1 mile) south of the REAL and approximately 100 m south of the northern edge of the orchard and was also centered in the east-west direction (Figure 13). The REAL scanned nearly horizontally with an elevation angle of 0.20° above the forest canopy and intersected the vertical tower at approximately 18 m to 20 m above ground level (AGL)(shown in Figure 14). Unfortunately, the lidar was installed along a trench used for irrigation. The trench was flooded at some point during the CHATS

experiment which caused the soil to become softer on one side of trailer which lead it to tip slightly. The trailer was periodically leveled but without record. Based on geometry, the height of the beam at the range of the tower would change 1 m for every 2 mm the far side of the trailer sank. The scan height was estimated based on hard target reflections from the guy wires, but this information was not available for the entire experiment. The PRF and a scan rate of $4° \text{ s}^{-1}$ resulted in a 11 m spacing between laser pulses at the range of the tower. The vertical tower was equipped with 13 Campbell Scientific CSAT3 3-D sonic anemometers and 13 NCAR-Vaisala hygrothermometers located at heights: 1.5 m; 3 m; 4.5 m; 6 m; 7.5 m; 9 m; 10 m; 11 m; 12.5 m; 14 m; 18 m; 23 m; and 29 m AGL. The anemometers and hygrothermometers record at 60 Hz and 1 Hz, respectively.

Figure 13. Plan view of the experimental area for the 2007 CHATS experiment. The REAL was located 1.61 km directly north of the 30-m-tall NCAR ISFF tower. The analysis of waves was limited to the 1 km² box centered on the tower.
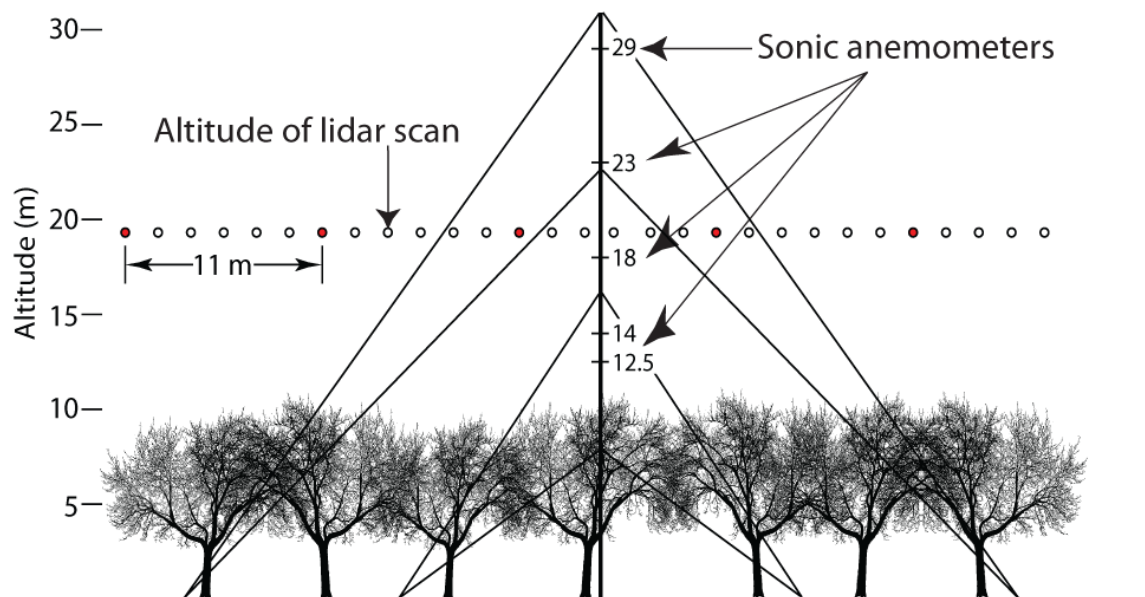
Figure 14. Arrangement of wind, temperature, and humidity sensors above the trees on the NCAR ISFF 30-m tower. Sensors below the canopy top are not shown.

Data

Tower Data

The data from the tower are stored as self-describing netCDF files. Each file contains 4 hours of data and includes the time of the first data point, pressure at 11 m, 3 components (u, v, w) of wind for 13 heights, temperature for 13 heights, slow temperature for 12 heights, and relative humidity for 13 heights. These data sometimes includes fill value of 10^{37} when the instruments did not record a value. Typically, the fill values occupied only one or several consecutive data points. When present, the fill value was removed and replaced with a result from a linear interpolation from the two nearest valid data points. The temperature and relative humidity were recorded at 1 Hz while the velocity data were recorded at 60 Hz. To compare these values and simplify the computation, the 60 Hz data were frequently averaged over one-second intervals to match the 1 Hz data.

Lidar Data

Fifty-two wave cases were identified by subjective inspection of time-lapse animations of aerosol backscatter (Figure 15). The animations were comprised of frames created from the raw lidar data stored in files referred to as BSCAN files. A BSCAN file contains metadata for each transmitted laser pulse from the REAL. It includes the time of the pulse resolved to the ms, the geographic coordinates of the lidar, the range of the first lidar data point relative to a laser trigger, and the range bin size. The coordinates of the REAL during CHATS were 36.7698° N 118.23° W. The range bin size is 1.5 m, determined by the sampling rate of the digitizer in the receiver for the REAL, 10^8 samples per second. Taking the speed of light to be 3.0×10^8 m s^{-1}, and considering the laser pulse makes a

round trip, the bin size becomes:

$$b = \frac{2c}{R_s} \tag{1}$$

where b is the bin size, and R_s is the sampling rate. This is one of several limiting factors for the radial resolution for lidars. The REAL has a large sampling rate yielding small bin size for a very good radial resolution. The rest of the data in a record of a BSCAN file are the backscatter intensity for each sample in range. There are two channels for perpendicular polarization states of the return signal. However, during CHATS the REAL was operated in a mode that was not sensitive to polarization (*Mayor*, 2008). Therefore, the two channels are summed to increase the signal-to-noise ratio by a factor of $\sqrt{2}$. The intensity is related to the voltage as seen by the photodetector. The voltage waveform is read by a 14-bit digitizer and mapped so that it spans the range. The gain is not recorded so the intensity has no physical units. In context, locations of high or low backscatter are observed to study the spatial distribution and movement of aerosol features over time.

The digitizer begins sampling before each laser pulse is emitted so that a background signal can be determined. The mean of the background signal was subtracted from the signal for each laser pulse. Since each aerosol particle acts as a point source of backscattered laser radiation, the radial data is subject to the inverse-square law. Therefore, each point was multiplied by its range squared. The backscatter voltage spanned many orders of magnitude so the logarithm of the intensity, plus an offset to ensure the domain was positive, was taken. Then the logarithm was multiplied by 10, so intensity is reported in units of decibels (dB).

A high-pass-median filter was applied to the raw backscatter data for each radial shot. The filter subtracts from each point the median value over a window centered on that point. The filter had a 333-point-long window, each point

1.5 m apart in the radial direction leading to a window of approximately 500 m. Therefore, the filter removes features that are larger than 250 m.

Like most radars and lidars, these data are natively in spherical coordinates. Each shot records an azimuthal and elevation angle and returns a data point for every 1.5 m in range. The scans are done in conic sections with constant elevation, so the spherical coordinates can be reduced to polar coordinates of a range and one angle, azimuth for Plan Position Indicator (PPI) scans, and elevation for Range Height Indicator (RHI) scans. The filtered data were mapped and interpolated from their native polar coordinates (r, θ) to a 1 km by 1 km Cartesian grid (x, y) with spacing of 1.0 m. The Cartesian resolution was chosen for convenience and is finer than the radial resolution in the original polar coordinates to ensure no loss of information in the transformation.

The circular section for each image in the dataset was cropped to a 1 km by 1 km box that was centered on the tower in order to ensure that the wave cases identified for study could be confirmed and further analyzed with the tower data. These images were encoded into time-lapse animations. Any case that passed over the tower and lasted longer than 1 minute was declared an episode. The wave cases were then cataloged and made available on a website.[1] The date, time, number of frames, and an estimate of wavelength were all recorded.

Spikes present in the lidar data are due to hard-target reflections, specifically due to the tall trees in the northwest area of the Cilker orchards as well as other high-intensity spikes from the tower, guy-wires, or even insects or birds (*Wilczak et al.*, 1996). Therefore, before any further analysis of the wave images, a clipping filter was added to the already high-pass median filtered data. All data points with a value over 1.5 dB were replaced with a zero. Zero was chosen rather

---

[1]Catalog of waves can be found at *http://phys.csuchico.edu/lidar/canopywaves*

than 1.5 in order to ensure that the large hard targets were not a large contributor statistically to the aerosol backscatter intensity field. Once the backscatter intensity fields were high-pass median filtered, mapped, and cleared of large spikes, the waves could be objectively analyzed.
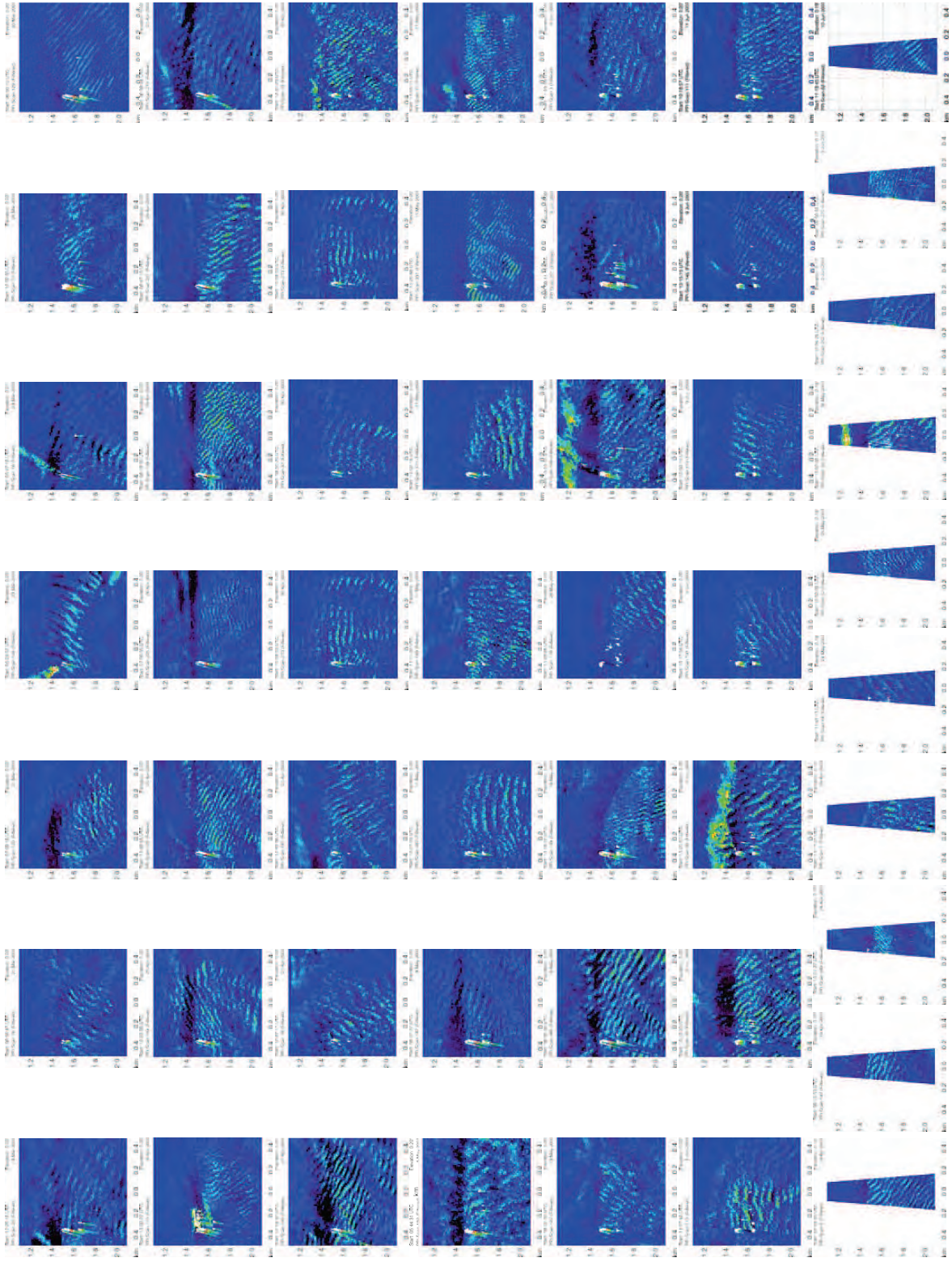
Figure 15. (Color required.) All wave episodes arranged in chronological order and by width of scan.

CHAPTER III

METHODS

Subjective Methods

The nature of the lidar time-lapse data makes it simple for a person to identify phenomena such as waves. Once identified, qualitatively describing phenomena can be much more difficult. To develop new methods to describe phenomena, first subjective estimates were made. The wavelengths of waves were estimated by simply using a ruler to measure distances from crest to crest on images collected by the lidar. The lidar images were plotted on a grid with minor tick marks every 10 m and major tick marks every 100 m for scale. However, the crests were not uniformly distanced from one another, and the high backscatter band took up a finite width that does not have an obvious maximum. These waves were estimated to the nearest 10 m. In addition to estimating wavelengths, the phase velocities were subjectively determined by laying tracing paper on a computer monitor and stepping through sequential frames. By keeping the tracing paper in the same location relative to the image and tracing the same crest, the displacement over time could be calculated. The wave crest was not always recognizable from frame to frame. Also, the efficacy of this method may depend on the choice of wave crest. Combining the estimate of wavelength and phase speed, a period can be determined, but with the error propagated from both of the initial estimates.

Subjective estimates of the period were also made by examining the in-situ tower data. This was done two ways. First, the time from one peak to the next was observed in time-series data. This is the less accurate way compared to the second method. By counting the number of cycles in a longer time frame, the uncertainty in the measurement goes down. This is reliant on a person counting the correct number of cycles which is not always clear. The problems already stated combined with a person's biases or errors in judgment cause these subjective estimates to fall short of more objective means.

Objective Methods

Autocorrelation

Autocorrelation serves as a description of a sequence, S_n, by comparing it with a copy of itself with a shift, or lag, denoted $S_{n+\tau}$. The sequence can be one or more dimensions in time or space with τ having the same dimension and units. For example, a one-dimensional time series will be shifted in time while a two-dimensional image will be shifted in two spatial dimensions. This shift will run from $N - N/2$ to $N + N/2$, where N is is the number of elements in the series. In temporal data, autocorrelation can reveal turbulence time scales or frequency in periodic data. With spatial data, autocorrelation techniques can determine length scales of turbulence or wavelengths of periodic data (Figure 16).

The autocorrelation, A_τ, is typically defined in one dimension as

$$A(\tau) = \frac{\sum_{i=1}^{N-n}(S_i - \bar{S}_n)(S_{i+\tau} - \bar{S}n)}{\sum_{i=1}^{N}(S_i - \bar{S}_n)^2} \tag{1}$$

where N is the number of elements in the series. This method for calculating the autocorrelation for large data sets can become computationally intensive.
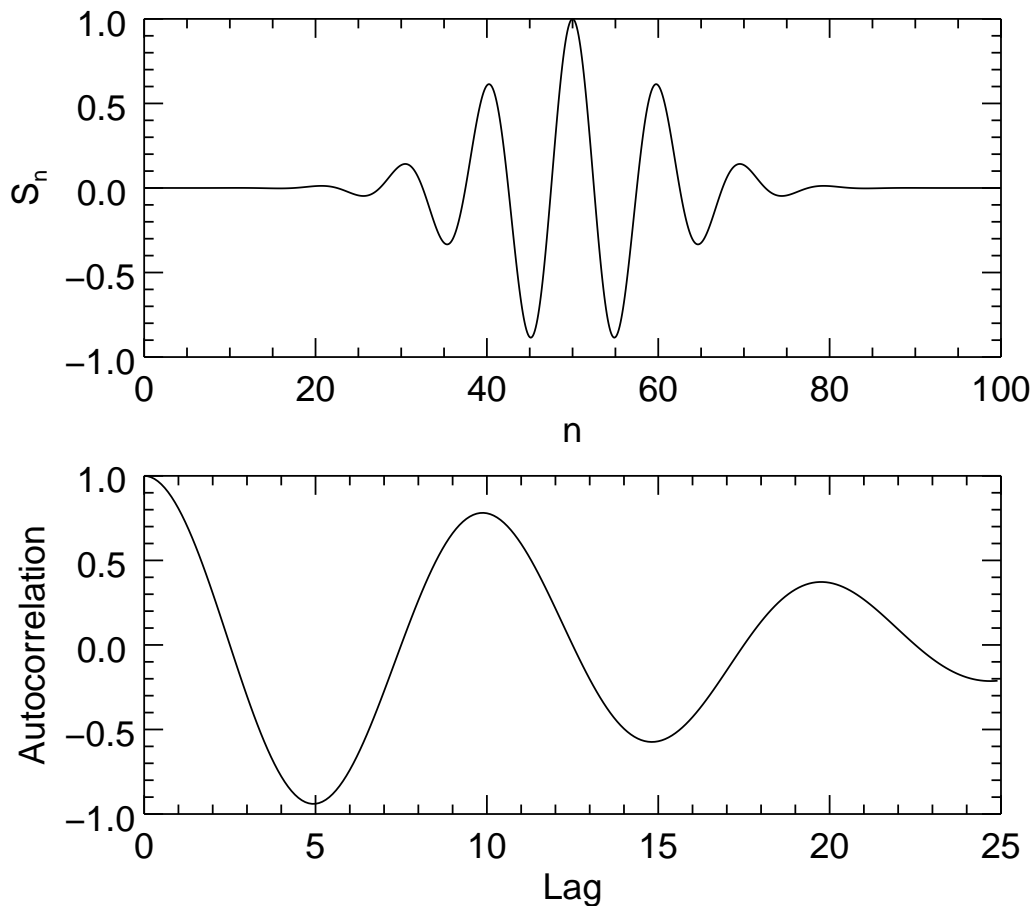
Figure 16. Top panel: An idealized wave packet in space or time with a wavelength or period of ten units. Bottom Panel: The autocorrelation function with lag in the same units as the abscissa on the top. Local maxima exist at wavelength or period multiples in the autocorrelation function with a perfect correlation at zero lag.

Fortunately, the Wiener-Khinchin theorem can be used. It asserts that the inverse Fourier transform of the cross-spectrum of a sequence with itself also yields the autocorrelation function. For a given sequence, S_n, that has a discrete Fourier transform, denoted $\mathcal{F}$, equal to $\mathcal{S}_k$

$$\mathcal{S}_k = \mathcal{F}(S_n) \qquad (2)$$

$$\mathcal{S}_k = \sum_{n=0}^{N-1} S_n e^{-i2\pi kn/N} \tag{3}$$

then the autocorrelation function, A_τ, will be

$$A_\tau = \sum_{k=0}^{N-1} \mathcal{S}_k \mathcal{S}_k^* e^{i2\pi kn/N} \tag{4}$$

where $\mathcal{S}^*$ denotes the complex conjugate of S. This can be written more compactly as

$$A_\tau = \mathcal{F}^{-1}[\mathcal{F}(S_n)\mathcal{F}^*(S_n)]. \tag{5}$$

Autocorrelation can be applied to both the tower and lidar data. When applied to the tower data, the first local maximum in the autocorrelation function signifies the wave period. Any of the variables that reveal periodicity during wave activities could be used. However, the temperature, relative humidity, and horizontal velocities are subject to larger trends. The vertical velocity, on the other hand, usually has no trend and has a very low mean. Therefore the vertical velocity was used to determine the wave period.

When applying this method to the REAL data canopy waves, the autocorrelation can be calculated using one- or two-dimensional fast Fourier transforms (FFT's) to calculate the autocorrelation in the following equation.

$$A_\tau = \mathcal{F}^{-1}[\mathcal{F}(\beta)\mathcal{F}^*(\beta)] \tag{6}$$

where β is the filtered backscatter field. $\mathcal{F}^{-1}$ and * denote the inverse FFT and the complex conjugate, respectively. The dimension of A_τ, τ, and β are all equal and typically equal to two.

Since the waves appear as periodic signals in β, A_τ will also be periodic. The function, A_τ, will peak at the origin where lag is equal to zero. From the origin it will have a decaying sine wave in the radial direction in the direction of propagation that decays further perpendicular to the direction of propagation. This leads to local maxima at a distance equal to the wavelength in the direction of propagation, giving the wavevector. For a series of images, a wavelength for every image can be calculated showing the evolution of wavelength over time.

Cross-Correlation

Cross-correlation can be used to compare two sequences as a function of lag. The correlation is calculated as a function of a shift of one of the images. Similar to the autocorrelation, the Wiener-Khinchin theorem can be applied to cross-correlation for two sequences $S_{1,n}$ and $S_{2,n}$ which is defined as

$$C_\tau = \frac{1}{N} \sum_{i=1}^{N-n} \frac{(S_{1,i+\tau} - \bar{S_{1,n}})(S_{2,i} - \bar{S_{2,n}})}{\sigma_{S_{1,n}} \sigma_{S_{2,n}}} \tag{7}$$

where $\sigma_{S_{1,n}}$ and $\sigma_{S_{2,n}}$ are the standard deviation of $S_{1,n}$ and $S_{2,n}$, respectively. This can take on a much simpler form

$$C_\tau = \mathcal{F}^{-1}[\mathcal{F}(S_{1,n})\mathcal{F}^*(S_{2,n})] \tag{8}$$

using Fourier transforms. This method was applied to two sequential frames of spatial two-dimensional lidar backscatter data. It takes the form

$$C_\tau = \mathcal{F}^{-1}[\mathcal{F}(\beta_1)\mathcal{F}^*(\beta_2)]. \tag{9}$$

These images are taken at known intervals, between 11 s and 30 s depending on the scan profile. The maximum in the cross-correlation function

indicates the displacement of the predominant features that the images share. Since the interval is known, the velocity can be calculated between every sequential pair of images. Since the waves are the most prominent feature of the images, this velocity is taken as the phase velocity.

CHAPTER IV

PRELIMINARY ANALYSIS

Lidar Data

Time-lapse animations of more than 1800 hours of high-pass median filtered REAL images from the entire CHATS data set were created. The animations of nearly horizontal scans were carefully examined for the presence of microscale wave packets. A wave packet is distinct from other flow features observed in the lidar images in that the linear bands (wavefronts) of enhanced backscatter intensity tend to be oriented perpendicular to the wind direction and the direction in which they propagate. Furthermore, they appear to have a high degree of spatial and temporal coherence compared to plumes and wind-parallel streaks that were occasionally observed during periods of turbulent flow.

The REAL has the unique ability to observe the spatial characteristics of microscale gravity waves. For the results presented herein, REAL data from a square kilometer area centered on the vertical tower was the main focus so that all quantities measured in situ could be studied as well. Time-lapse animations of this area were viewed by a human observer. For a wave packet to be included in this study, it must have passed over the position of the tower, located 1.6 km directly south of the lidar, and have a lifetime longer than one minute. Subjective judgments of the existence of the wave packets were based on the clear identification of crests and troughs and movement together as a group. Fifty-two wave episodes met the criteria.

Wavelength was measured subjectively for all the cases and ranged between 40 m and 100 m. For the 22 cases with a sufficiently short time between frames (≤17 s), propagation direction and phase speed were also determined from the displacement of a wave front in consecutive scans. Displacement was determined by tracing a wave crest in a series of images to see its progression in time. With the displacement, the phase speed can be calculated by dividing by the time between scan. The direction was determined by aligning a protractor perpendicularly to the wave crests. The propagation direction was in the direction of the mean flow (Figure 48) while the phase speed tended to be slower than the wind at the estimated scan height of 18 m.

In-Situ Data

Once the wave episodes were identified in the lidar data, the corresponding temporal data from the tower were studied to confirm the hypothesis that the waves have a dynamical cause and are not an artifact of the lidar. Time series of vertical velocity during wave episode do in fact show wave activity. Oscillations in the vertical velocity (Figure 17) confirm the hypothesis that the perturbations in the backscatter are a dynamical phenomenon and related to vertical displacements of air. These oscillations are vertically coherent throughout the height of the tower suggesting the waves are evanescent and not vertically propagating. Through subjective inspection, periods were estimated to range between 20 s and 120 s. Autocorrelation of these temporal data can be used to determine the period objectively on a case by case basis.

After the vertical velocity was analyzed, the temperature was examined (Figure 18). Waves are also present in these data, providing strong evidence that the waves are gravity waves even though there are no direct measurements of
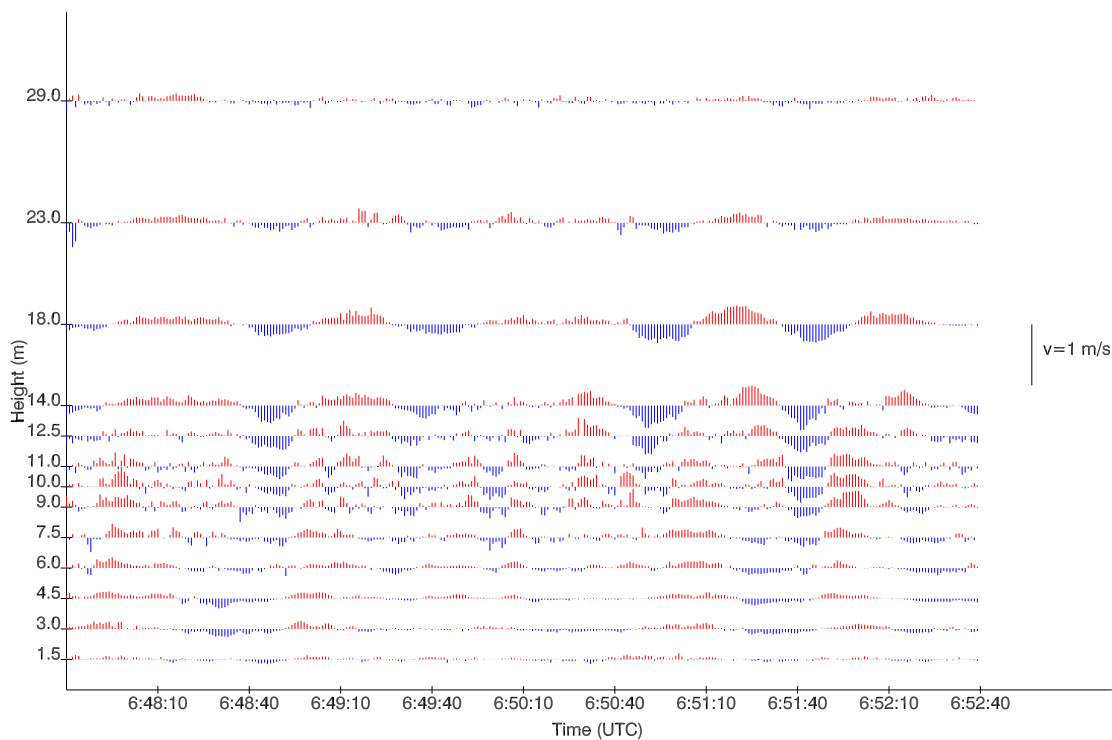
Figure 17. (Color required.) Time series for the duration of a wave episode that occurred at 06:45:10 until 06:52:29 UTC 30 March, 2007. Data from each height is plotted simultaneously with the length of each bar indicating the magnitude of the vertical velocity. Upward motions are in red and downward are in blue. Oscillations are vertically coherent from inside the canopy (<10 m) to the top of the tower (29 m).

density. Based on the first subjective inspections, the periods of the oscillations in the temperature are approximately the same as the periods in vertical velocity for a given wave episode. A 90° phase difference exists between the vertical velocity oscillations and the temperature oscillations. This supports that these are waves and not a turbulent coherent structure. Turbulence would result in a random phase shift, while waves show this 90° relation (*Lee et al.*, 1996).

In-situ measurements of horizontal wind components from the tower also reveal oscillations (Figure 19). The oscillations occur with the same frequency and
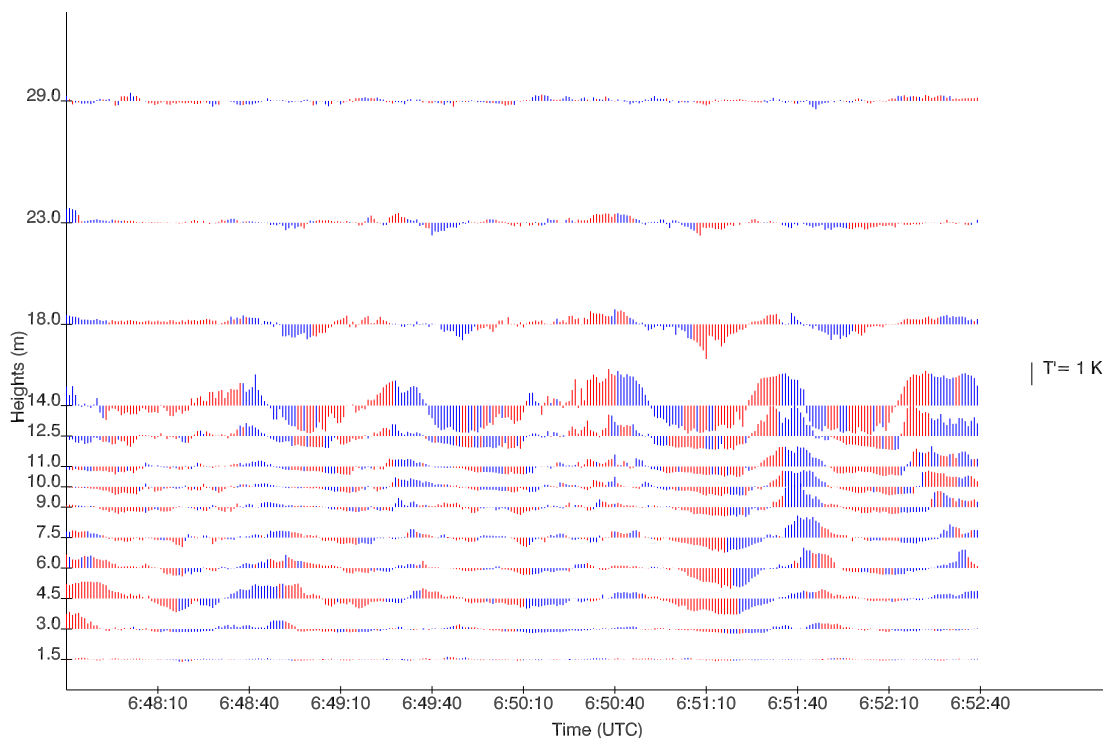
Figure 18. (Color required.) Simultaneous time series of temperature for all 13 heights for the same wave episode as shown in Figure 17. To compare the two, positive vertical velocities are in red and negative in blue. Oscillations are present in temperature data with the same period as the vertical velocity.

period as the vertical velocity, however, they occur with a 90° phase difference. This results in a low vertical flux of horizontal momentum. In other words, the waves are not transporting horizontal momentum vertically. Symmetrically, there is low vertical-momentum flux horizontally, but this is less consequential since there is very little vertical momentum compared to horizontal momentum, generally (*Martin*, 2006). The velocities also exhibit both speed and directional shear as a function of height. The speed shear of the environment during waves supports the notion that the waves are generated by wind shear. Temperature profiles during these episodes all show very stable conditions (Figure 20). This observation is

consistent the notion that wave activity occurs in stable atmospheres and that strong stability results in high-frequency waves.
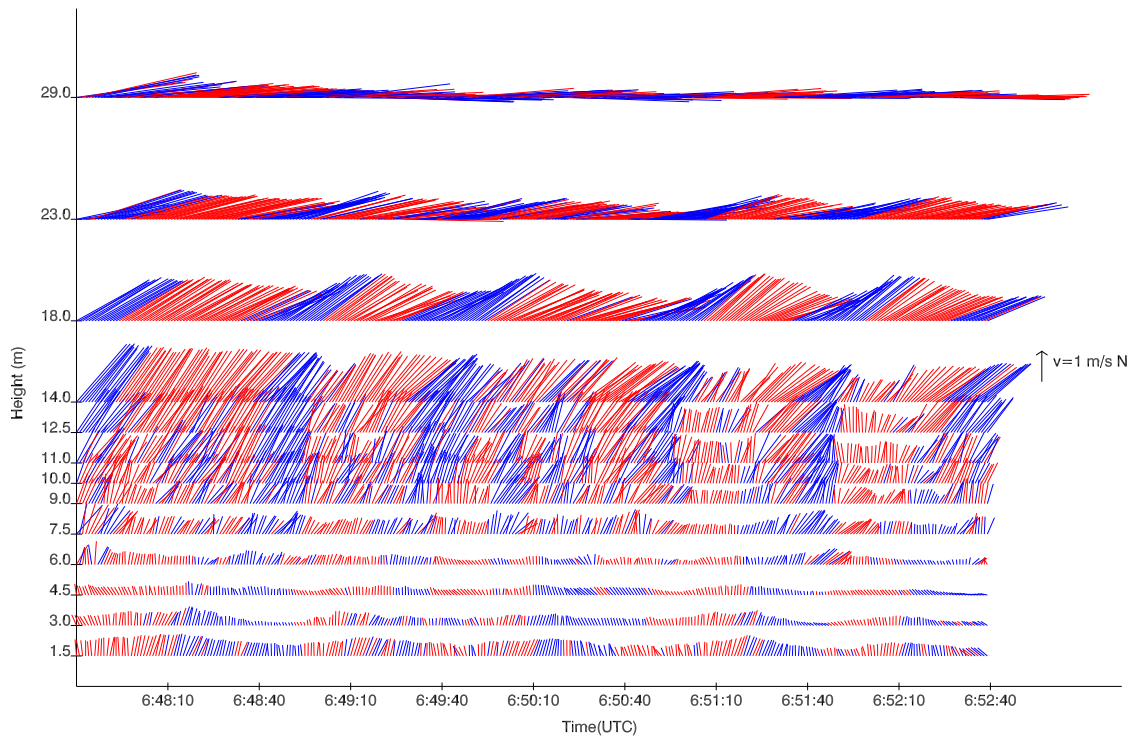
Figure 19. (Color required.) The horizontal velocities plotted in the same fashion as shown in Figures 17 and 18. However, here the wind vectors are plotted to indicate the wind speed and direction. The horizontal velocities reveal oscillations, speed shear and directional shear over the altitude span of the 13 sensors.
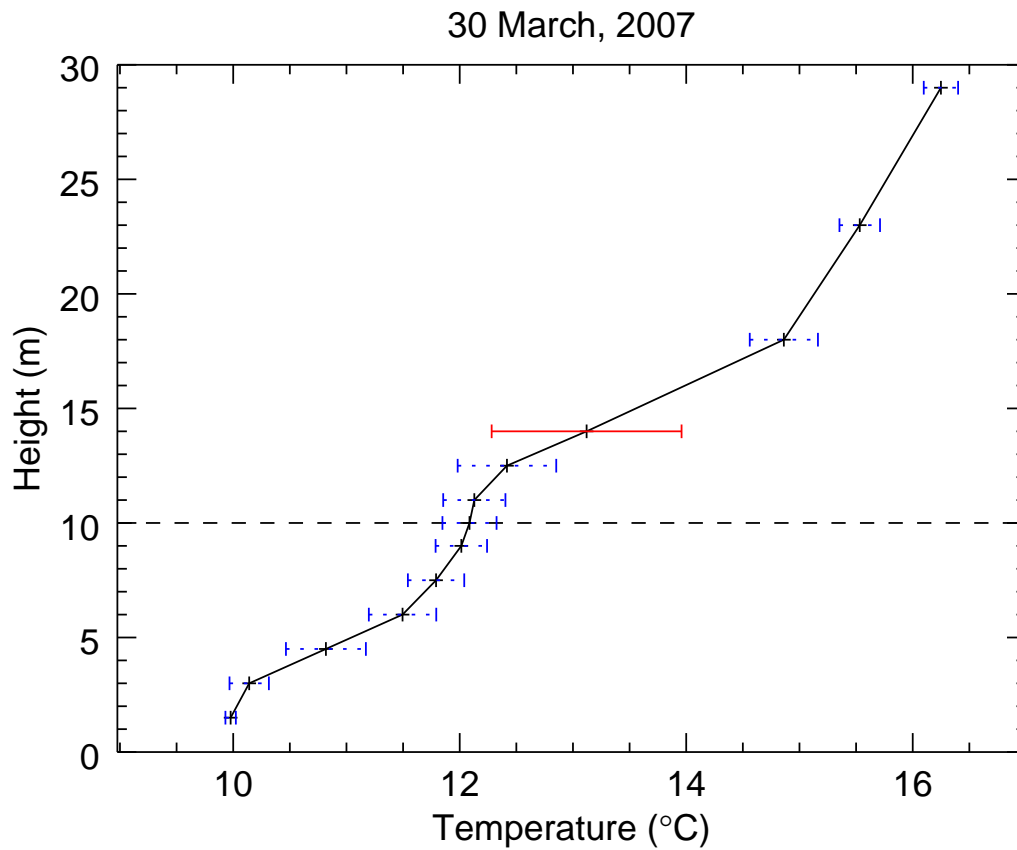
Figure 20. (Color required.) Mean temperature profile for the 30 March wave episode. The average temperature at each height on the tower is plotted and the horizontal bars show the standard deviation during the wave episode. The solid error bar indicates the largest variability of the 13 measurements.

CHAPTER V

CASE STUDIES

In the CHATS data, 52 wave episodes were identified in the images produced by the lidar. These varied in duration, spatial and temporal coherence, amplitude of the quantities measured in situ, the time between scans of the lidar, and the angle that each scan subtended. Based on these criteria, three case studies were chosen for further analysis.

Case 1: 14 May 2007

This case has the longest duration at 1 hour 11 minutes (01:00:34 to 02:11:11 AM PDT). During this time the lidar was programmed to alternate between RHI (vertical) and PPI (horizontal) scans and therefore the temporal resolution of the horizontal image sequence was lower relative to other cases. The waves do not appear in the RHI scans, likely due to the small number of laser pulses projected in the small range of altitudes where the waves existed. PPI scans were repeated every 30.3 s. Each scan covered 60° of azimuth at an elevation of 0.20°. Figure 11 shows a 1 km by 1 km subset of a scan centered on the ISFF tower. In this image, it is possible to identify approximately 15 parallel bands of backscatter. The corresponding time-lapse animation shows the bands traveling perpendicular to their orientation and toward the NW. The waves exist up to the edge of the forest canopy at about 1.4 km range from the lidar but do not appear to be present in the areas absent of trees. Also of note is the very bright

backscatter streaks starting at about 1.5 km range on the left side of the image. This was the result of hard target reflections from a cluster of taller trees near a farm compound. In some scans, laser pulses struck the tower or foliage from the canopy top resulting in intermittent hard-target reflections.

During this episode, the atmosphere was statically stable with an average lapse rate of -0.27 K m^{-1} and a mean temperature of 15.4°C at 18 m (the estimated height of the lidar scan at the range of the tower). The lapse rate was based on data from the bottom temperature sensor at 1.5 m and the top sensor at 29 m (Figure 21).

Oscillations are present in the in-situ velocity data (Figure 22). From the sonic anemometer data, the waves have a vertical velocity (w) amplitude on the order of 0.5 m s^{-1} and a period of approximately 40 s based on subjective visual inspection. These oscillations appear to have a constant phase with height and a decreasing amplitude with increasing distance from the oscillations at 18 m AGL. This suggest the waves are evanescent. Temperature data also exhibit oscillations with the same period and an amplitude of about 3° C at 18 m (Figure 23). These two variables (w and T) oscillated with a 90° phase difference with respect to one another resulting in nearly zero thermal flux (Figure 24). This relationship also holds between vertical and horizontal wind speeds implying low vertical flux of horizontal momentum. There is no phase shift between vertical velocity relative humidity oscillations leading to a net flux of moisture.

Wavelength was determined subjectively from the PPI scans. For the scan with the most pronounced bands of backscatter, a wavelength was estimated to be about 70 m. By tracing wavefronts from each scan, and noting their displacement from frame to frame, the phase speed of the waves was determined to be about 1.7 m s^{-1}. These numbers are good first estimates, but both are prone to
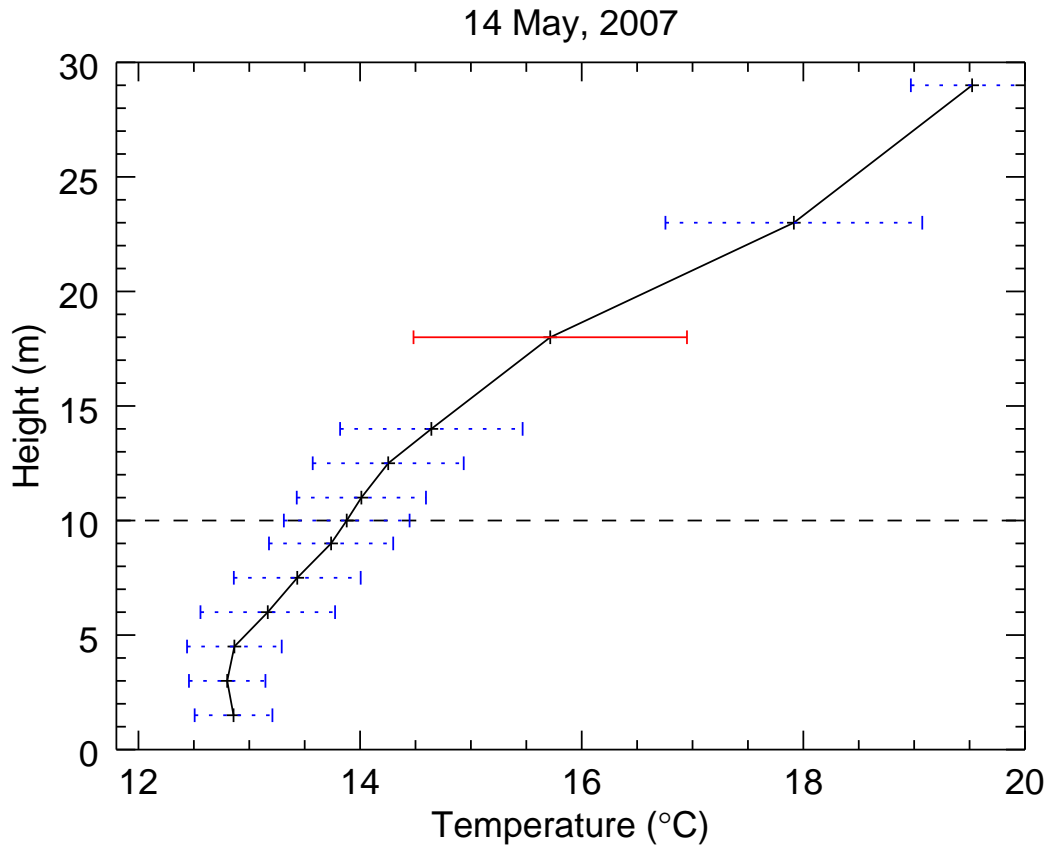
14 May, 2007

Figure 21. (Color required.) Mean temperature profile for the 14 May 2007. The dashed line indicates canopy height. The horizontal error-bars indicate the standard deviation with the largest indicated in red.

biases. For instance, the values depend on which wave crest an observer chooses to follow and how one interprets the precise location of the crest. To avoid these ambiguities, statistical correlation methods were used to objectively determine the quantities, and therefore eliminate the variability of errors due to human interpretation.

Autocorrelation functions (ACFs) reveal similarities in sequences as a function of a shift, or lag, with respect to the same data. The global maximum of an ACF is always at the origin. For turbulent data, an ACF can reveal the time
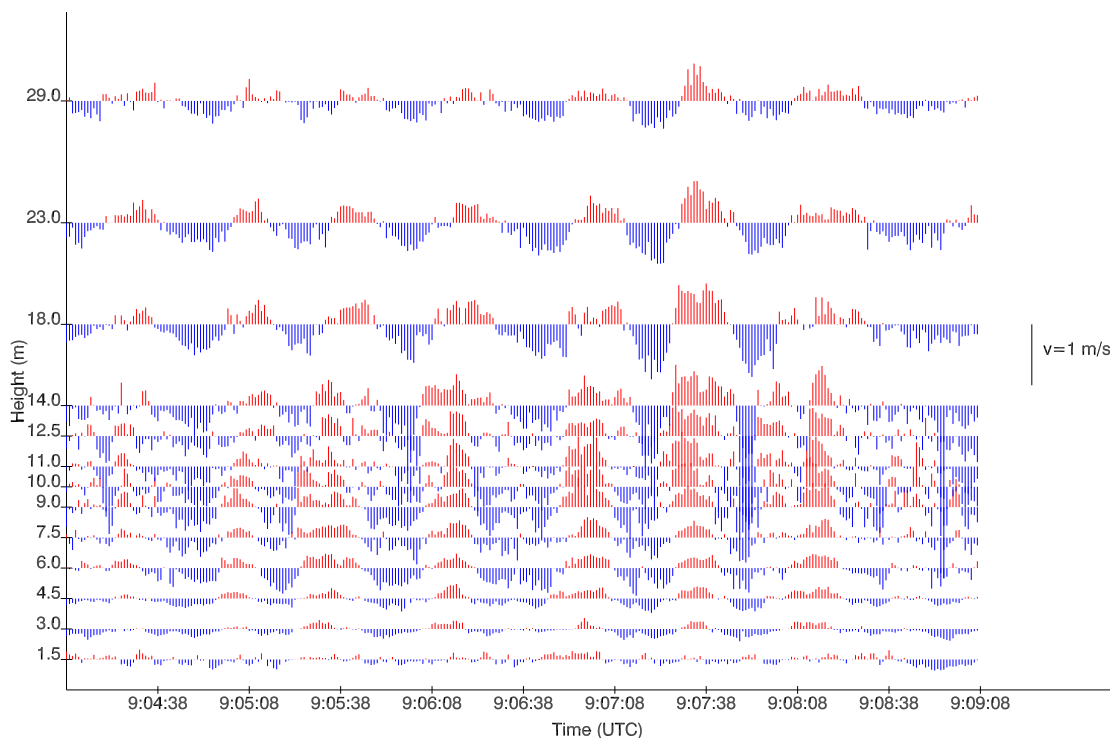
Figure 22. (Color required.) Vertical velocity from the sonic anemometers at all 13 heights plotted versus time for 14 May 2007 case. Red indicates upward motion and blue indicates downward motion.

scale or length scale. For periodic data, the first local maximum indicates the wavelength for spatial data or the period for temporal data. Using this method with the spatial lidar data, the wavelengths range from 54 m to 105 m over the course of this episode (Figure 25). At the time of the subjective estimate of 70 m, the ACF indicates a wavelength of 78 m. The wavelength generally decreases over the course of this episode. The autocorrelation of the temporal data leads to a period of 42 s, agreeing with the subjective estimate.

The mean wind during this period was from the south at altitudes below the canopy and increased in speed and veered from 10 m to 29 m above ground level (see Figures 27 and 28). Oscillations are present in the horizontal velocities as
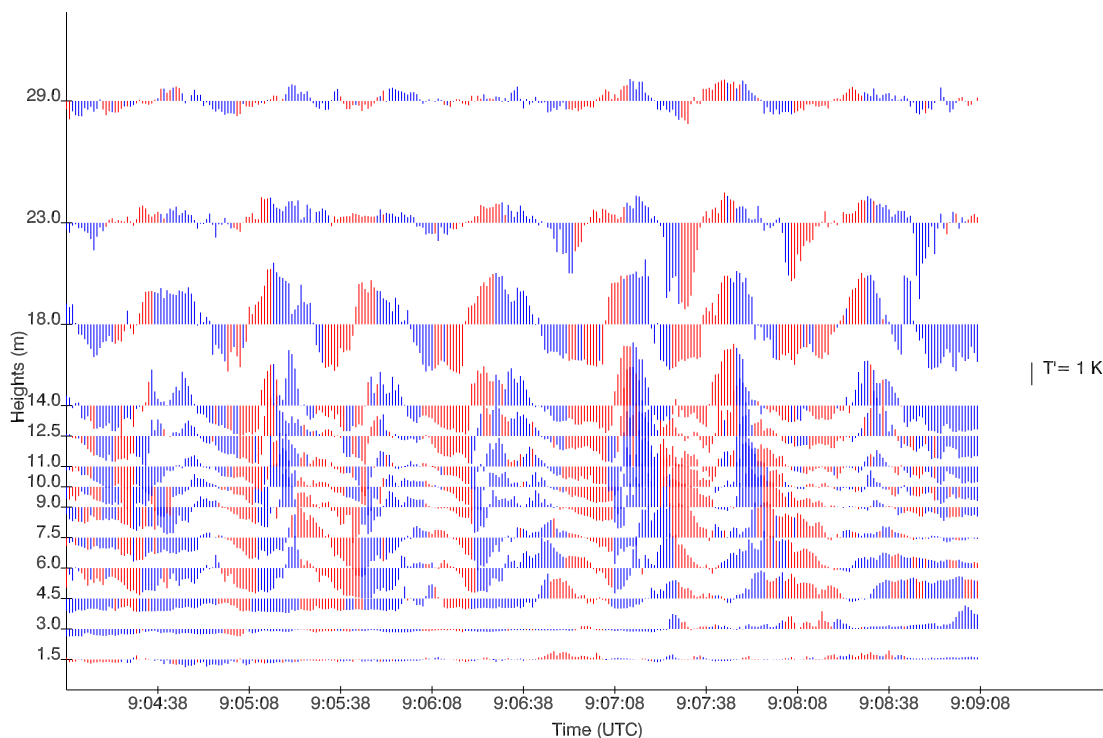
Figure 23. (Color required.) Temperature perturbations from the sonic anemometers at all 13 heights plotted versus time for 14 May 2007 case. Red indicates upward motion and blue indicates downward motion.

well in both speed and direction (Figure 29). A periodic change in both magnitude and direction is present at the same frequency as the oscillations in the vertical velocity and temperature. The standard deviation of vertical velocity was calculated at each height. The fluctuations due to wave motion are assumed to be the greatest contributor to the standard deviation, so it follows that the height with the highest standard deviation is the height with the greatest amplitude. In this case, that height is 18 m. This is suspected to have been the height closest to the point of generation of the waves. Since this is the height that is closest to the scan plane, it may explain why this case has such large crests of backscatter compared to some of the other cases. Theoretically, the point of generation should
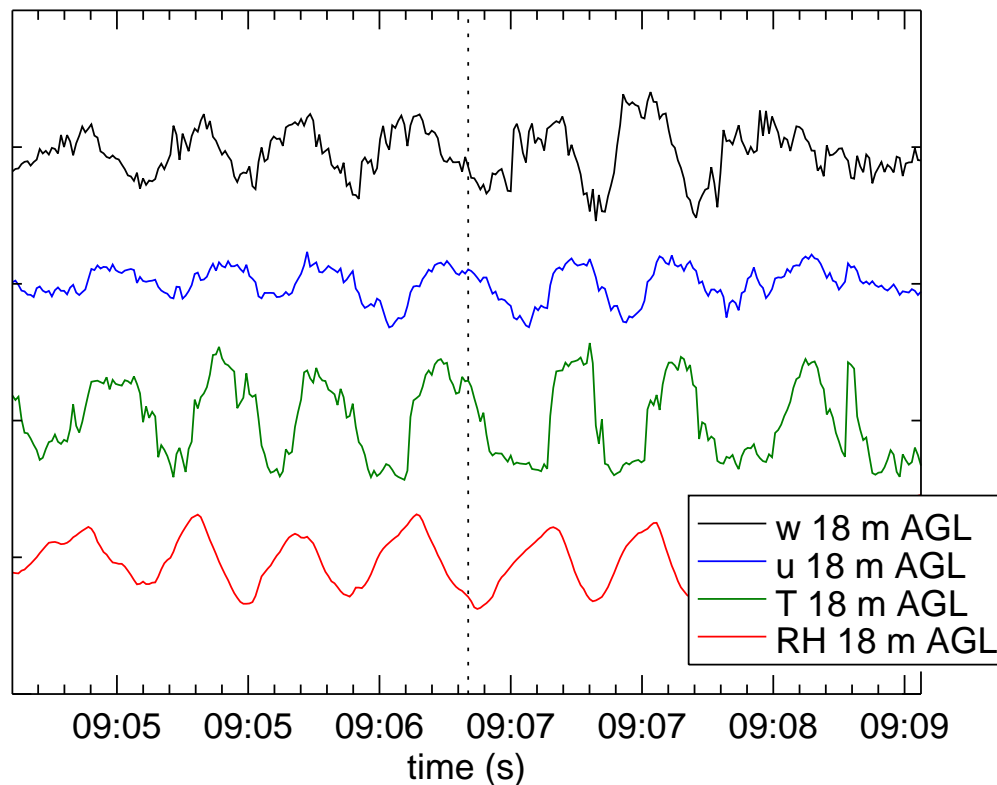
Figure 24. (Color required.) From top to bottom, time series for vertical velocity, temperature perturbations, horizontal velocity perturbations, and relative humidity perturbations to show their relative phases. The vertical velocity is in phase with relative humidity and 90° out of phase with both vertical velocity and temperature.

be at the inflection point (*Nappo*, 2012). This height appears to be above the inflection point, which appears to be closer to 14 m. Both of these heights have similar standard deviations in vertical velocity so there is no clear maximum, but it most likely lies between those two heights. Another explanation is that the amplitude of the waves decreases as the distance to the ground decreases due to the fact that the ground itself is a barrier to vertical air motion, resulting in a maximum amplitude at or above the inflection point.
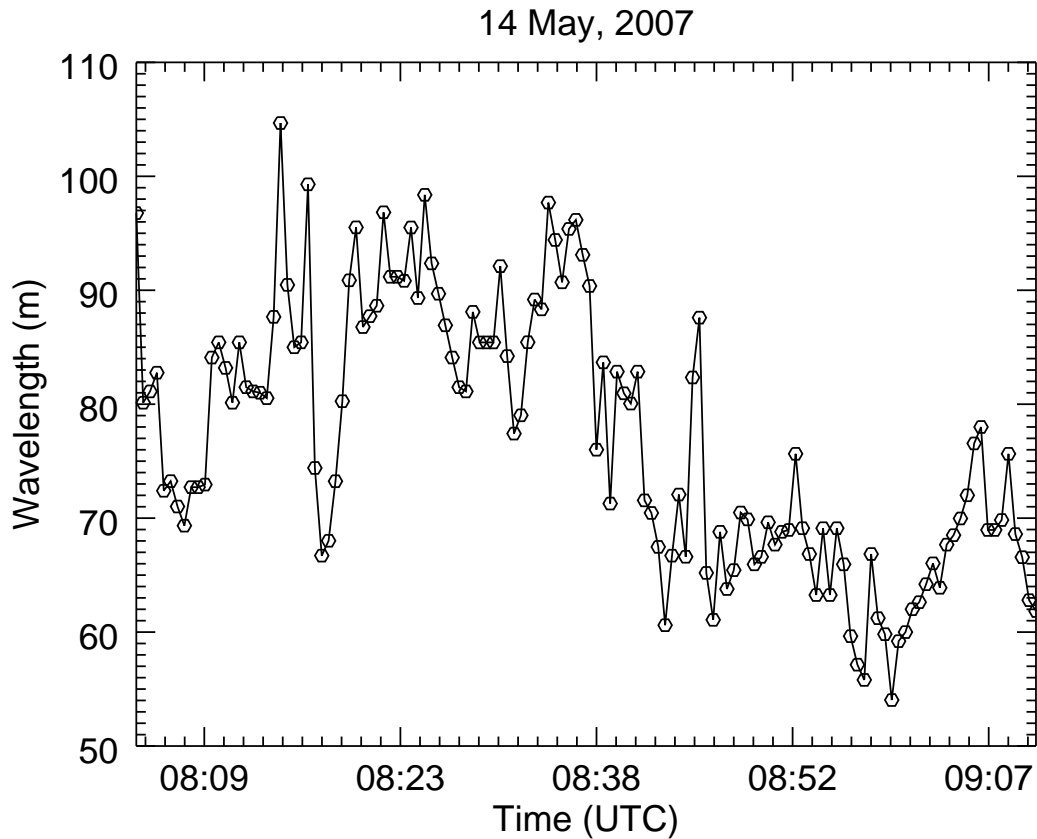
Figure 25. Time series of the wavelength that results from the application of the autocorrelation algorithm for every frame of this episode.

The cross-correlation function between sequential frames can be used to objectively determine the displacement of the prominent features that the frames share (*Hamada*, 2014). In this case, the prominent features are the 15 parallel bands that displace an average distance of 60.0 m toward 18° N of E. Dividing the displacement by the time between scans, 30.3 s, gives the phase speed of 2.0 m s^{-1}. With an average wavelength of 77 m and average phase speed of 2.0 m s^{-1}, the average period is 39 s, which is very close to the subjective estimate of 40 s and the temporal autocorrelation calculation of 42 s.

14 May, 2007
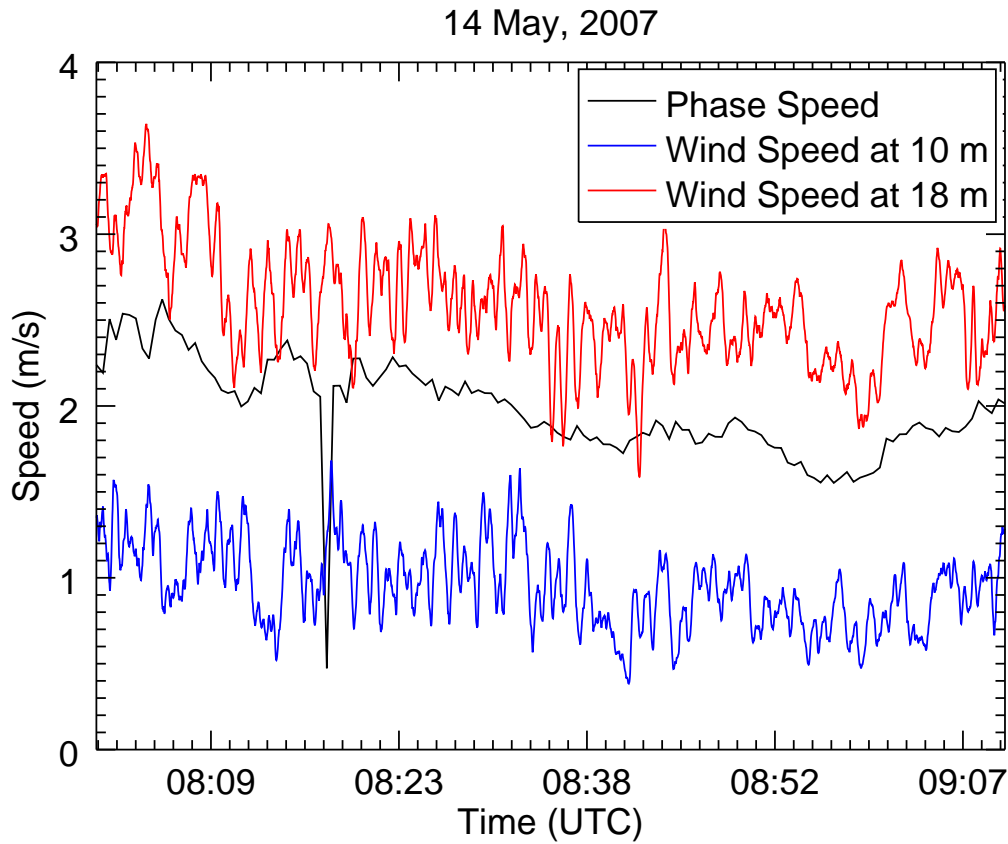
Figure 26. (Color required.) Time series of the phase speed as calculated by cross-correlation for every pair of frames on 14 May.

The relative humidity (RH) also exhibited oscillations at the frequency of the other variables (Figure 30). It is in phase with vertical velocity which would lead to a net positive flux of humidity upward. The RH trends down for all of the sensors below 18 m which also suggests positive vertical humidity flux. These oscillations and trends are not present in all of the cases however.
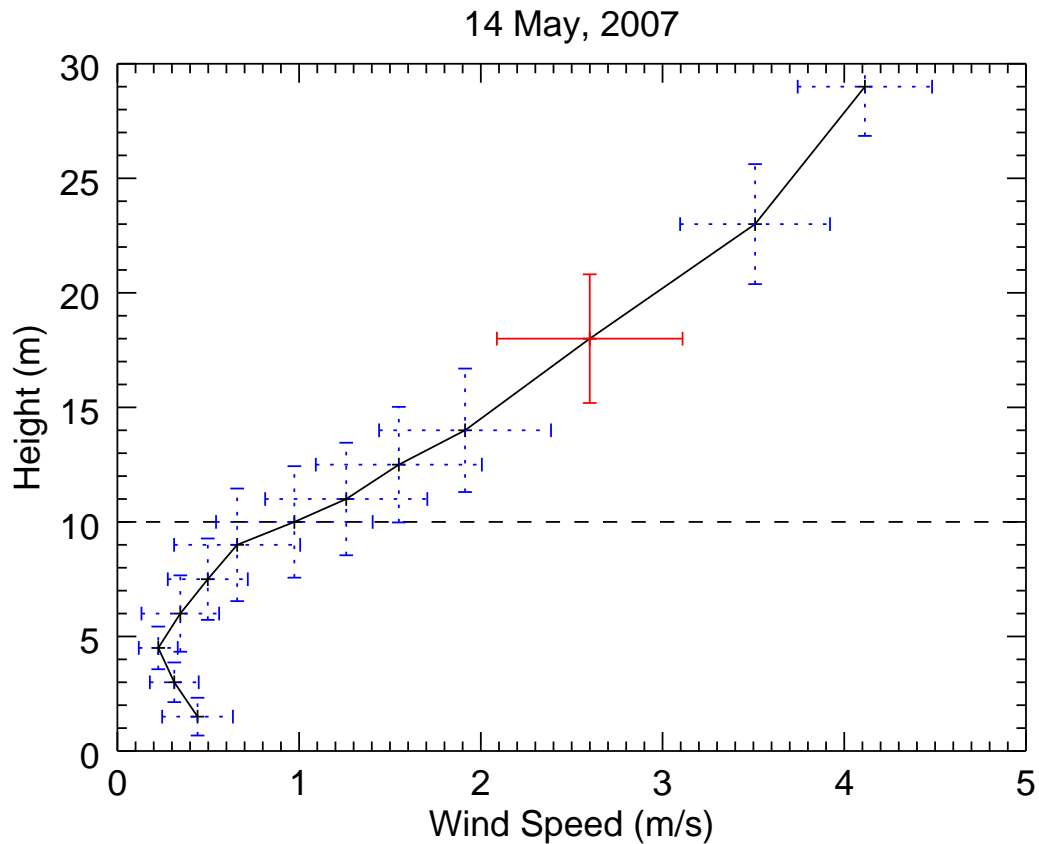
Figure 27. (Color required.) Mean wind speed profile for the 14 May wave episode. Horizontal and vertical bars at each point indicate the standard deviation for horizontal and vertical winds, respectively. The height of the maximum standard deviation of the vertical velocity is indicated in red. The horizontal dashed line indicates canopy height. Note: The standard deviation bars are not to scale. Since the magnitudes of the vertical velocities are so much lower, they are scaled up by a factor of ten compared to the horizontal velocities, which are to scale with the x-axis.
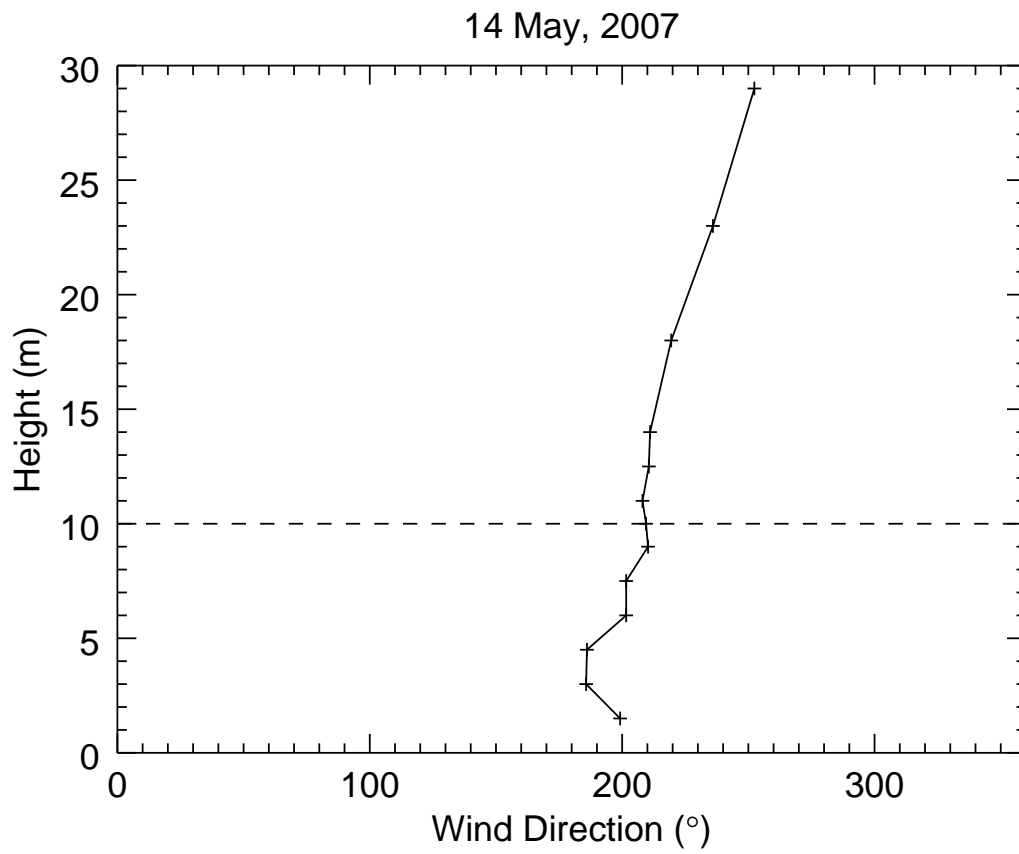
Figure 28. Mean wind direction profile for the wave episode on 14 May.
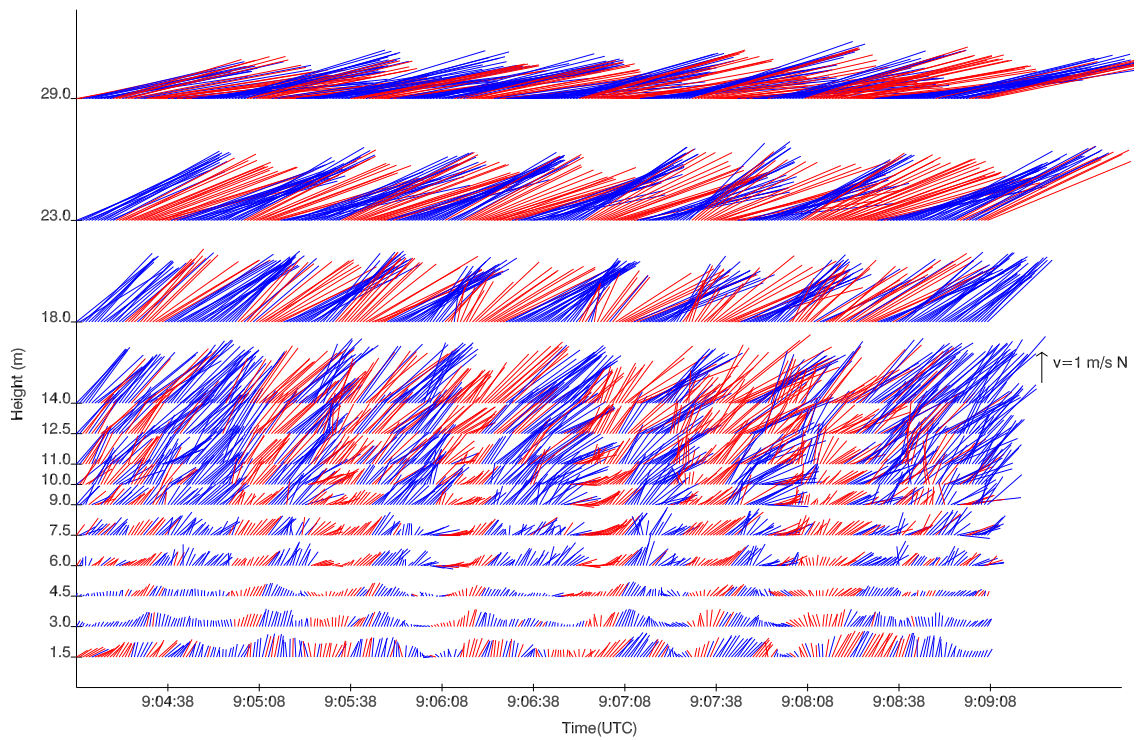
Figure 29. (Color required.) Horizontal wind vectors from the sonic anemometers at all 13 heights plotted versus time for 14 May 2007 case. Red indicates upward motion and blue indicates downward motion. Positive u-component is up, and positive v-component is right.
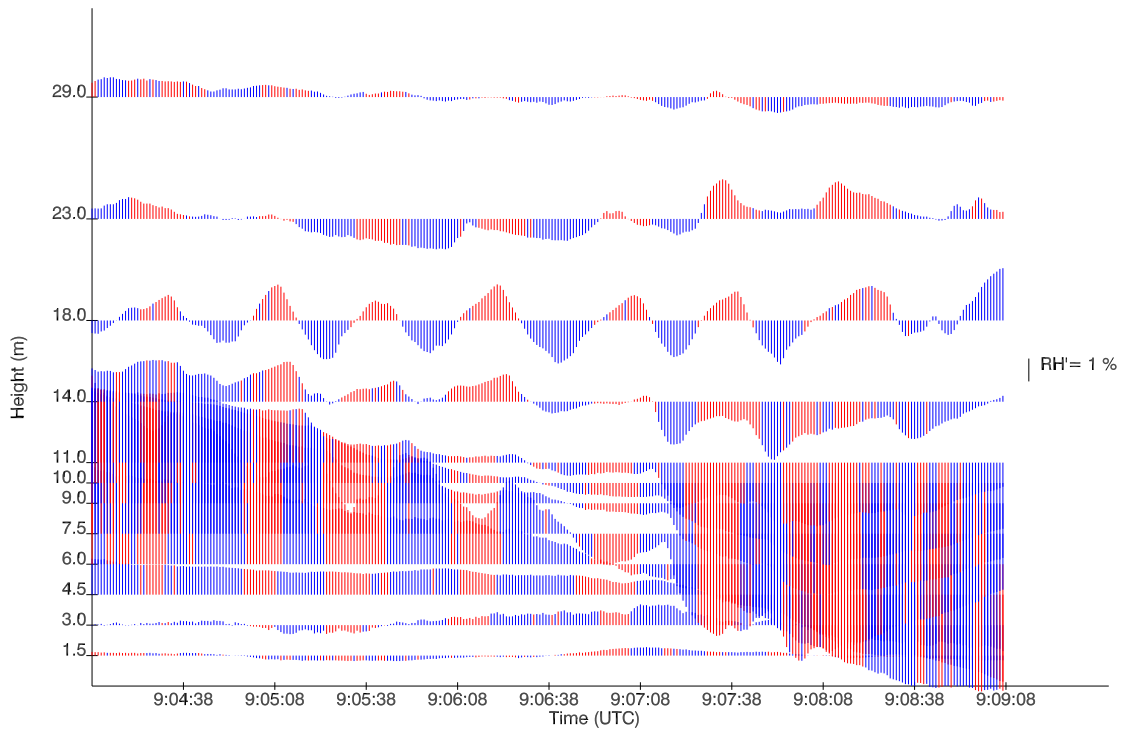
Figure 30. (Color required.) Relative humidity time series for 14 May case for all 13 heights over five minutes in which the episode had very pronounced waves.

Case 2: 27 April 2007

This case occurred between 00:51:15 to 01:07:53 PDT (15 min 38 s) and is shown in Figure 31. The same scanning routine was used as in the 14 May case with alternating PPI's and RHI's, which resulted in a PPI scan every 30.3 s and an area covering 60° of azimuth. This is another case with very pronounced waves in the backscatter data from the lidar. There are approximately 16 linear bands of high backscatter in the 1 km^2 area of study.

The vertical velocities from the sonic anemometers (Figure 32) show coherent waves, but may have a very slight phase shift with height that increases with altitude suggesting this case may not be entirely evanescent, but it may have some small vertical component to the direction of propagation. The waves appear to have a period of about 40 s. The autocorrelation method strongly agrees which suggests a period of 40. s.

The average wind velocity at 18 m was 2.37 m s^{-1} 249.72°. The horizontal velocities are also periodic. This periodicity is again 90° out of phase with the vertical velocity, as shown by the relative phase of the red and blue, to the magnitude and direction in Figure 33. There is also speed shear with an average value of 0.068 s^{-1} as well as directional shear. The wind comes from almost due south at the bottom and from ESE at the top of the tower. Both this case and the 14 May case are veering in height through the height of the tower.

The average temperature at 18 m during this episode was 15.8°C with a gradient from 10 m to 29 m averaging 0.27 K m^{-1}. The waves are present in the temperature data with a decreasing trend in temperature as the episode progresses. Temperature perturbations are again 90° out of phase with vertical-velocity perturbations.

Autocorrelation of the lidar data results in an average wavelength of 62.9 m, agreeing within error to the subjective estimate of 70 m (Figure 35). This case is fairly monochromatic for the first several minutes, varying from about 55 m to 65 m until approximately 01:00 PDT when the wavelength increases to over 80 m. The increase is unlikely to be a random spike because the wavelength gradually grows to over 80 m and then gradually decreases again over about 3 min. The cross-correlation for this case suggests a phase speed of 1.42 m s^{-1} (Figure 36). The wave phase speed remains between the wind speed at canopy height and the wind speed at the lidar scan plane for the duration of the episode. When the period is calculated by combining both of the methods using lidar data, a period of 44.3 s was determined, agreeing with both of the previous periods.

The night of 27 April had five wave episodes, the most of any night during CHATS, suggesting that the environmental conditions were very supportive of wave activity that night. This episode was the second of the five and the most spatially coherent based on subjective inspection.

From the time lapse lidar animation of this episode, there are patches of very low backscatter that remain at the north end of the orchard. This potentially could move the local max of the autocorrelation and global max of cross-correlation toward the center because it appears as a stationary feature. This could explain why both objective methods were lower than their corresponding subjective estimates. If the wavelength and phase speed are proportionally low with respect to each other, the method of determining the period from lidar data would still be accurate which it seems to be here.
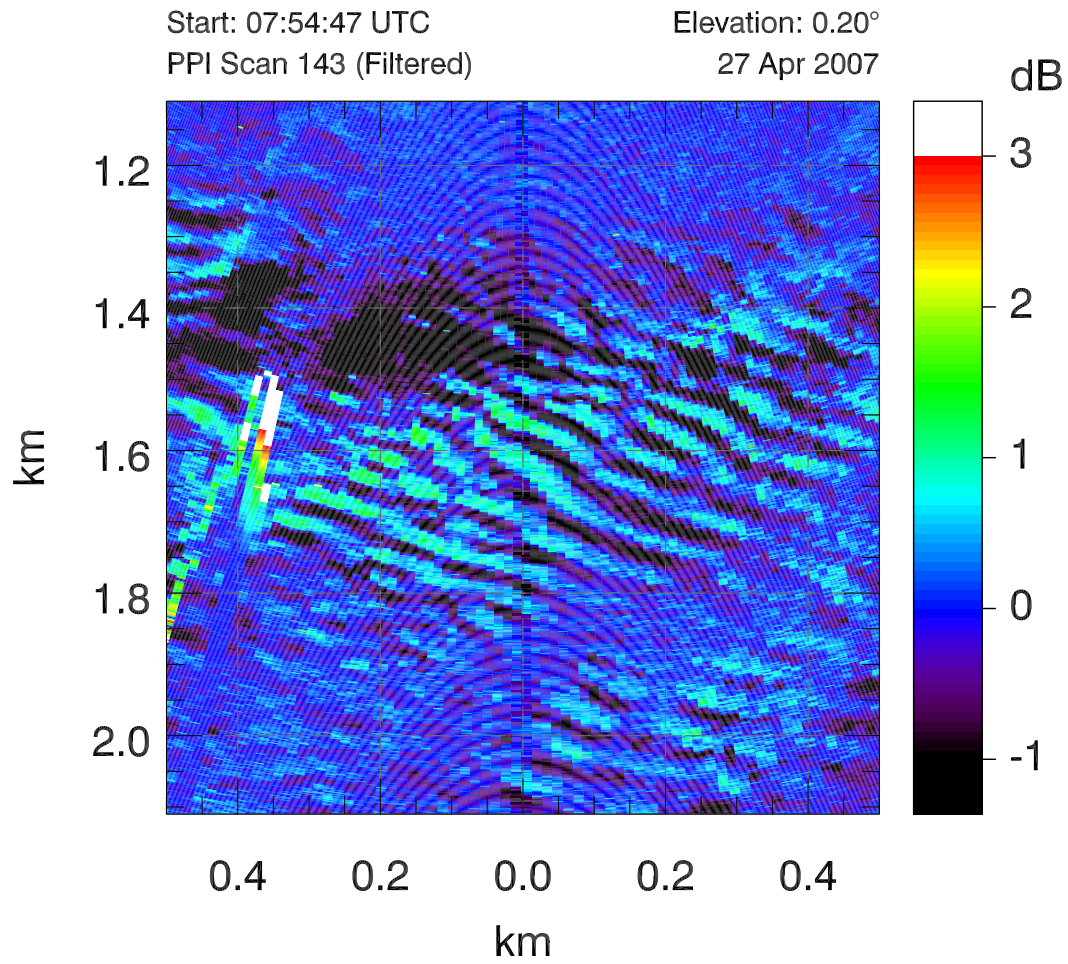
Figure 31. (Color required.) Lidar image for the wave episode at 07:54 UTC (00:54:15 PDT) on 27 April 2007.
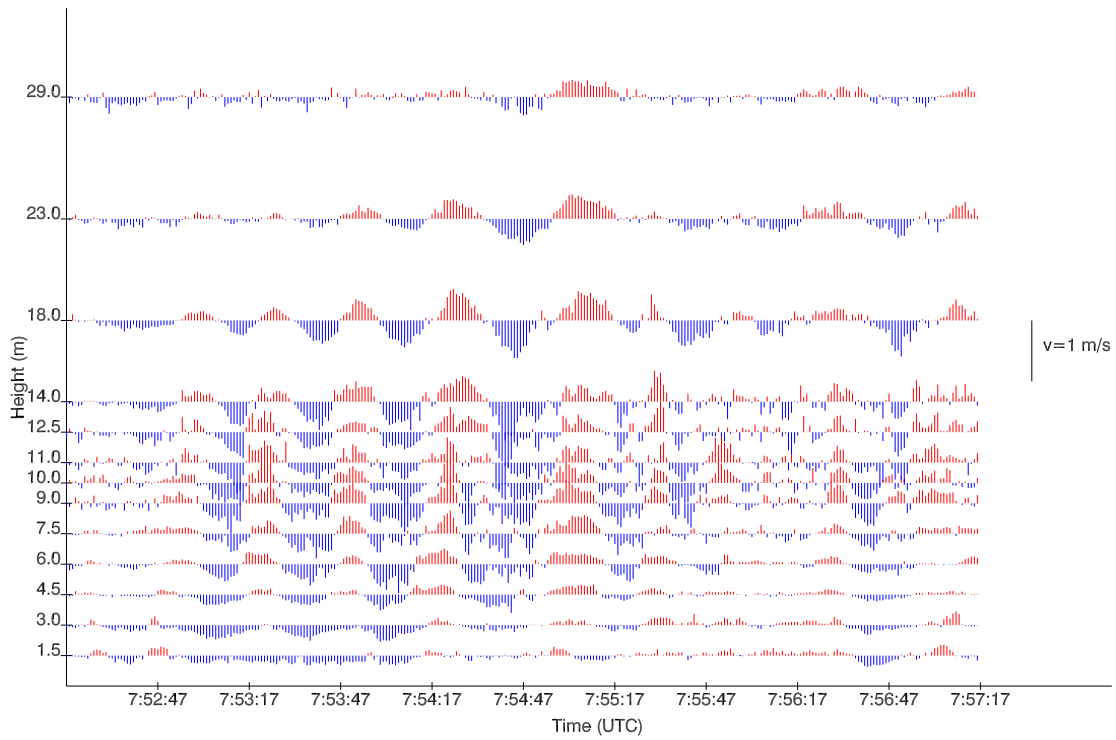
Figure 32. (Color required.) Vertical velocity on 27 April for all 13 heights plotted versus time. Red indicates upward motion and blue indicates downward motion.
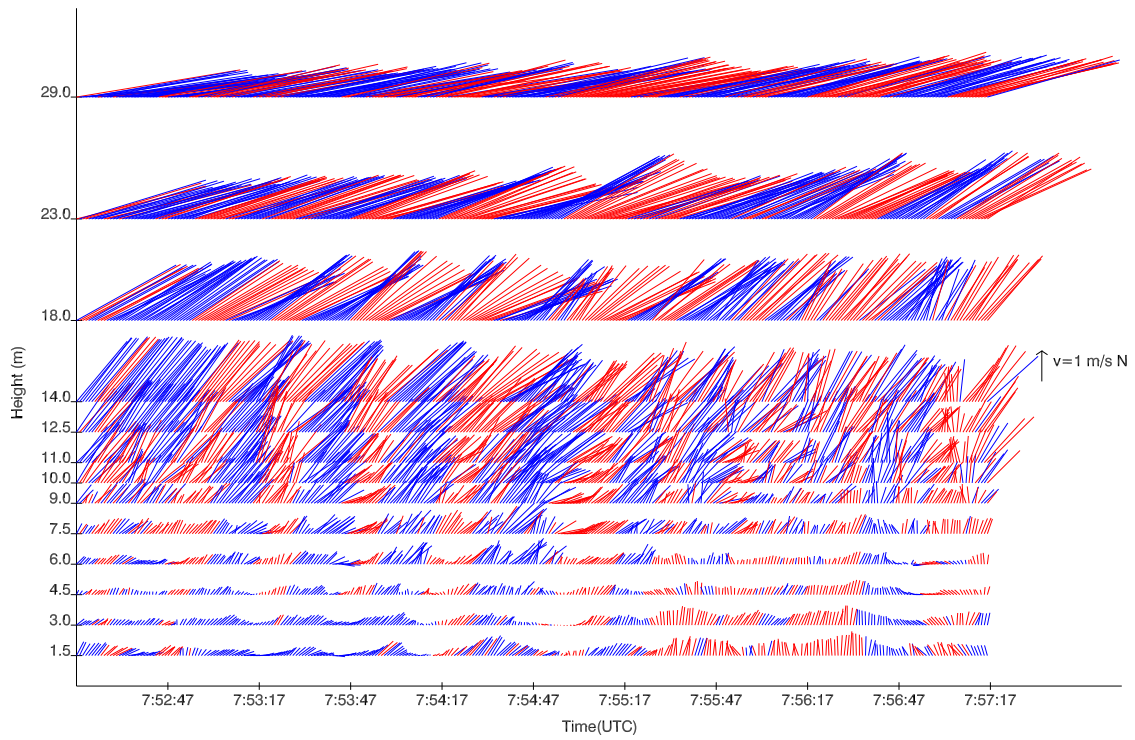
Figure 33. (Color required.) Horizontal velocity on 27 April for all 13 heights plotted versus time. Red indicates upward motion and blue indicates downward motion.
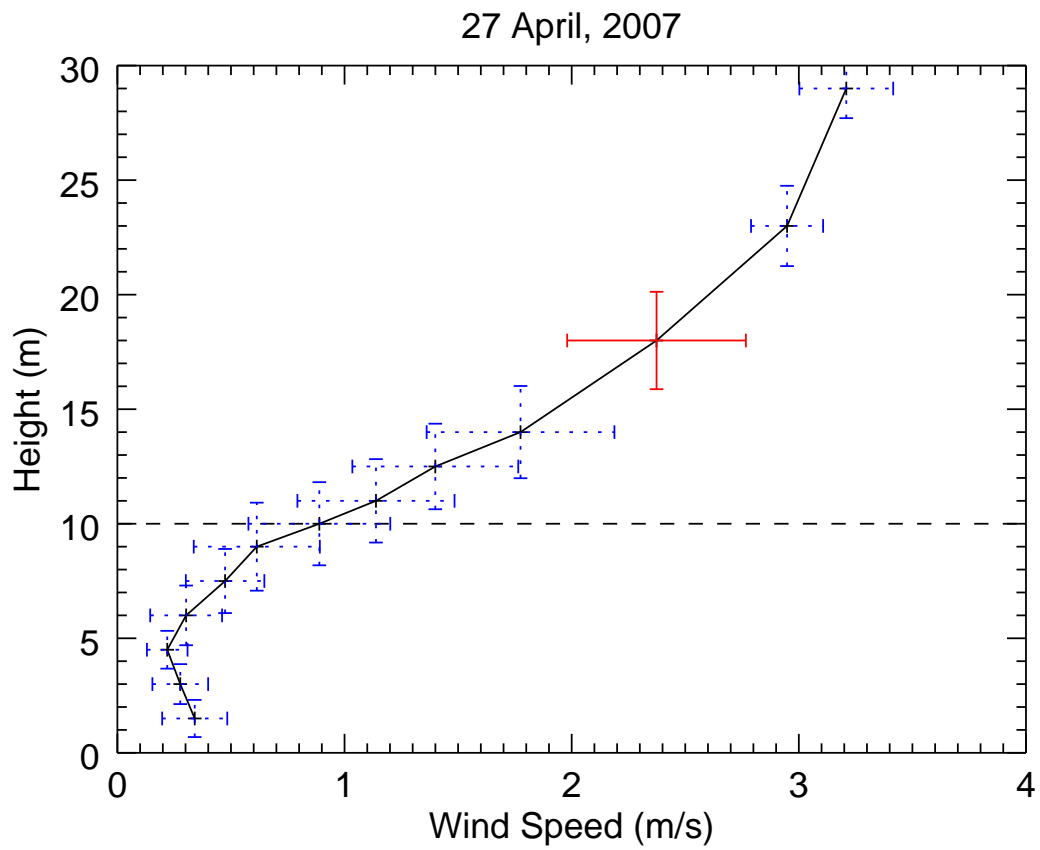
Figure 34. (Color required.) Mean wind speed profile for the 27 April wave episode.
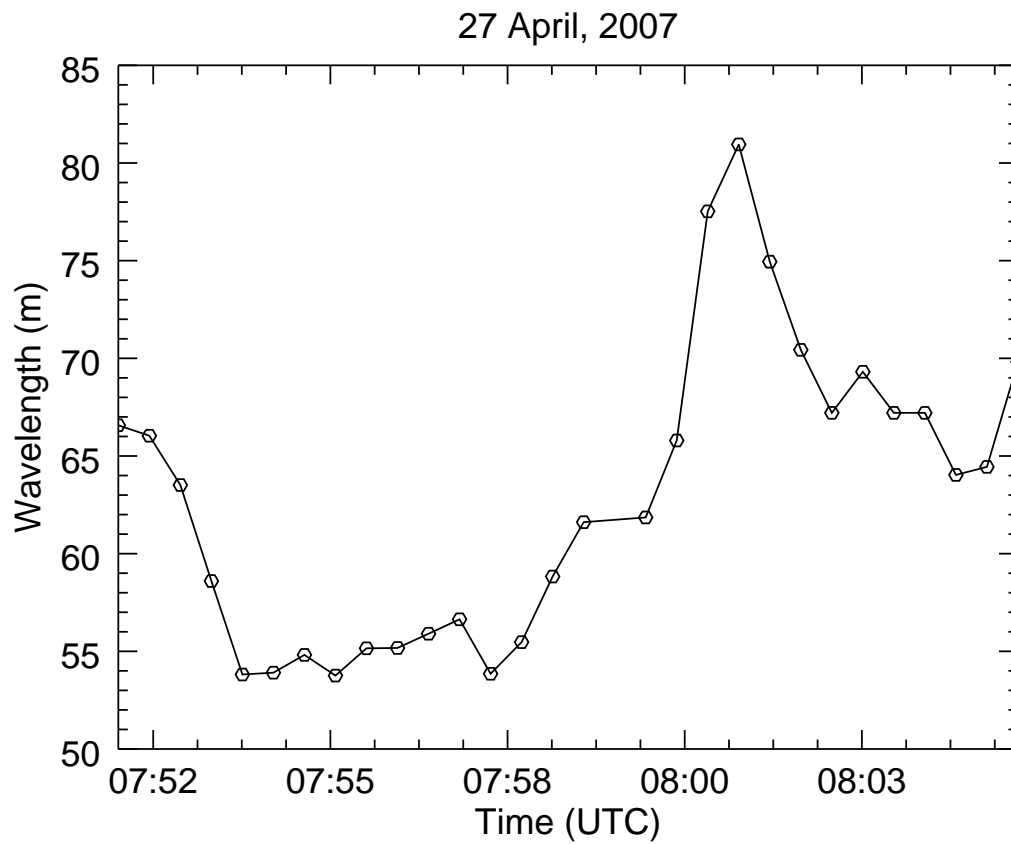
Figure 35. Time series of the wavelength that results from the application of autocorrelation to every frame for the 27 April episode.
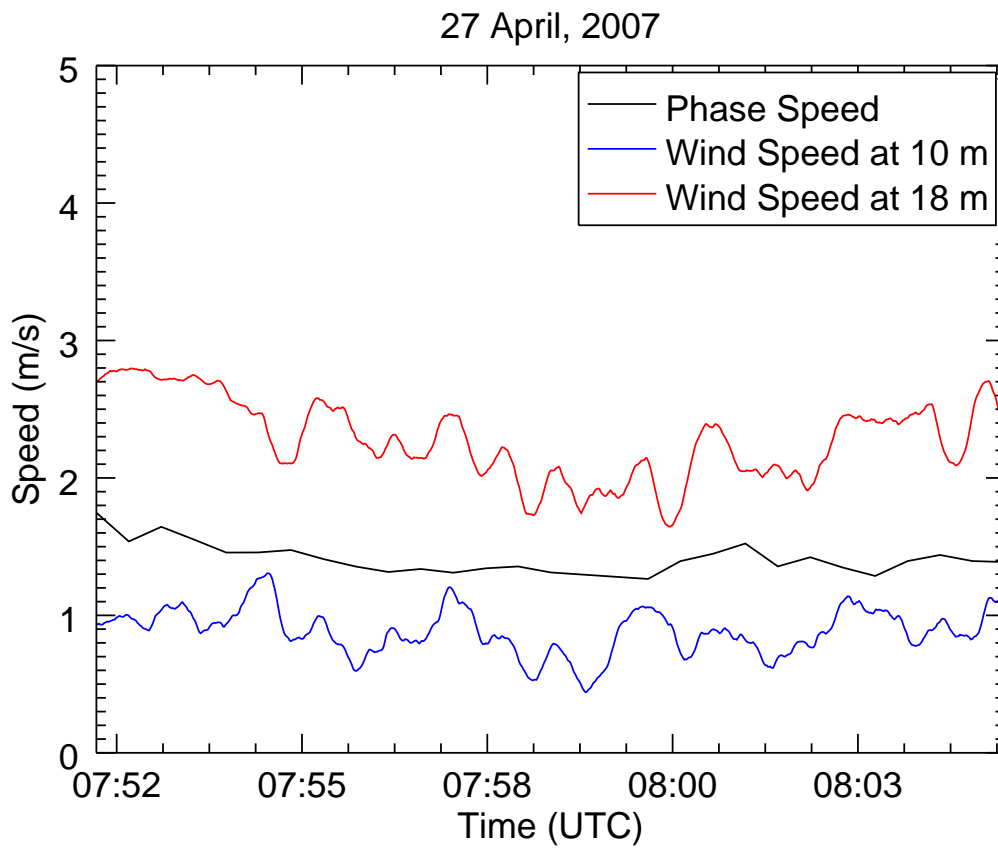
Figure 36. (Color required.) Time series of the phase speed as calculated by cross-correlation for every pair of frames on 27 April.

Case 3: 30 March 2007

The third episode that was studied in depth occurred from 23:45:10 to 23:52:29 PDT (7 min 19 s) (Figure 37). This case was previously discussed in Chapter IV as it was used to confirm that the waves were caused by dynamics. The lidar scanned only horizontally during this time frame creating a PPI every 17.5 s covering 60° scanning at a rate of about 15° s^{-1} at an elevation angle of 0.20°. This was the only case during the night of 30 March.

During this episode, the environmental lapse rate was stable at -0.21° m^{-1} from 10 m to 29 m with an average temperature of 13.9° C at 18 m. The wind shear, calculated from the same heights, is an average 0.065 s^{-1}. At 18 m, the mean wind is 1.89 m s^{-1} from a heading of 231°.

The period of oscillations according to the temporal autocorrelation of the in-situ data is 53 s. The vertical-velocity oscillations have an amplitude of approximately 0.2 m s^{-1}. The temperature at 18 m shows weak, incoherent oscillations, but the oscillations at 14 m are much more pronounced with an amplitude of about 1°, which may suggest that the waves in this case have a source closer to 14 m.

The lidar images show a very coherent wave packet, but the intensity is weaker than the two cases previously discussed. This may be due to the fact that the waves are in fact lower than the lidar scan plane. From the spatial autocorrelation, the wavelength is 53 m, strongly agreeing with the subjective estimate of 50 m (Figure 39). The average phase velocity determined from cross-correlation is 0.87 m s^{-1} propagating 49° N of E which is slower than the wind speed at 18 m and 10 m, 2.5 m s^{-1} and 1.25 m s^{-1}, respectively but matches the subjective analysis value of 0.8 m s^{-1} (Figure 40). Combining phase speed with

the wavelength from the lidar data values gives a period of 60. s, slightly higher than the temporal autocorrelation period.
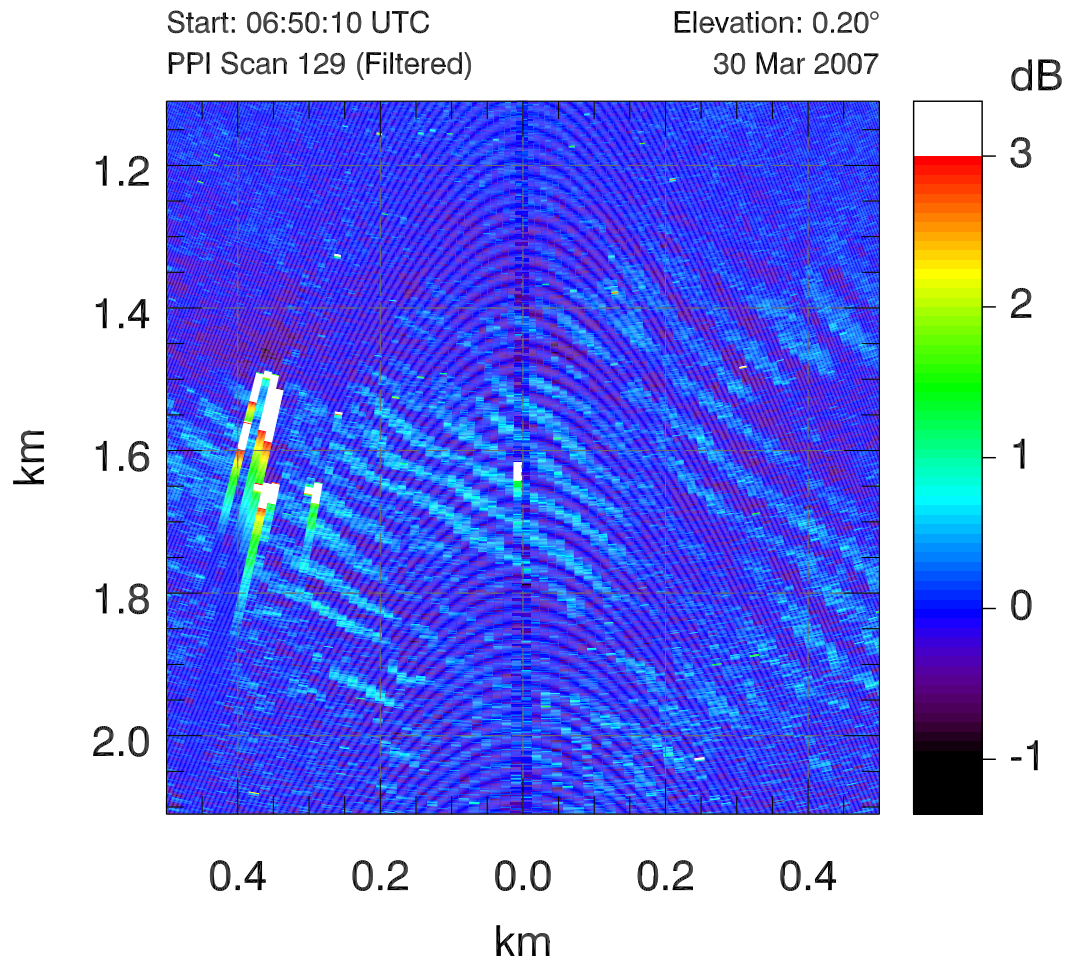
Figure 37. (Color required.) Lidar image for the wave episode on 30 March 2007 at 06:45 UTC (11:45 PDT on 29 March)
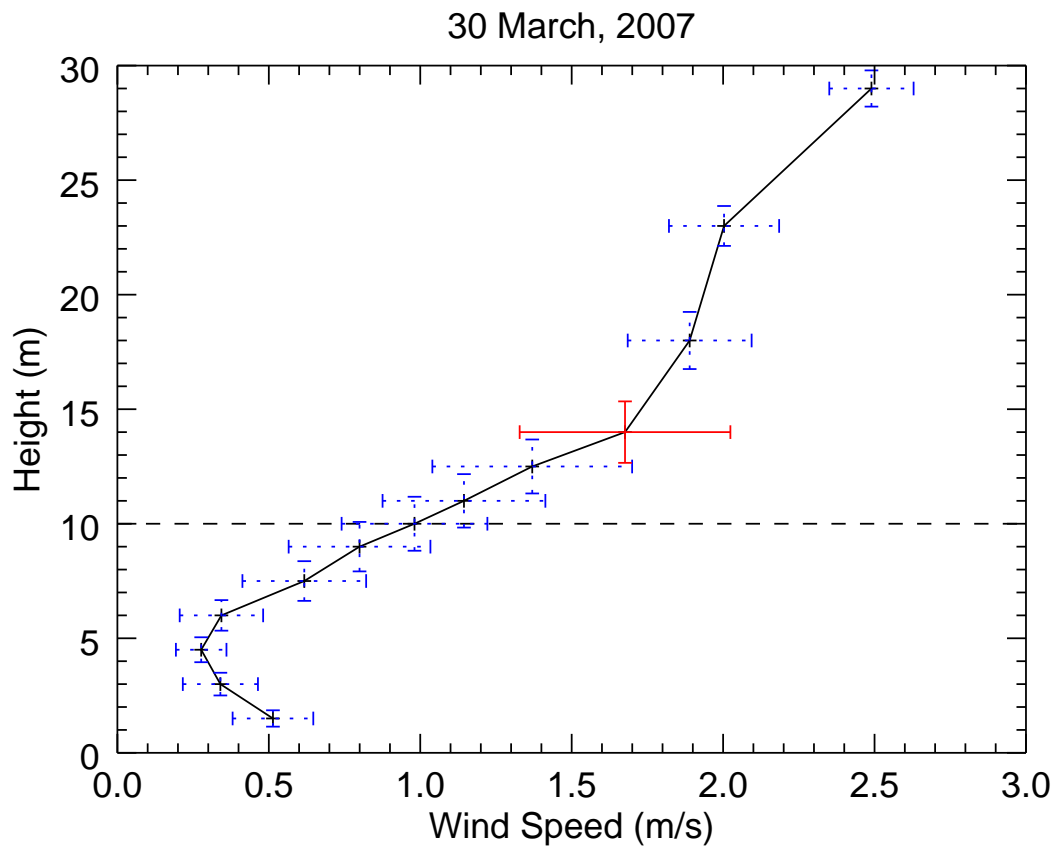
Figure 38. (Color required.) Mean wind speed profile for the 30 March wave episode. Plot is in same style as Figure 27.
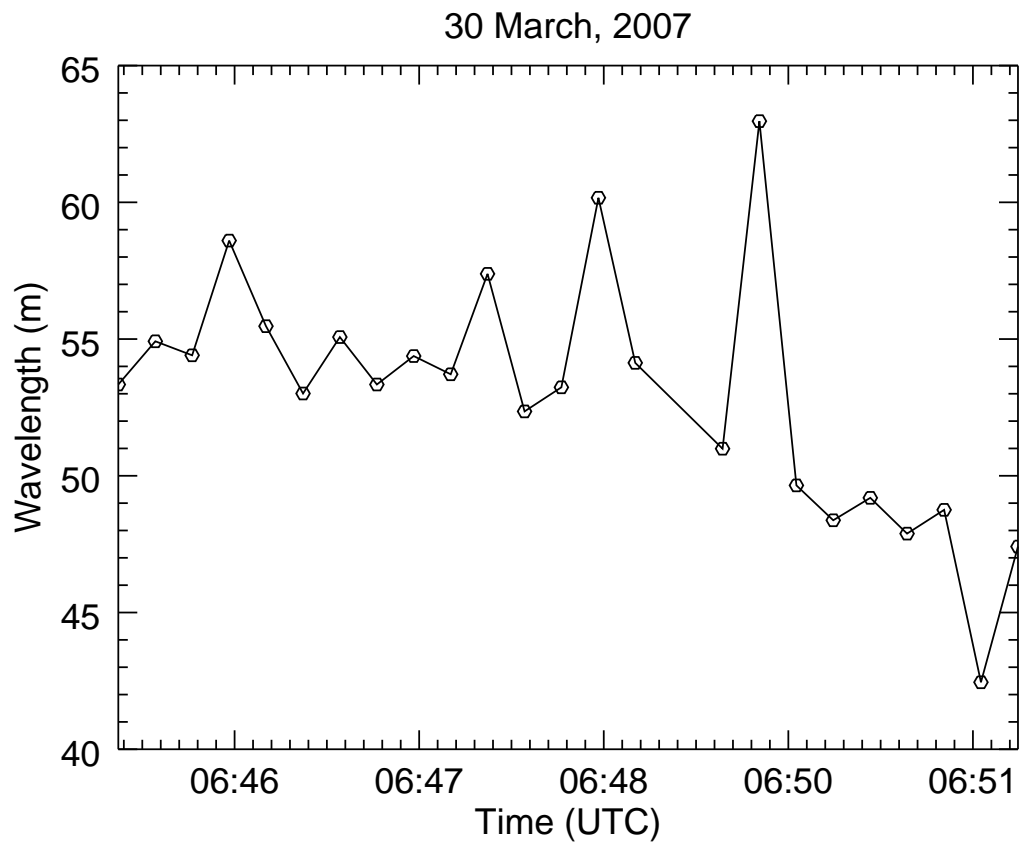
Figure 39. Time series of the wavelength that results from autocorrelation for every frame produced for 30 March.
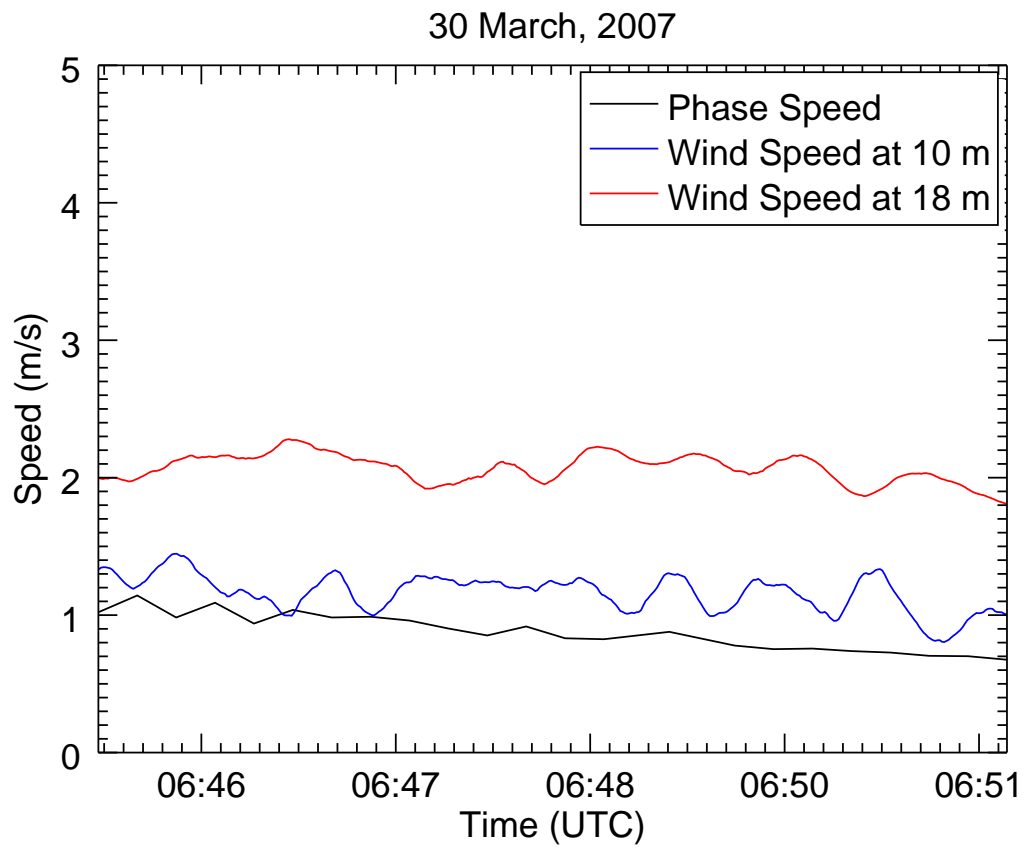
Figure 40. (Color required.) Time series of the phase speed as calculated by cross-correlation for every pair of frames on 30 March.

Case 4: 10 June 2007

This case (Figure 41) was chosen for presentation here because the narrow and slow scan produced high angular resolution data. This case occurred from 10:50 to 11:22 UTC (31 min 44 s). The lidar performed only narrow PPI scans during this episode leading to a better temporal resolution than most of the other episodes, completing a scan every 11 s. The scan speed resulted in an angular resolution of about 0.9° and each scan covered 9° of azimuth. Each image shows about 15 wave crests. Unfortunately, much of the data contains many spikes due to hard target reflections from the foliage extending into the scan plane. This suggests the lidar trailer leaned and the scan plane began to intersect to the top of the canopy

The atmosphere was statically stable with an average temperature gradient of 0.23 K m^{-1} from 10 m to 29 m and an average temperature of 16.1°C at the 18 m scan height. There is also a positive wind speed shear of 0.06 s^{-1} from 10 to 29 m.

Oscillations exist in the in-situ data during this case for the velocity and temperature. The amplitudes are lower in this case than in the one from 14 May with the vertical velocity amplitude being about 0.25 m s^{-1} (Figure 43) and temperature amplitude of about 1°C (Figure 42).

From subjective inspection, the wavelength appears to be 50 m and from the tower data, the period appears to be about 40 s. By tracing wavefronts, the phase speed was determined to be 1.1 m s^{-1} toward 75 degrees azimuth. When compared to the objective methods, autocorrelation gives a shorter wavelength of 39 m, but cross-correlation gives a similar phase speed of 1.0 m s^{-1} to the

subjective estimate. The period from these numbers is 38 s, which is shorter than the period from the temporal autocorrelation of 49 s.
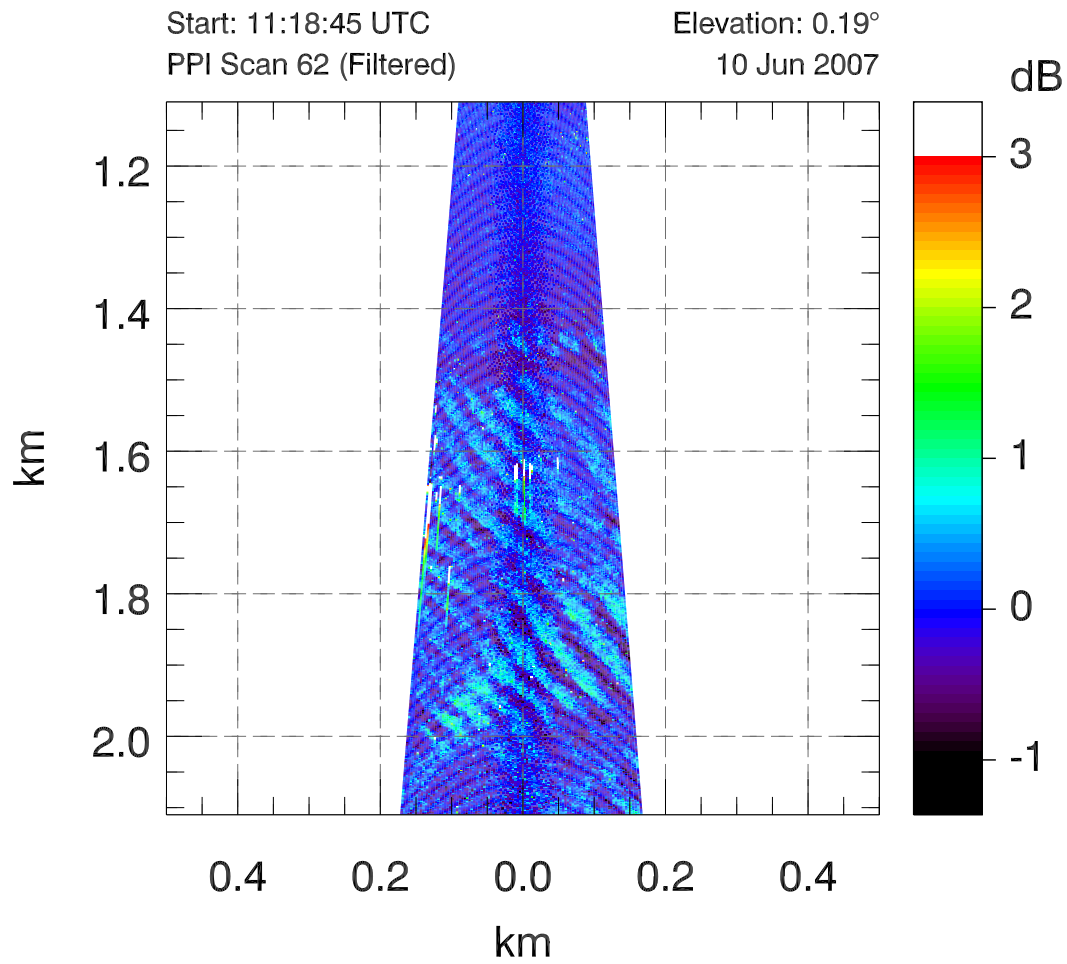

Figure 41. (Color required.) Lidar image for the wave episode on 10 June 2007 at 11:18 UTC
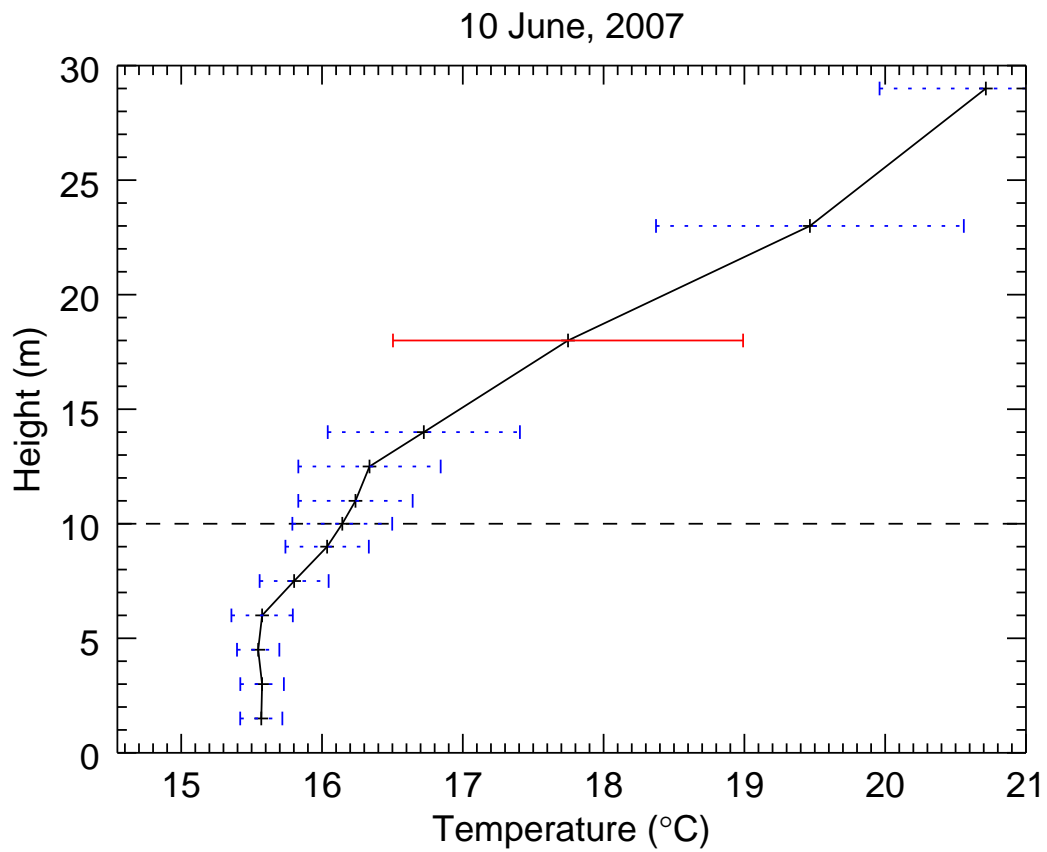
Figure 42. (Color required.) Mean temperature profile for the 10 June episode. The dashed line indicates canopy height.
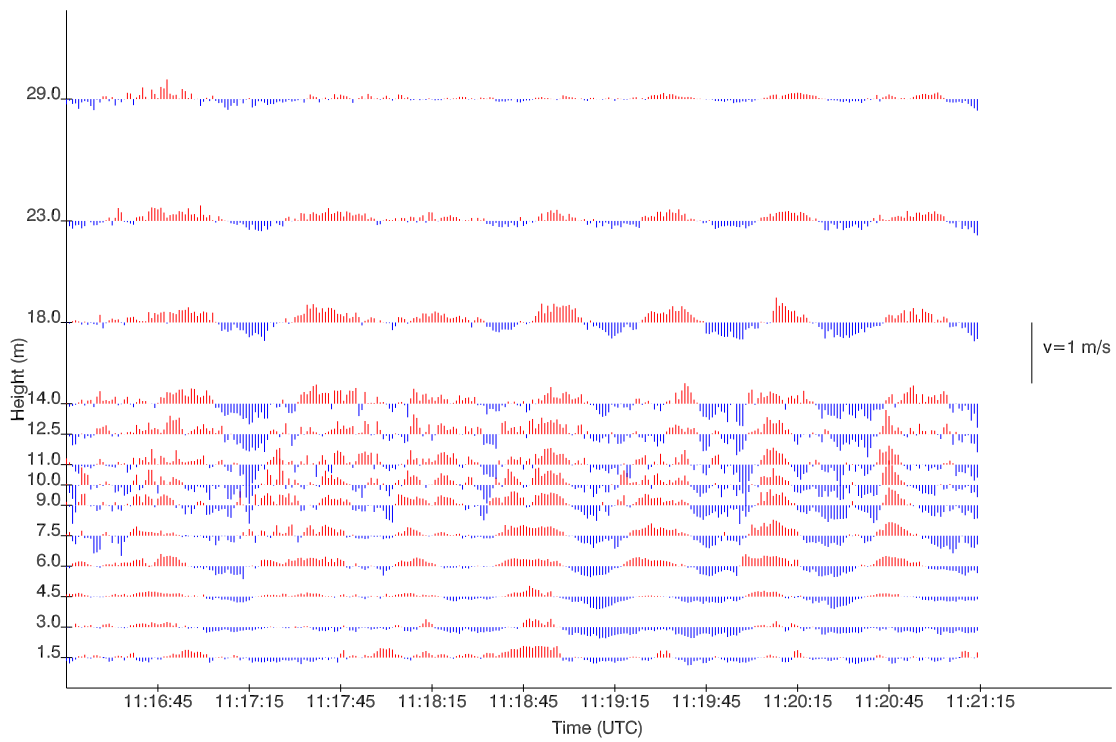
Figure 43. (Color required.) Vertical velocities on 10 June for all 13 heights plotted versus time. Red indicates upward motion and blue indicates downward motion.
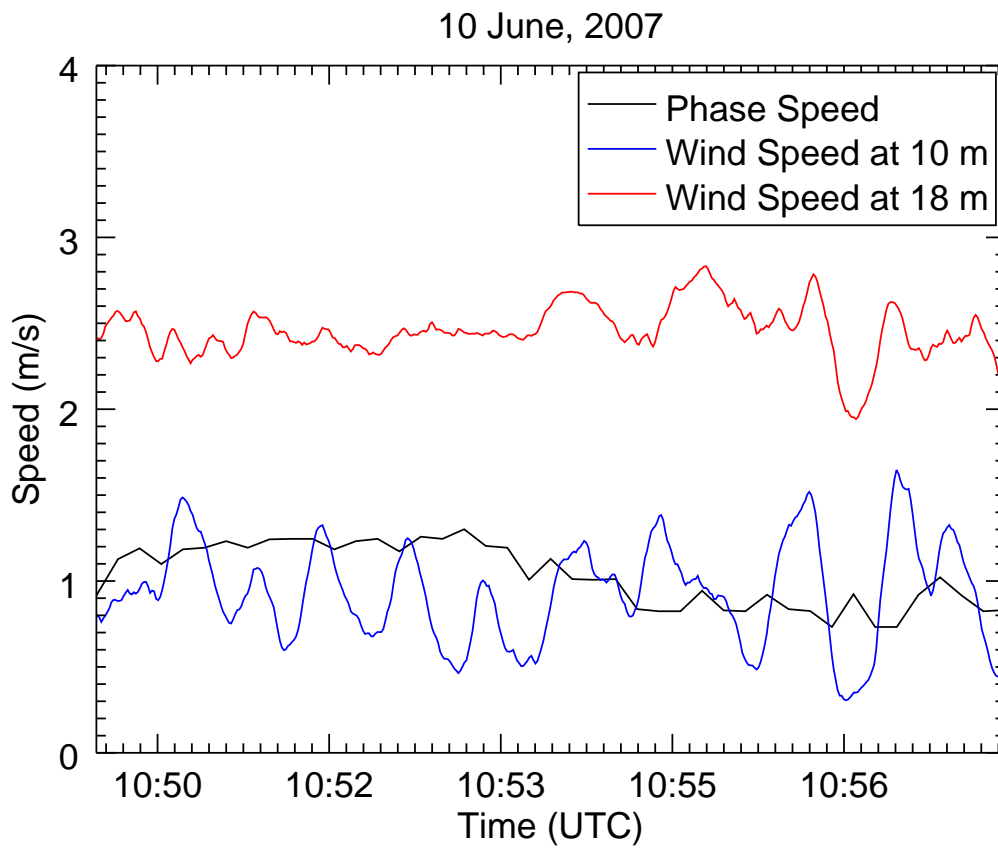
Figure 44. (Color required.) Time series of the phase speed as calculated by cross-correlation for every pair of frames on 10 June.
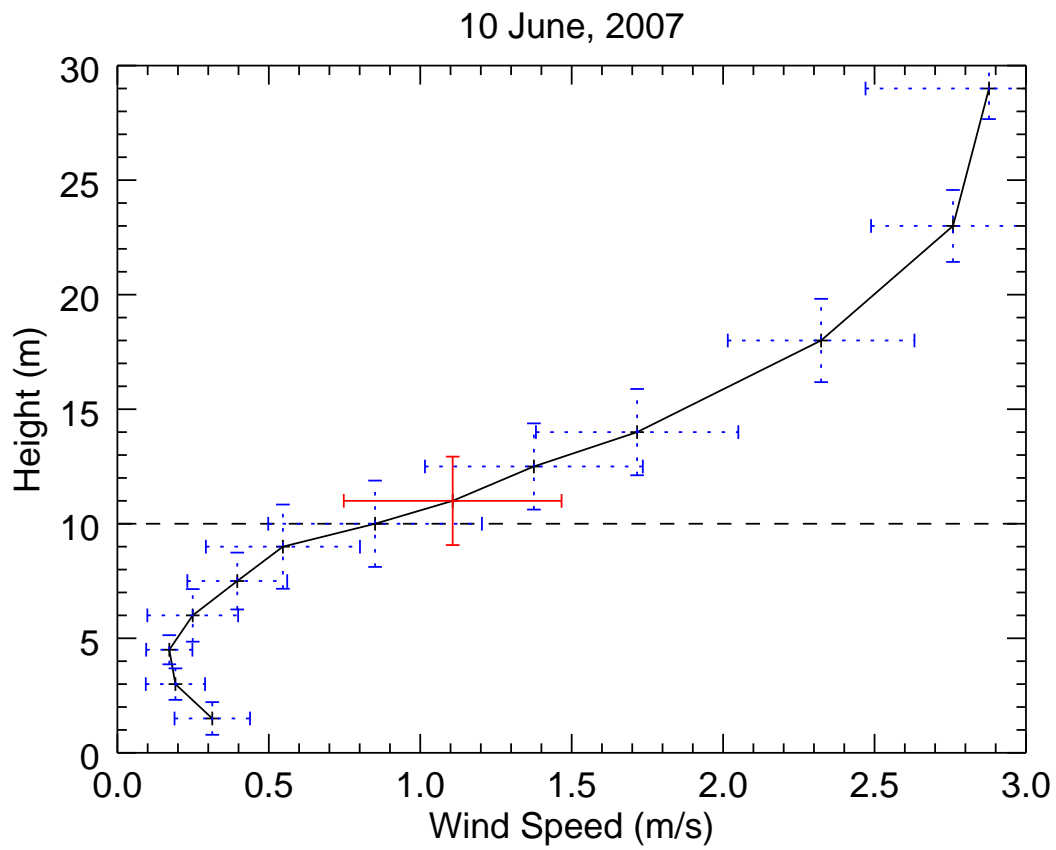
Figure 45. (Color required.) Mean wind speed profile for the 10 June wave episode. Plot is in same style as Figure 27.
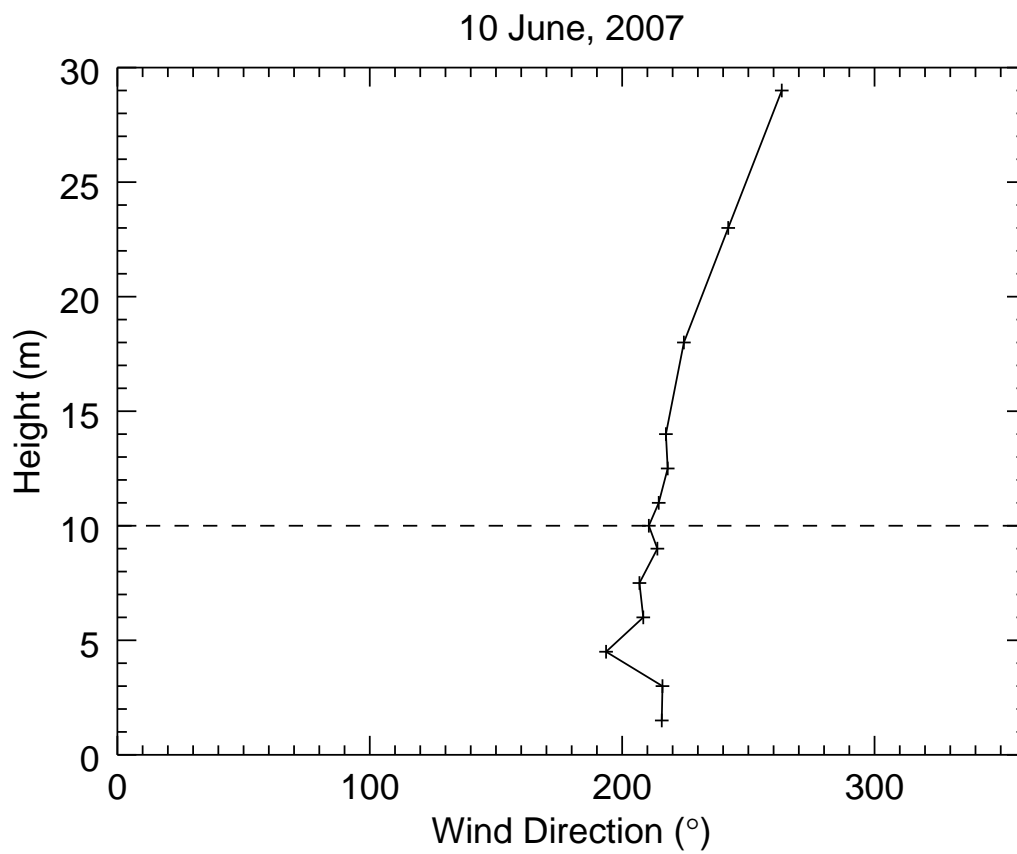
Figure 46. Mean wind direction profile for the wave episode on 10 June.

CHAPTER VI

STATISTICAL ANALYSIS OF ALL WAVE CASES

All fifty-two episodes occurred between 05:00 and 14:00 UTC (22:00 and 07:00 PDT) during stable nighttime conditions. None occurred during the day. The average wave episode duration was about 12 min while episodes ranged from 1 min 43 s to 1 hr 10 min 37 s. Wave episodes were detected on 28 of the 86 nights of CHATS. These episodes range in quality. That is, the episodes vary in backscatter intensity of the parallel bands, spatial coherence, and length of the episode. In addition to natural variability, the lidar scan strategy varied in the time between scans and the angle subtended.

A subjective analysis of the waves that involved tracing wave fronts (Figure 47) leads to an estimate of phase speed and direction. Through this analysis, it is shown that the waves tend to travel in the direction of the wind (Figure 48). Based on this observation, the autocorrelation function was computed for a subjectively placed line that intersects the wavefronts perpendicularly and is parallel to the wind direction as determined from the vertical tower at 18 m (Figure 49). With these periodic functions, the autocorrelation function is also periodic with maxima that occur at wavelength multiples. The distance to the first local maximum is determined and indicates the wavelength. A drawback to this method is that it requires an arbitrary choice of one of many parallel lines to the wind direction for each frame that included a wave episode while ignoring most of the backscatter image. It also requires a choice of height from which to use in situ

data. The data from 18 m was typically used, but as shown earlier, there can be significant directional shear at through the altitudes measured by the tower, so 18 m may not be the optimal choice in all cases. Furthermore, the lidar scan plane may have been higher or lower than 18 m depending on the pitch of the lidar trailer. The distance from the origin to the first local maximum indicated the wavelength. Here the direction, $\arctan(y/x)$, is ignored because the waves do not appear to always move exactly $90°$ from the wave front. Also, if the wrong angle was chosen, the apparent wavelength would be too long by a factor of $\sec(\theta) - 1$, where θ is the angle from the true wavevector. For these reasons, this technique was abandoned in favor of the more general, though more computational intensive, two-dimensional autocorrelation (Figures 50 and 51).
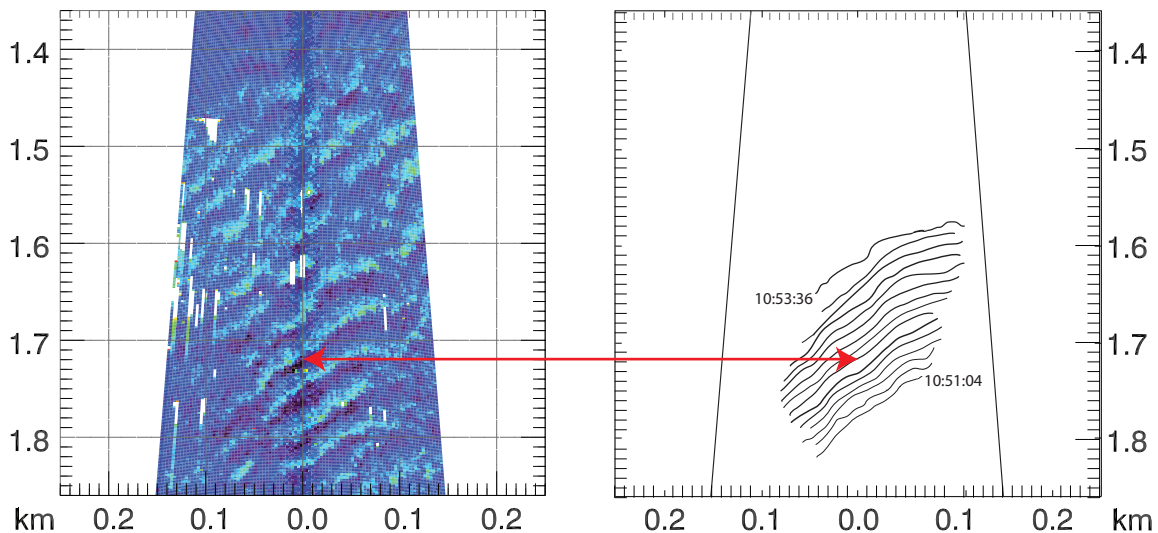

Figure 47. (Color required.) Subjective analysis of phase speed and direction. One wave crest was traced for a sequence of scans to see its displacement over time. The red arrow indicates which crest in the left image corresponds to which traced crest in the right. The sequence goes from 10:51:04 to 10:53:36 UTC on May 25 2007. The subjective phase speed here is 0.91m s^{-1} .
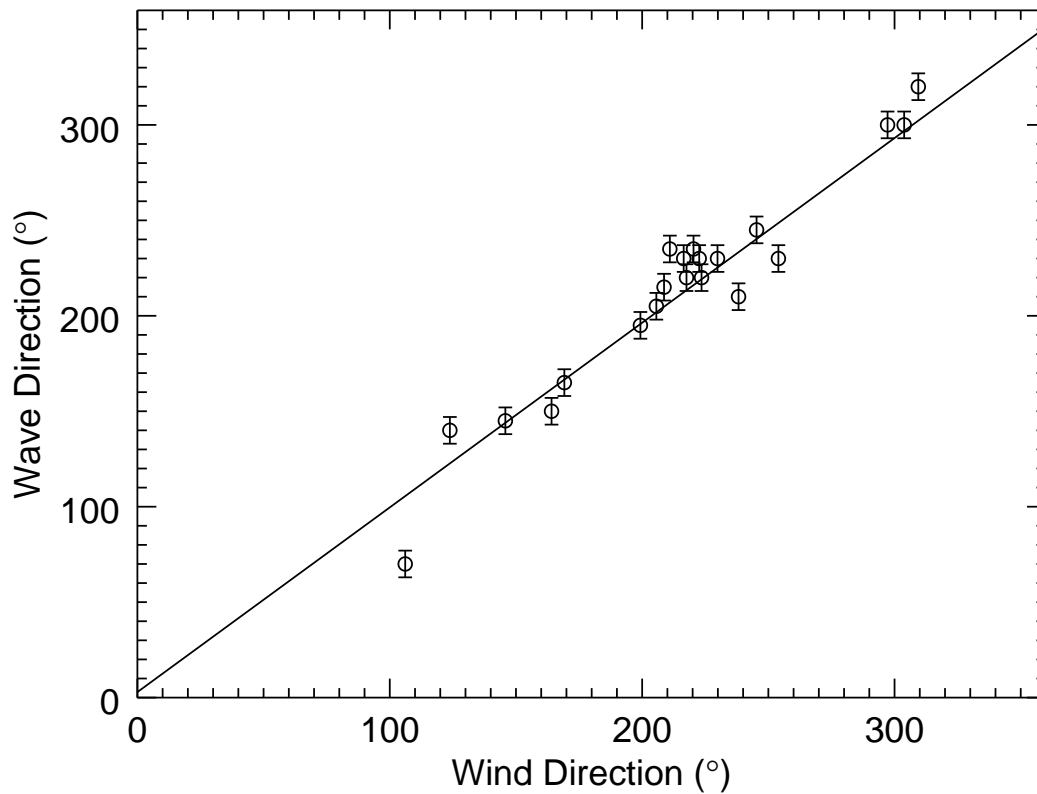
Figure 48. Plot of wave propagation direction (determined subjectively) versus wind direction at 18 m from the sonic anemometer for 22 wave cases showing that the waves are propagating in the direction of the mean flow.

Since the REAL is unique in being able to elucidate the spatial characteristics of these waves directly, there are no independent measures of wavelength. The subjective wavelength measurements were compared to the objective calculations from autocorrelation (Figure 52). The subjective analysis of the waves was to the nearest ten meters. The uncertainty of the objective wavelength is harder to determine but is estimated to be about 5 m. The two methods agree well to confirm the autocorrelation effectively determines wavelength

but it appears that either the autocorrelation procedure underestimates the wavelength or the subjective bias overestimates.

The phase velocity determined by cross-correlation has was compared to the wind speeds at various heights and the wind direction. The phase speed was compared to both the 10 m and 18 m wind speeds for the canopy height and altitude of the lidar scan (Figure 53). The waves' phase speed is always lower than the wind at the lidar scan height of 18 m and most often lower than the speed at the canopy height of 10 m. Some outlying wave cases were omitted whose speed was much lower than that of the wind speed. The backscatter intensity of the crests of the waves in the omitted scans was very weak and was usually accompanied by some stationary feature such as a region of low backscatter at the north edge of the orchard. This may bias the average distance in the cross-correlation maxima toward zero. The wind direction can be compared to the objective propagation direction (Figure 54) reinforcing the conclusion that the waves travel with the wind. The scans omitted in the phase speed analysis were also omitted for the direction analysis.

Most of the cases occurred when the wind came from the SW, but the headings range from 110° (ESE) to 310° (NNW). All of the cases show more prominent waves directly over the orchard canopy with a weaker or no trace of the waves north of the canopy. The northern edge of the canopy is the only forest edge in the 1 km^2 study area with the exception of road aligned north-south approximately 150 m from the eastern edge of the study area. The prevalence of the waves over the canopy and only over the canopy further support the hypothesis that the waves are the result of shear induced by the canopy.

All of the discovered wave episodes occurred at night. Since the NBL becomes increasingly more stable throughout the night, wave activity increases

somewhat as the night progresses (Figure 55). There are no wave cases that occurred within the first hour after sunset and only two that occurred within the first two hours. Twenty-eight of the 52 wave episodes (54%) began more than 6 hours after sunset. Seventeen cases (33%) occurred more than 8 hours after sunset. No cases occurred more than 10 hours after sunset. The length of time between sunset and sunrise on the day of the first wave episode in the set, 19 March 2007, was 12 hr 5 min. This time decreased to 8 hours 56 min on the date of the last wave episode, 10 June 2007 (*Time and Date AS*, 1995).

The period of these waves, whether it is found from the in-situ tower data or the lidar data, is less than the Brunt–Väisälä period. Alternatively, the frequency is always higher for the waves than the Brunt–Väisälä frequency. Brunt–Väisälä is thought to be upper bound on frequency and the lower bound on period for the waves because the restoring forces, gravity and buoyancy, cannot oscillate parcels any faster than this theoretical limit. However, we observe parcels from an Eulerian frame, while the theoretical periods are calculated for a Lagrangian frame.

Since the waves propagate in a fluid medium which is moving, the frequency measured in situ is Doppler shifted. Since the Brunt–Väisälä frequency is calculated from the data collected at 18 m AGL, the velocity of the wind is subtracted from the phase speed determined from the lidar data so that the data is in a reference frame moving with the wind. This allows calculations of an intrinsic frequency which is lower than the observed frequency and an intrinsic period which is longer than the observed period. The intrinsic quantities are closer to the Brunt–Väisälä frequencies and the corresponding periods (Figure 57). The wind speed at 18 m is used because it is the closest to the height of the lidar scan plane and it is believed that the wavelength and phase speed are constant in height. If

the wind speed at canopy height is used, the period grows even more. In the cases in which the wind speed approaches the phase speed at or above canopy height, the frame that is translating with the wave observes a frequency that approaches zero and the intrinsic period goes toward infinity.

The study is unique in that the lidar data allow direct measurement of wavelength. Following the two methods used by Lee (Chapter I, Equations 71 and 73), theoretical wavelengths were determined entirely from the data taken from the in-situ tower (Figure 58). Both methods yield results within an order of magnitude for the lidar observed wavelength, but both show weak to no correlation. Since the wavelengths measured subjectively and objectively agree, and since the wavelength is used to calculate a period that is consistent with the in-situ data, the lidar measurement is taken to be more reliable as it doesn't rely on data from a single point location from which to extrapolate spatial data.
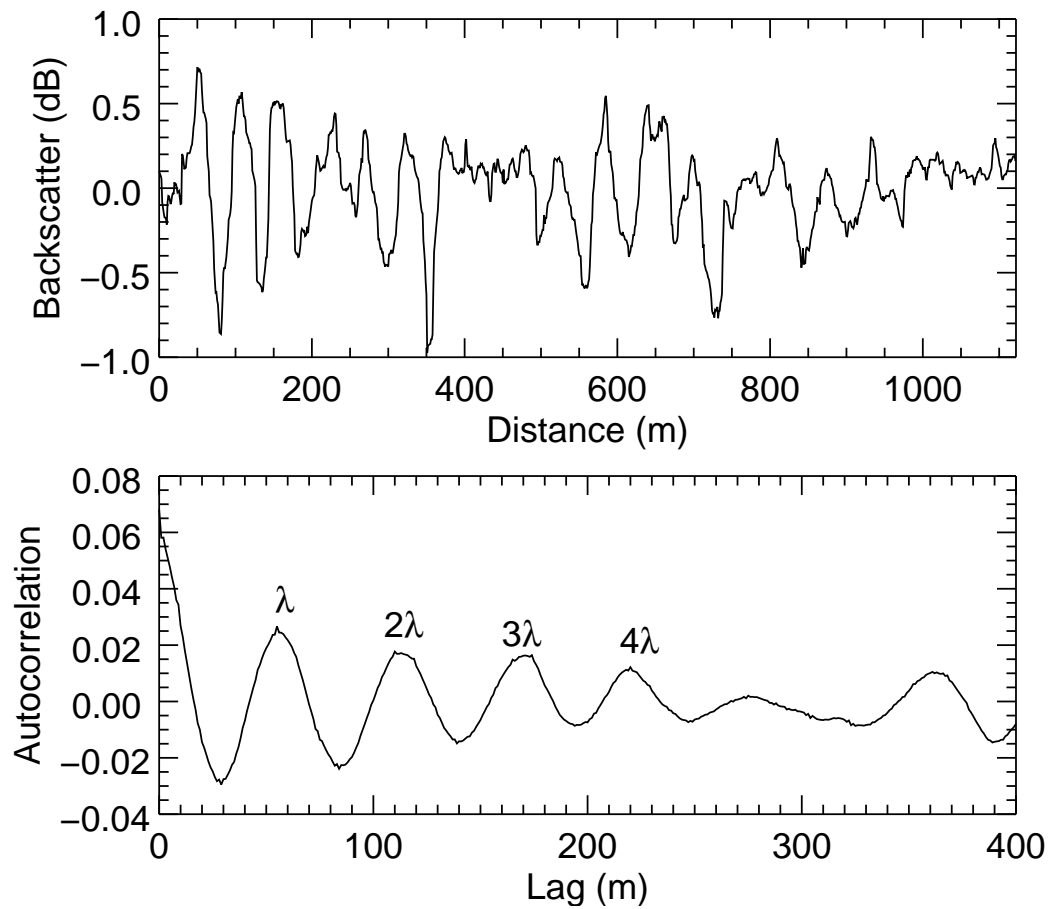
Figure 49. The top plot shows one-dimensional slice of range-corrected, high–pass median filtered backscatter intensity from 14 May 2007 at 9:06:38 UTC in the streamwise coordinate system. The bottom plot shows autocorrelation function for slice in top plot with peaks at wavelength-multiples, the first of which is at 55 m agreeing with the subjective measurement of 60 m.
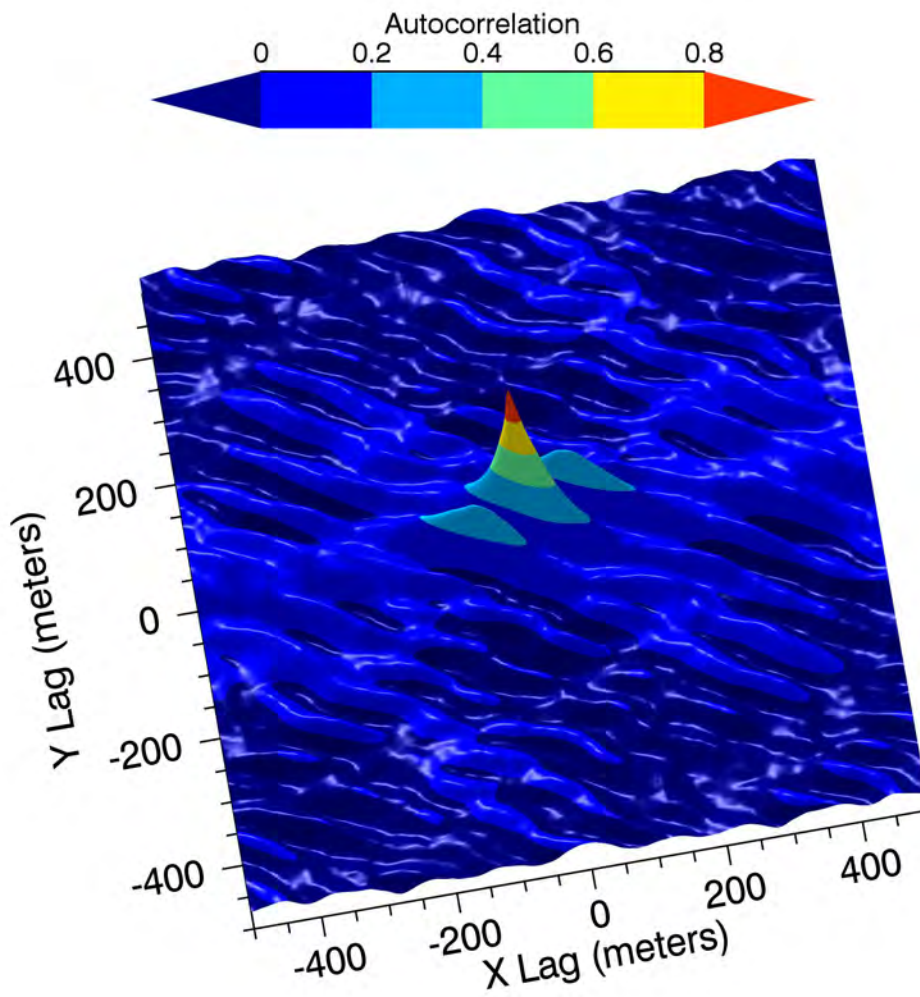
Figure 50. (Color required.) Two-dimensional autocorrelation function for the same time as in Figure 49 for 14 May. The wavelength here is 78 m.
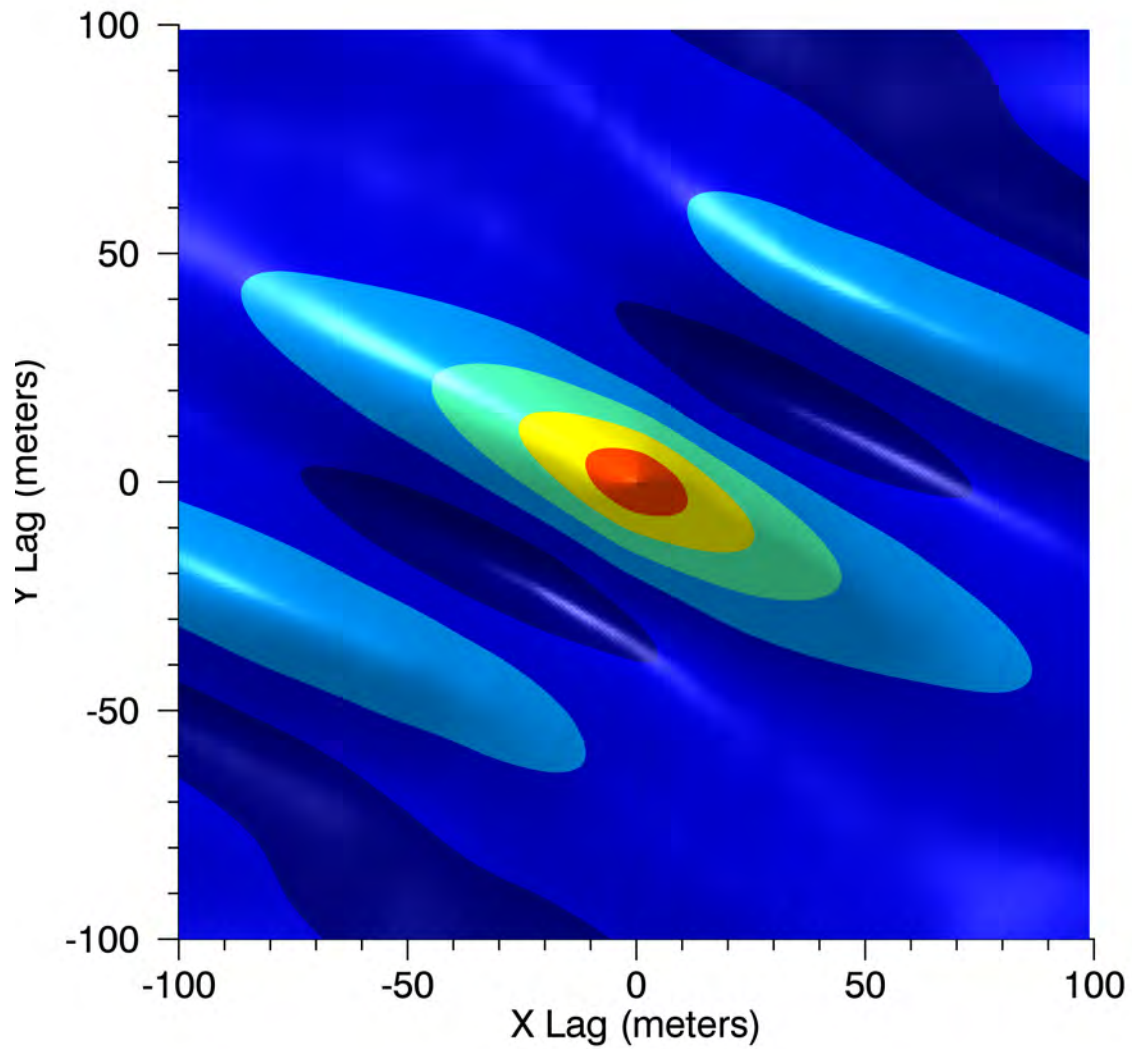
Figure 51. (Color required.) Zoomed in on the center of Figure 50. Two-dimensional autocorrelation function for the same time as in Figure 49. The wavelength measured here is 78 m.
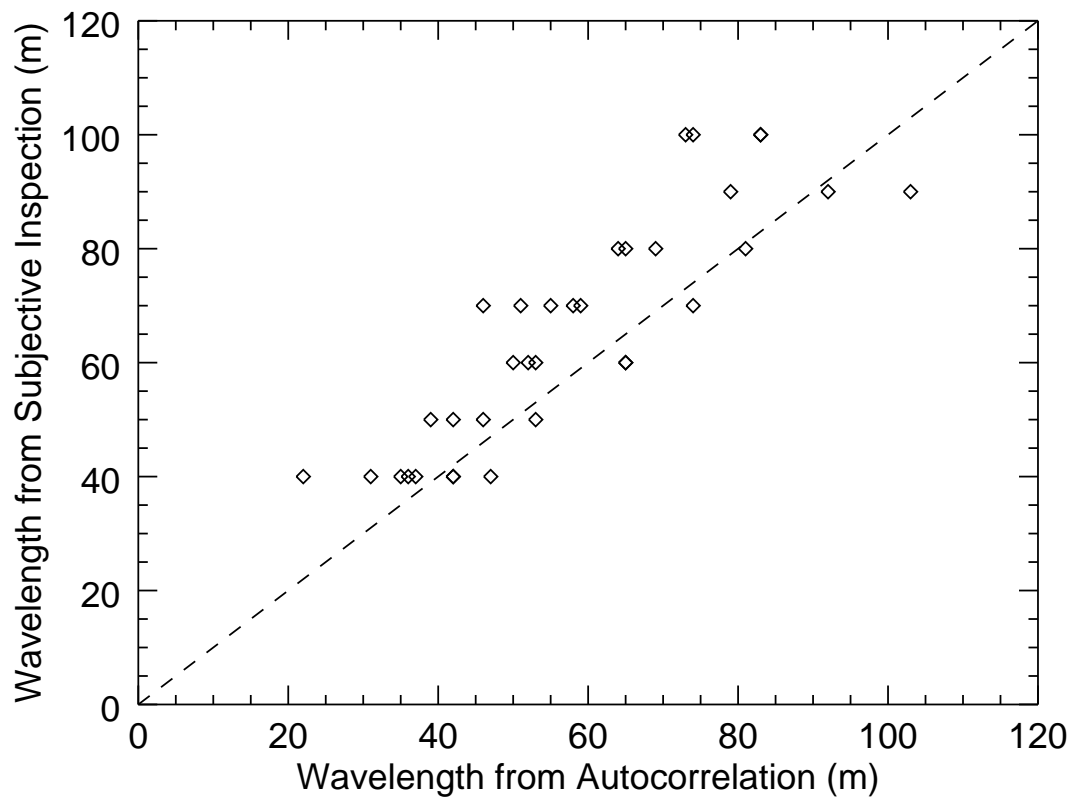
Figure 52. Scatterplot of the subjective wavelengths that were initially assigned to the wave episodes upon discovery versus the mean wavelength versus the episode. Subjective wavelength measurements were made to the nearest 10 m versus the wavelength derived from the autocorrelation algorithm are to the nearest 1 m.
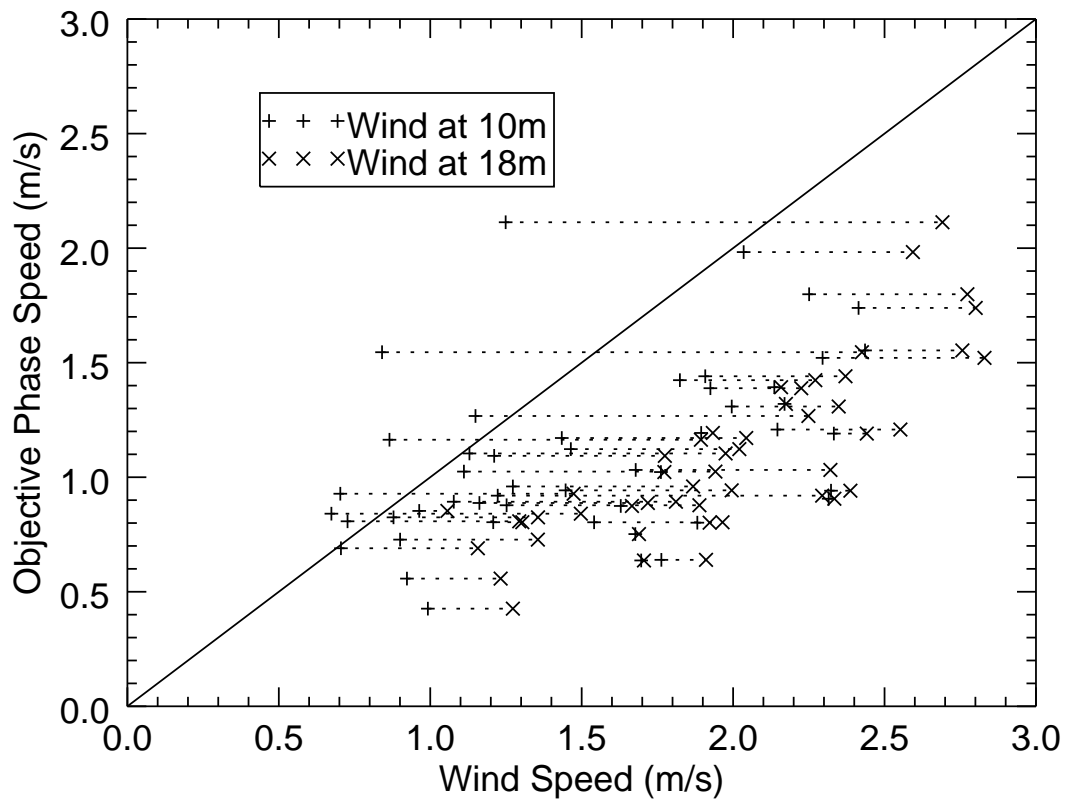
Figure 53. Scatterplot comparing the lidar-determined phase speed against the in-situ wind speed. The phase speed is always less than the wind speed at 18 m, the height of the scan plane, and usually less than the speed at 10 m, the height of the canopy.
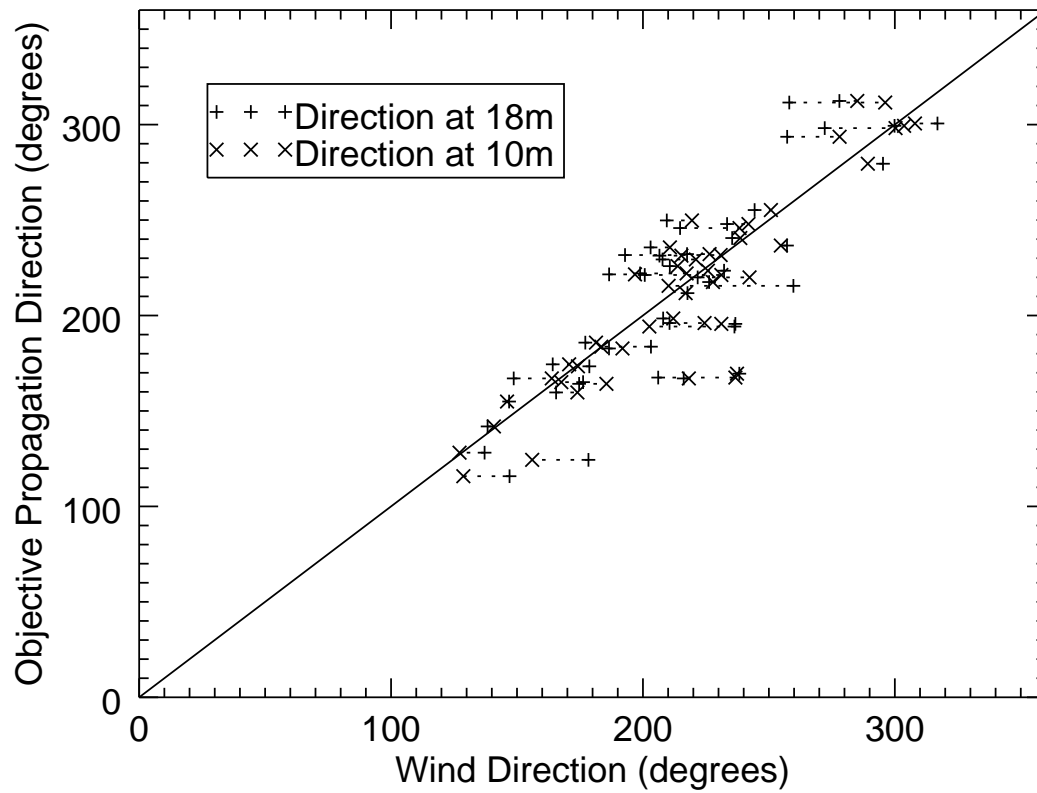
Figure 54. Scatterplot comparing lidar-determined propagation direction versus the in-situ wind direction. Usually the propagation is somewhere between the direction at 10 m and the direction at 18 m.
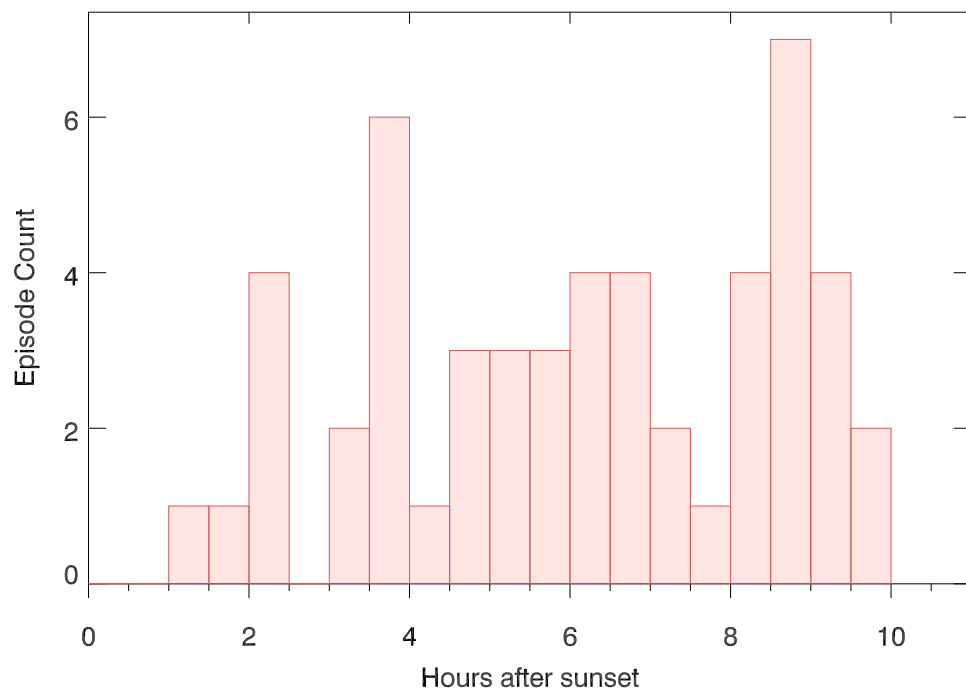
Figure 55. Histogram of the time after sunset that the onset of waves occurred binned into 30 min intervals.
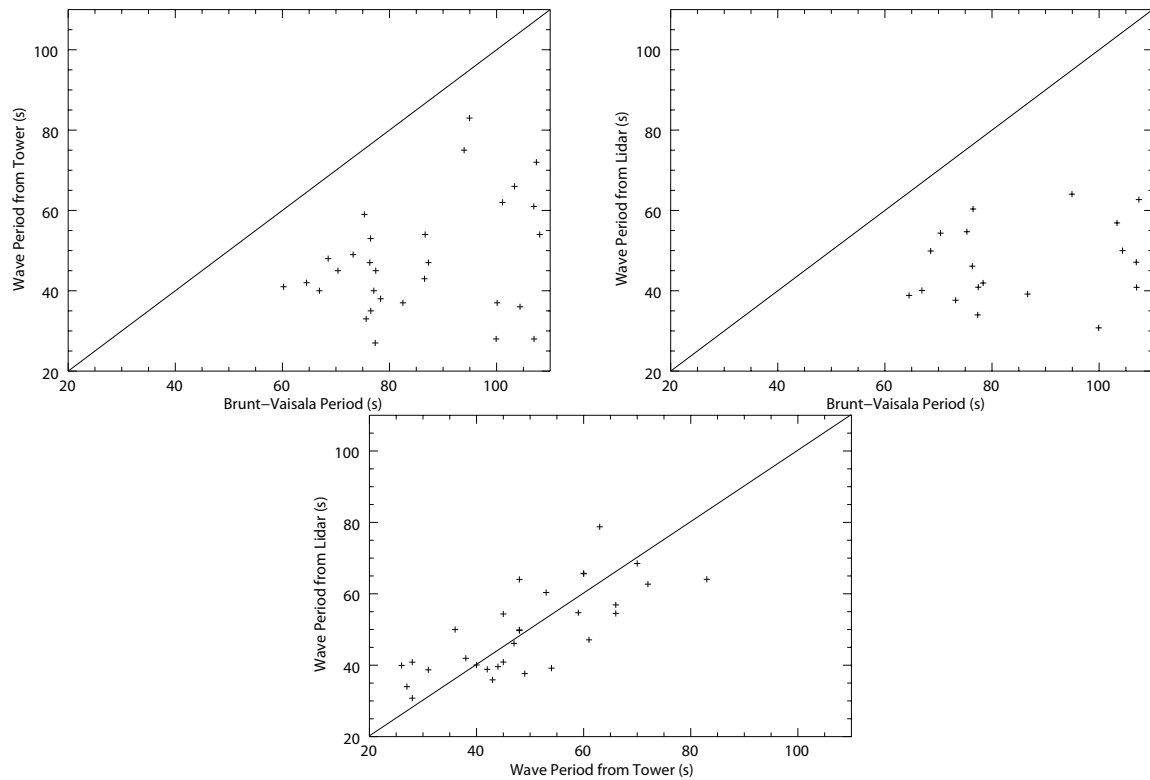
Figure 56. Scatterplots of periods shown. The top left plot is the tower-derived period versus the period calculated from the Brunt–Väisälä frequency. The top right plot is the lidar-derived period versus period from the Brunt–Väisälä frequency. The bottom plot is the lidar-derived period versus the tower-derived period. All three plots show the line $y = x$ for clarity.
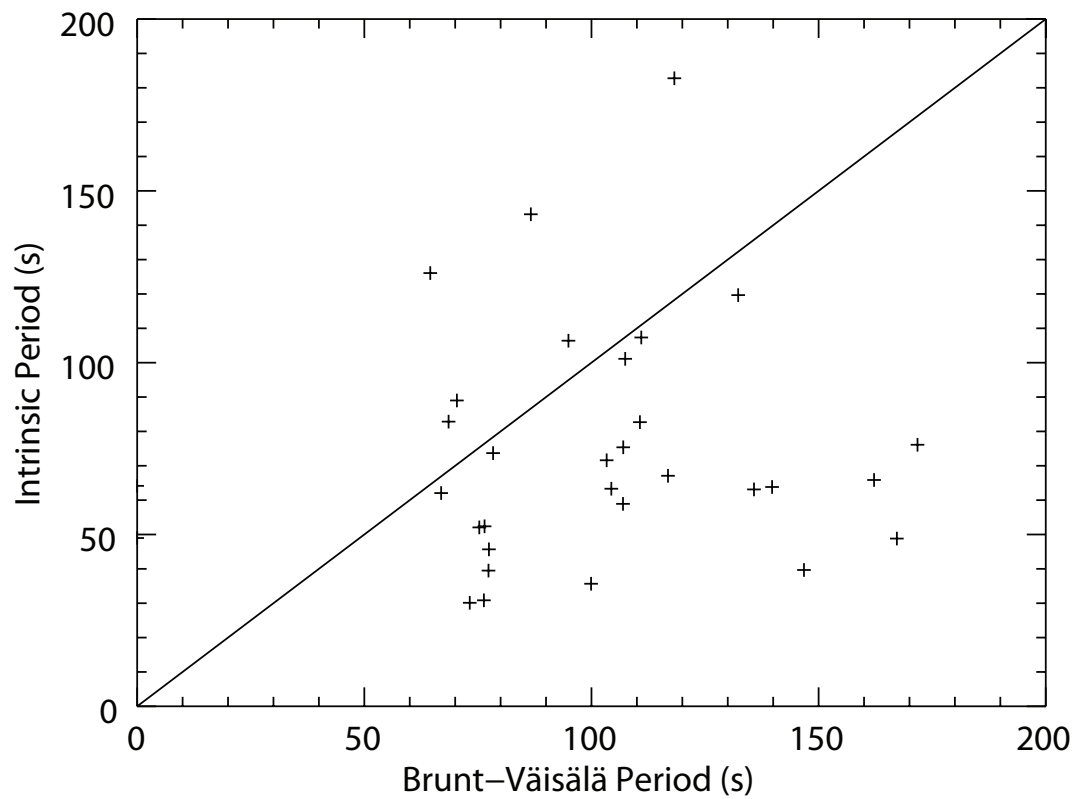
Figure 57. Scatterplot of the intrinsic period of the waves when calculated from a reference frame traveling at the speed of the wind at 18 m versus the period calculated from Equation 56 in Chapter I. The line $y = x$ is plotted for clarity.
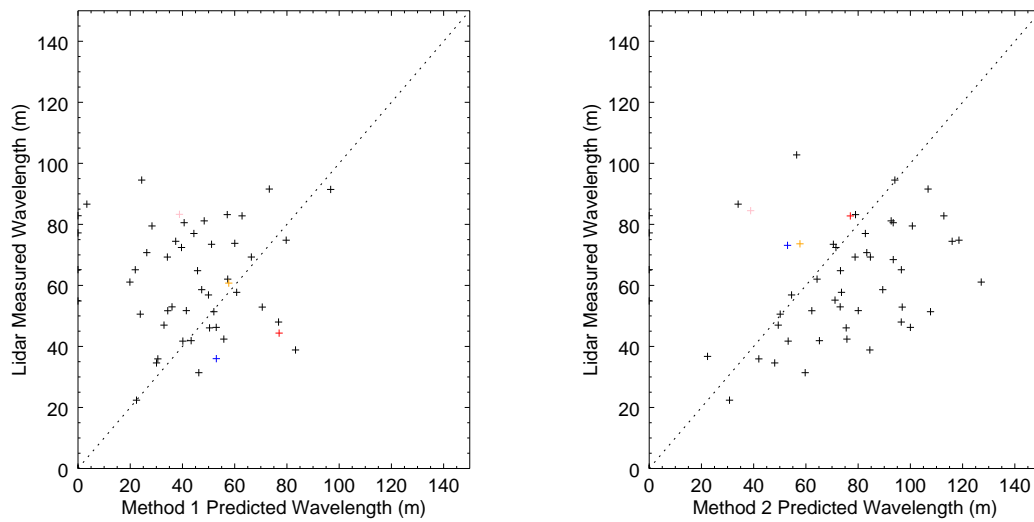
Figure 58. (Color required.) Theoretical wavelengths from in-situ data versus the observed wavelengths in the lidar data. The left plot shows the method outlined by *Lee et al.* (1997). The right plot shows method by *Hooke et al.* (1973). Red indicates 14 May case, blue is 30 March, orange is 27 April, and pink is 10 June cases described in Chapter V for both plots.

CHAPTER VII

CONCLUSION

The horizontally scanning eye-safe elastic backscatter lidar can identify
the presence of microscale gravity waves over forest canopies. The lidar images
contain quantitative spatial information such as wavelength and phase velocity that
is not available from in-situ time-series data. A key requirement for such lidar
measurements is high spatial resolution images and sensitivity to small changes in
aerosol backscatter. Radial high-pass median filtering is used to clarify the presence
of the waves in the images. This enables the instrument to resolve wave structures
that occur on scales of tens of meters.

The presence of waves in the in-situ velocity and temperature data
during the same time periods as the waves observed in the lidar images and
time-lapse animations confirms the waves are a local dynamic phenomenon and not
some artifact of the lidar system or aerosol structure that advected into the
observation region from elsewhere.

With images produced from the lidar data, the wavelength of the waves
can be subjectively and objectively determined. Wavelengths range from about 40
m to 110 m. The wavelengths were calculated for every frame providing time series
of wavelength and revealing the evolution of the wave spacing in time.

With consecutive images, the phase velocity of the waves was determined
subjectively and objectively. The waves propagate in the same direction as the
wind. Their speed is always slower than the wind speed at the lidar scan height

(presumed to be 18 m AGL) and typically less than or equal to the speed at the inflection point. With both the phase speed and wavelength, the period of the waves was determined. The periods were confirmed with the period from the in-situ tower data.

The canopy waves studied all occurred at night in stable to very stable conditions with an increasing temperature with respect to altitude. Wave episodes tend to occur later at night when static stability is stronger.

The waves occurred when there was a sheared wind profile. This shear profile has an inflection point due to the drag induced by the canopy. This inflection point is the source of wave generation. The waves disappear in the absence of trees north of the canopy. The maximum amplitude is at or near the inflection point in the mean wind profile.

The waves are evanescent as shown by their uniform phase through the height of the tower and their decreasing amplitude with height. The oscillations in vertical velocity are 90° out of phase with the temperature perturbations which shows little to no vertical thermal flux. The oscillations in vertical velocity are also 90° out of phase with the horizontal velocity that shows low horizontal momentum flux in the vertical direction. Transporting no energy or momentum vertically is a property of evanescent waves.

Limitations of the Study

CHATS was designed primarily to study turbulence structure rather than waves. Canopy waves were found in the extensive REAL data set but not until after the completion of the campaign. Therefore, the scan strategy was not optimized to study waves. Scans sometimes were narrow which gained some temporal resolution but at the cost of valuable spatial data. Other scan profiles

interleaved RHI's and PPI's leading to a coarse temporal resolution of about 30 s, approximately the same as the period of the higher frequency waves observed, potentially leading to problems in the ability to observe phase propagation.

The study focused only on the structure observed in the conic section created by the PPI scans. The vertical structure could not be studied in the lidar data because the RHI's were such that the angular separation between consecutive pulses at canopy height did not provide adequate vertical spatial resolution. The tower did provide insight to the vertical extent of waves, but the highest sensors were at 29 m AGL where there was still wave motion, so the full vertical extent of the waves could not be observed.

The PPI scans were collected at some angle above the horizontal so that lidar the beam, emitted from below the height of the trees, would be above the trees when it reached the northern edge of the orchard. By the southern edge, the beam was well above the height of the trees. Further south, the beam was far above the height of evanescent waves. Specifically, the REAL beam scanned with a slope of 8.6 m up for every 1 km in range. Therefore, if the beam was at 18 m AGL at the range of the tower, it would be approximately 24 m AGL at the range of the far end of the orchard and 50 m AGL at approximately 5 km range. Furthermore, the beam was assumed to be at or near 18 m AGL for the duration of CHATS. However, since the trailer tipped due to flooding of a nearby trench, the height of the lidar scan could only be estimated to within several meters. Therefore, some of the analysis comparing lidar and in-situ measurements may have referenced data collected at an incorrect height. Fortunately, since the waves were vertically coherent through the height of the tower, the effect on this analysis is minimal.

Despite the extensive data, some questions went unanswered. The cause of the areas the high backscatter, specifically the wave crests, was never fully

explained. A hypothesized explanation was offered in Chapter I that aerosol in the NBL tend to have higher concentration at the bottom. Wave motion displaced regions of higher concentration to higher altitudes which form wave crests, and regions of low concentration were displaced to lower altitudes which form troughs. Verification for this explanation could have come in the form of a time series of backscatter at the tower versus vertical velocity. The oscillations in vertical velocity should lead the oscillations in backscatter by 90°. However, to use points at the tower from a lidar scan gives only a single point for every scan. From these sparse measurements, no definitive conclusion could be made.

Future Work

Observations of the atmosphere provide necessary information for accurate simulations of the atmosphere. A worthwhile activity would be the development of a computer model using the environmental conditions recorded at CHATS during wave episodes to attempt to recreate waves. Since the lidar scans only a two-dimensional plane or conic section, a simulation would contribute to the understanding of canopy waves by providing the full three-dimensional structure. This microscale model could provide the subgrid-scale parameterization for larger models in weather forecasting.

This is the first study of its kind, so there is still significant future work that can be done. An experiment similar to CHATS but with its focus on canopy waves could scan a lidar beam horizontally above an orchard canopy across one or preferably multiple in-situ towers. With multiple towers, the spatial variables such as wavelength and phase speed could be confirmed. The scan should be wide enough to cover approximately 1 km^2 centered at a tower, but not so wide that the time interval between scans is any longer than it needs to be to meet the first criteria.

The scan profile should be such that there are only PPI's or that there are interleaved RHI's that have a much smaller angular separation between pulses so that the vertical structure of canopy waves can be resolved. The RHI's in CHATS scanned too quickly to resolve waves in the vertical. Two lidars operated simultaneously could provide vertical and horizontal cross sections.

The REAL has the capability to broadcast scans near real time. Therefore, the onset of a wave episode could alter the scan profile to fit the study's needs without interrupting other studies done by the REAL. To do this would require constant surveillance of the data. So that a person does not need to constantly monitor the output, especially considering canopy waves occur at night, algorithms that identify the onset of waves could be developed to eliminate the current requirement for monitoring the entirety of the output. Techniques used for this research, such as autocorrelation, could be used, but they alone do not have the same capability as a person to recognize waves. Advancements in neural networks have been made that enable recognitions of patterns in data, and may be used in future work to identify wave episodes in real time or in existing data sets.

Most of this study focused on the time and place of waves, but the flow around the canopy and the state of the atmosphere before and after the waves is of interest. The interaction of these waves with turbulence could also be studied. Waves can potentially break into turbulence or simply dissipate due to viscosity.

The analysis shows that the waves do not transport thermal energy or momentum vertically. This is consistent with previous expectations for evanescent fluid waves in stably stratified fluids (*Stull*, 1988). This is not to say the NBL with canopy waves does not tranport heat or momentum. Intermittent turbulence is known to exist in NBL, especially in environments with sheared wind profiles and low Richardson numbers. Turbulence is an effective transport of thermal energy,

momentum, and trace gases. It is possible that the waves are a phenomena in the transition from purely horizontal, laminar flow, to turbulence (*Nappo et al.*, 2013). Therefore, a better understanging of wave dynamics may assist in the ability to predict the occurrence and intensity of ensuing turbulence.

REFERENCES

REFERENCES

Beer, T. (1974), *Atmospheric waves*, John Wiley and Sons, New York, NY.

Bergström, H., and U. Högström (1989), Turbulent exchange above a pine forest. 2. organized structures, *Bound. Layer Meteor.*, *49*, 231–263.

Blackadar, A. K. (1957), Boundary layer wind maxima and their significance for the growth of nocturnal inversions, *Bull. Amer. Meteor. Soc.*, *38*, 283–290.

Blaes, O. (2011), University lecture, University of California, Santa Barbara, California Physics, Santa Barbara, CA.

Boyce, W. E., and R. C. DiPrima (2004), *Elementary Differential Equations and Boundary Value Problems*, John Wiley and Sons, Hoboken, NJ.

Cava, D., U. Giostra, M. Siqueira, and G. Katul (2004), Organised motion and radiative perturbations in the nocturnal canopy sublayer above an even-aged pine forest, *Bound. Layer Meteor.*, *112*, 129–157.

Dewan, E. M., R. H. Picard, R. R. O'Neil, H. A. Gardiner, J. Gibson, J. D. Mill, E. Richards, M. Kendra, and W. O. Gallery (1998), MSX satellite observations of thunderstorm-generated gravity waves in mid-wave infrared images of the upper stratosphere, *Geophysical Research Letters*, *25*(7), 939–942.

Durran, D. (1999), *Numerical methods for wave equations in geophysical fluid dynamics*, Springer, New York, NY.

Durran, D. R. (2015), Lee waves and mountain waves, in *Encyclopedia of Atmospheric Sciences*, vol. 3, edited by G. North, J. Pyle, and F. Zhang, second ed., Elsevier Science, Waltham, MA.

Einaudi, F., and J. J. Finnigan (1981), The interaction between an internal gravity wave and the planetary boundary layer. part i: The linear analysis, *Quart. J. R. Met. Soc.*, *107*(454), 793–806, doi:10.1002/qj.49710745404.

Ferrare, R. A., E. W. Eloranta, and R. Coulter (1991), Lidar observations of banded convection during blx83, *J. Appl. Meteor.*, *30*, 312–326.

Fitzjarrald, D. R., and K. E. Moore (1990), Mechanisms of nocturnal exchange between the rain forest and the atmosphere, *J. Geophys. Res*, *95(D10)*, 16,839–16,850.

Gossard, E., and W. Munk (1954), On gravity waves in the atmosphere, *J. Meteor.*, *11*(4), 259–269.

Hamada, M. (2014), Evaluations of the performance of a cross-correlation algorithm for wind velocity estimation using synthetic backscatter lidar images and velocity fields, Master's thesis, California State University, Chico.

Held, A., T. Seith, I. M. Brooks, S. J. Norris, and S. D. Mayor (2012), Intercomparison of lidar aerosol backscatter and in-situ size distribution measurements, in *European Aerosol Conference*.

Holton, J. R. (2004), *An introduction to dynamic meteorology*, International geophysics series, Elsevier Academic Press, Amsterdam, Boston, Heidelberg.

Hooke, W., J. Hall, F. F., and E. Gossard (1973), Observed generation of an atmospheric gravity wave by shear instability in the mean flow of the planetary boundary layer, *Bound. Layer Meteor.*, *5*(1-2), 29–41.

Hooke, W. H. (1986), Gravity waves, in *Mesoscale Meteorology and Forecasting*, edited by P. Ray, American Meteorological Society, Boston, MA.

Hu, X. (2001), Nocturnal wave-like air motion in forests, Ph.D. thesis, Yale University.

Jachens, E. R., T. N. Randall, and S. D. Mayor (2012), Lidar observations of fine-scale atmospheric gravity waves in the nocturnal boundary layer above an orchard canopy, in *26th International Laser Radar Conference*, Porto Heli, Greece.

Kaimal, J. C., and J. J. Finnigan (1994), *Atmospheric Boundary Layer Flows*, 289 pp., Oxford University Press, New York, NY.

Kolmogorov, A. (1941), Interpolation und extrapolation von stationären zufälligen folgen, *Bulletin de l'Acadmie des Sciences de l'URSS*, *5*, 3–14.

Kundu, P. K., I. M. Cohen, and D. R. D. Ph.D. (2011), *Fluid Mechanics, Fifth Edition*, Academic Press.

Lane, T. (2015), Convectively generated gravity waves, in *Encyclopedia of Atmospheric Sciences*, vol. 3, edited by G. North, J. Pyle, and F. Zhang, second ed., Elsevier Science, Waltham, MA.

Lee, X. (1997), Gravity waves in a forest: A linear analysis, *J. Atmos. Sci.*, *54*, 2574–2585.

Lee, X., and A. G. Barr (1998), Climatology of gravity waves in a forest, *Quart. J. R. Met. Soc.*, *124*, 1403–1419.

Lee, X., T. Black, G. den Hartog, H. H. Neumann, Z. Nesic, and J. Olejnik (1996), Carbon dioxide exchange and nocturnal processes over a mixed deciduous forest, *Ag. and Forest Met.*, *81*(12), 13–29.

Lee, X., H. H. Neumann, G. D. Hartog, J. D. Fuentes, T. A. Black, R. E. Mickle, P. C. Yang, and P. D. Blanken (1997), Observation of gravity waves in a boreal forest, *Bound. Layer Meteor.*, *84*, 383–398.

Lilly, D. K. (1986), Instabilities, in *Mesoscale Meteorology and Forecasting*, edited by P. Ray, American Meteorological Society, Boston, MA.

Mahrt, L. (2014), Stably stratified atmospheric boundary layers, *Annual Review of Fluid Mechanics*, *46*(1), 23–45, doi:10.1146/annurev-fluid-010313-141354.

Martin, J. E. (2006), *Mid-Latitude Atmospheric Dynamics*, John Wiley and Sons, Ltd, West Sussex, England.

Mayor, S. D. (2008), Raman-shifted Eye-safe Aerosol Lidar (REAL) observations at the Canopy Horizontal Array Turbulence Study (CHATS), in *18th Symposium on Boundary Layers and Turbulence*, AMS.

Mayor, S. D., G. J. Tripoli, and E. W. Eloranta (2003), Evaluating large-eddy simulations using volume imaging lidar, *Mon. Wea. Rev.*, *131*, 1428–1452.

Mayor, S. D., S. M. Spuler, B. M. Morley, and E. Loew (2007), Polarization lidar at 1.54-microns and observations of plumes from aerosol generators, *Opt. Eng.*, *46*, DOI: 10.1117/12.781,902.

Nappo, C., J. Sun, L. Mahrt, and D. Belušić (2013), Determining Wave-Turbulence Interactions in the Stable Boundary Layer, *Bull. Amer. Meteor. Soc.*, *95*(1), 11–13, doi:10.1175/BAMS-D-12-00235.1.

Nappo, C. J. (2012), *An Introduction to Atmospheric Gravity Waves*, 400 pp., Academic Press, Oxford, UK.

Newsom, R. K., and R. M. Banta (2003), Shear-flow instability in the stable nocturnal boundary layer as observed by doppler lidar during CASES-99, *J. Atmos. Sci.*, *60*, 16–33.

Nieuwstadt, F. T. M. (1984), The Turbulent Structure of the Stable, Nocturnal Boundary Layer, *Journal of the Atmospheric Sciences*, *41*(14), 2202–2216, doi:10.1175/1520-0469(1984)041⟨2202:TTSOTS⟩2.0.CO;2.

Patton, E. G., et al. (2011), The Canopy Horizontal Array Turbulence Study (CHATS), *Bull. Amer. Meteor. Soc.*, *92*, 593–611.

Paw U, K. T., Y. Brunet, S. Collineau, R. H. Shaw, T. Maitani, J. Qiu, and L. Hipps (1992), On coherent structures in turbulence above and within agricultural plant canopies, *Ag. and Forest Met.*, *61*(12), 55–68, doi:http://dx.doi.org/10.1016/0168-1923(92)90025-Y.

Petty, G. W. (2008), *A First Course in Atmospheric Thermodynamics*, Sundog Publishing, Madison, WI.

Poulos, G., et al. (2002), Cases -99: A comprehensive investigation of the stable nocturnal bondary layer, *Bull. Amer. Meteor. Soc.*, *83*, 555–581.

Randall, T. N., E. R. Jachens, and S. D. Mayor (2012), Lidar observations of fine-scale atmospheric gravity waves in the nocturnal boundary layer above an orchard canopy, in *20th Symp. on Boundary Layers and Turbulence*, AMS.

Stensrud, D. (2007), *Parameterization schemes: keys to understanding numerical weather prediction models*, Cambridge University Press, Cambridge, UK.

Stull, R. B. (1988), *An Introduction to Boundary Layer Meteorology*, Kluwer, Boston, MA.

Sun, J., et al. (2015), Review of wave-turbulence interactions in the stable atmospheric boundary layer, Submitted to: *Rev. Geophys.*

Sutherland, B. (2010), *Internal Gravity Waves*, New York, NY.

Taylor, J. R. (2005), *Classical Mechanics*, University Science Books, Herndon, VA.

Time and Date AS (1995), timeanddate.com.

Valkonen, T., T. Vihma, S. Kirkwood, and M. M. Johansson (2010), Fine-scale model simulation of gravity waves generated by basen nunatak in Antarctica, *Tellus A*, *62*(3), 319–332, doi:10.1111/j.1600-0870.2010.00443.x.

Van Gorsel, E., I. N. Harman, J. J. Finnigan, and R. Leuning (2011), Decoupling of air flow above and in plant canopies and gravity waves affect micrometeorological estimates of net scalar exchange, *Agr. Forest Meteorol.*, *151*, 927–933.

Wilczak, J., E. Gossard, W. Neff, and W. Eberhard (1996), Ground-based remote sensing of the atmospheric boundary layer: 25 years of progress, in *Boundary-Layer Meteorology 25th Anniversary Volume, 1970-1995*, edited by J. Garratt and P. Taylor, pp. 321–349, Springer Netherlands, doi:10.1007/978-94-017-0944-6_14.